THE EFFECT OF SUBMERGED ARC WELDING PARAMETERS ON THE PROPERTIES OF PRESSURE VESSEL AND WIND TURBINE TOWER STEELS

A Thesis Submitted to the College of
Graduate Studies and Research
in Partial Fulfillment of the Requirements
for the Degree of Master of Science
in the Department of Mechanical Engineering
University of Saskatchewan
Saskatoon

By

Yongxu Yang

PERMISSION TO USE

In presenting this thesis in partial fulfilment of the requirements for a Postgraduate degree from the University of Saskatchewan, I agree that the Libraries of this University may make it freely available for inspection. I further agree that permission for copying of this thesis in any manner, in whole or in part, for scholarly purposes may be granted by the professors who supervised my thesis work or, in their absence, by the Head of the Department or the Dean of the College in which my thesis work was done. It is understood that any copying or publication or use of this thesis or parts thereof for financial gain shall not be allowed without my written permission. It is also understood that due recognition shall be given to me and to the University of Saskatchewan in any scholarly use which may be made of any material in my thesis.

Requests for permission to copy or to make other use of material in this thesis in whole or part should be addressed to:

Head of the Department of Mechanical Engineering
57 Campus Drive
University of Saskatchewan
Saskatoon, Canada S7N 5A9

ABSTRACT

Submerged arc welding (SAW) is commonly used for fabricating large diameter linepipes, pressure vessels and wind turbine towers due to its high deposition rate, high quality welds, ease of automation and low operator skill requirement. In order to achieve high melting efficiency required for high productivity, best weld quality and good mechanical properties in manufacturing industries, the welding process parameters need to be optimized.

In this study, the effect of SAW current and speed on the physical and mechanical properties of ASME SA516 Gr. 70 (pressure vessel steel) and ASTM A709 Gr. 50 (wind turbine tower steel) were investigated. Three welding currents (700 A, 800 A and 850 A) and four travel speeds (5.9, 9.3, 12.3 and 15.3 mm/s) were used to weld sample plates measuring 915 mm x 122 mm x 17 mm. The weld quality and properties were evaluated using weld geometry measurements, visual inspection, ultrasonic inspection, hardness measurements, optical microscopy, tensile testing, Charpy impact testing and scanning electron microscopy.

It was found that the physical and mechanical properties of the weldments were affected by SAW parameters. Severe undercuts were found at high travel speed and welding current. Low heat input caused lack of penetration defects to form in the weldments. The welding process melting efficiency (WPME) achieved was up to 80%. The hardness of the coarse grain heat affected zone (CGHAZ) and the weld metal increased with travel speed. The toughness of both materials increased with increasing travel speed and welding current. The yield and tensile strengths of the weldments of SA516 Gr.70 and A709 Gr.50 steels were within the same range as those of their respective parent metals because all test specimens broke in the parent metals. Also, the parent metals of both steels had the highest fracture strain and percent elongation. The percentage elongation increased with travel speed but decreased with welding current.

ACKNOWLEDGMENTS

I would like to express my earnest gratitude to my supervisors, Drs. S. Yannacopoulos and I. N. A. Oguocha, for their invaluable guidance and support throughout the duration of this research project. I wish to extend my appreciation to my supervisory committee members, Drs. Qiaoqin Yang and Reza Fotouhi, for their criticisms, suggestions and useful feedback.

I would like to thank the Hitachi Canadian Industries (HCI) Ltd., Saskatoon, for the supply of the test materials, funding, and scientific input. My thanks go to Mr. Augustin Marisca and Dr. Huawei Guo for their support and feedback throughout this study.

I wish to express my appreciation to Mr. Robert Peace and Mr. Hans Steinmetz for their valuable technical assistance. My thanks go to Mr. Fathi Hamad and Mr. J. C. Jackson of the Research Department of IPSCO Inc. Regina, for assistance with their Charpy impact tester.

Finally, I am very grateful for this financial supports from the Natural Sciences and Engineering Research Council (NSERC), HCI and the University of Saskatchewan.

May God bless you all.

DEDICATION

My Parents

My wife Ying Zhu

And

My twin girls

Lillian Bingxuan Yang

Vivian Xueqi Yang

.

TABLE OF CONTENTS

LIST OF TABLES

LIST OF FIGURES

NOMENCLATURE

Abbreviations

A	Welding current
A_d	Deposition area
A_f	Total fusion area
AF	Acicular ferrite
A_{HAZ}	Area of the heat affected zone
ANOVA	Analysis of variance
A_p	Area of penetration
A_r	Reinforcement area
ASME	American Society of Mechanical Engineers
ASTM	American Society for Testing and Materials
ASPF	Aligned side plate ferrite
AWS	American Welding Society
b	Weld bead width
B	Basicity index
BF	Block ferrite
CCT	Continuous cooling transformation
CGHAZ	Coarse grain heat affected zone
CVN	Charpy V-notch
d	Grain size
DAC	Distance amplitude correction
DBTT	Ductile-to-brittle transition temperature
EDS	Energy dispersive X-ray spectroscopy
EME	Electrode melting efficiency
FGHAZ	Fine grain heat affected zone
FZ	Fusion zone
GMAW	Gas metal arc welding
GTAW	Gas tungsten arc welding
H	Welding heat input

HAZ	Heat affected zone
HSLA	High-strength low-alloy
I	Welding current
ITT	Impact transition temperature
K	Coefficient of welding efficiency
k_y	Strengthening coefficient
NDT	Non-destructive test
P	Penetration depth
PF	Polygonal ferrite
PGBF	Proeutectoid grain boundary ferrite
PME	Plate melting efficiency
PM	Parent metal
PV	Pressure vessel
PWHT	Post weld heat treatment
R	Reinforcemen
R_d	Deposition rate
S	Travel speed
SAW	Submerged arc welding
SEM	Scanning electron microscopy
SMAW	Shield metal arc welding
TS	Tensile strength
V	Welding voltage
V_α	Volume fraction of α phase
V_β	Volume fraction of β phase
w	HAZ size
WFS	Wire feed speed
WI	Weld interface
WM	Weld metal
WPME	Welding process melting efficiency
WSPF	Widmanstatten side plate ferrite

WT	Wind turbine tower
YS	Yield strength

Greek Symbols

ρ	Density of the welding metal
θ	Contact angle
σ	Strength of a multiphase alloy
σ_{α}	Strength of α phase
σ_{β}	Strength of β phase
σ_{i}	Friction stress
σ_{y}	Yield strength
σ_{ts}	Tensile strength

1 INTRODUCTION

1.1 Overview

High-strength low-alloy (HSLA) steels are a class of alloy steels with low carbon content and small additions of alloying elements such as niobium, aluminum, vanadium, titanium, molybdenum, copper, and zirconium [1]. They have a good combination of strength, toughness, and good formability and weldability. The good strength is produced by the addition of small quantities of alloying elements at concentration of less than 0.1 wt.%. Their yield strength is about 2 to 3 times greater than that of plain carbon steels. Therefore, they can provide better mechanical properties and/or greater atmospheric corrosion resistance than plain carbon steels or conventional low-alloy steels. Their good formability and weldability come from the low carbon content (0.05 to ~ 0.25 wt.% C) and low quantity of alloying elements [2]. HSLA steels are widely used in many applications such as high pressure vessels, wind turbine towers, ships, submarines, long distance oil and gas transportation systems, bridge beams and other offshore structures. In most of these applications, welding is the primary fabrication method in industries.

The most widely used welding methods in industries and research organizations are shield metal arc welding (SMAW), gas metal arc welding (GMAW), gas tungsten arc welding (GTAW) and submerged arc welding (SAW). The SAW process is often preferred because it offers high production rate, high melting efficiency, ease of automation and low operator skill requirement. It was first used in industries in the mid 1930's as a single-wire welding system. It was further developed into two-wire or three-wire system because of high productivity requirements after the Second World War. Recently, five-wire SAW system has also been developed to get high welding speed and high productivity [3].

Figure 1.1 shows three main zones of a typical weldment, namely: (i) the parent metal (PM), (ii) the heat affected zone (HAZ) and (iii) the weld metal (WM) or fusion zone (FZ). The high welding current used in the SAW process results in high heat input in the weldment. The consequence of this is the deterioration of the mechanical properties of the parent metal. Two main factors are responsible for this deterioration. The first comes from the welding thermal cycles which result in large HAZ within which the microstructure of the parent metal is altered by the high temperature of the molten weld pool. The toughness of HAZ is impaired because of the formation of martensite or other low-emperature transformation products such as lower bainite [4]. The other is the fast solidification structure in the WM which is a mixture of the parent metal, filler rod, and the flux. Thus, the compositions of the parent metal and the filler rod, heat input, cooling rate, solidification characteristics, and the welding thermal cycles contribute to the final properties of the weld joint. The high cooling rate and heat input obtained in the SAW process result in the WM developing a heterogeneous and columnar morphology with a high fraction of grain boundary ferrite [5-7]. Therefore, the properties of the parent metal cannot adequately match those of the weldments to ensure good performance in service, especially in low temperature services.

1.2 Motivation

The physical and mechanical properties of the weld metal vary with different welding parameters such as heat input, filler material type and size, flux chemistry, and preheat and inter-pass temperatures. The unavoidable welding discontinuities that exist in weld metals can also significantly affect the properties of weld joints. Engineers in the manufacturing industries and researchers often face the problem of selecting appropriate or optimum combinations of input welding parameters for achieving the required weld quality. Optimal control of the welding parameters will give the best properties of the weld and reduce weld defects.

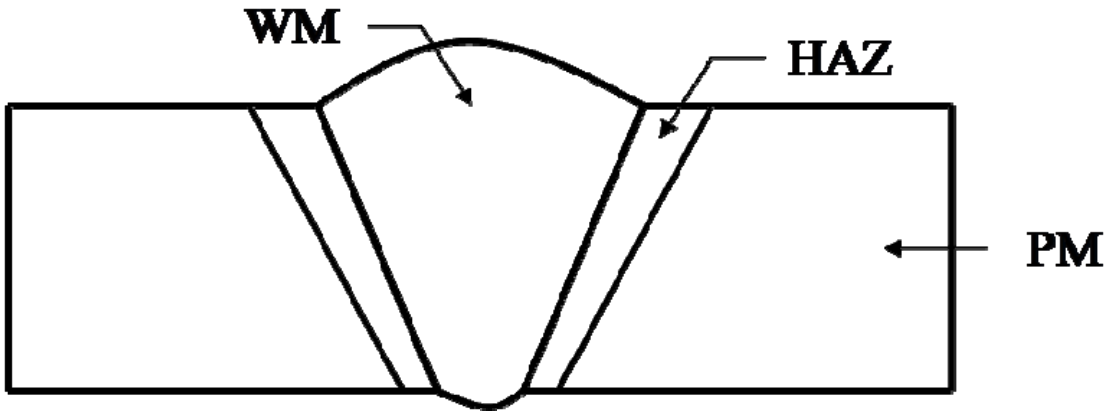

Figure 1.1. A sketch of a typical welding joint.

Many researchers [4, 8-12] have conducted experiments to determine how to select suitable welding parameters to optimize the weld metal strength and toughness when joining HSLA steels. McGrath *et al*. [8] reported that increasing the volume fraction of acicular ferrite (AF) benefits the toughness of the weld metal because of its peculiar structure. The random orientation of AF in the weld metal differs from the ordered orientation of classical bainite [11]. Hence, AF has superior resistance to cleavage crack propagation. The toughness of the weld metal is roughly proportional to the amount of acicular ferrite present [8].

Although many authors [4, 8-12] have reported on the optimization of the welding of various HSLA steels, to the best of the author's knowledge, there is no open literature source that has studied the effect of SAW process parameters on the properties of pressure vessel and wind turbine tower steels, ASME SA516 Grade 70 and ASTM A709 Grade 50 steel, respectively. Since these steels are heavily used in the fabrication industry, it is important to have adequate knowledge of how their physical and mechanical properties change with SAW parameters.

1.3 Objectives

The main objectives of this study were:

1. To investigate the effect of SAW process parameters on the physical and mechanical properties of SA516 Gr.70 and A709 Gr.50 steels.
2. To study the relationship between SAW process parameters and welding performance.
3. To select proper SAW process parameters in order to increase productivity and melting efficiency while maintaining acceptable weld quality for SA516 Gr.70 and A709 Gr.50 weldments.

1.4 Methods of Evaluation

In order to understand the effect of SAW parameters such as welding current and travel speed on the physical and mechanical properties of SA516 and A709 steels, the as-welded test specimens were evaluated by weld geometry measurements to find the relationship between the welding parameters and weld geometry parameters. The external and internal defects were evaluated by visual examination and ultrasonic examination. The traverse hardness of the weld was obtained using Vickers hardness measurements. The microstructure of the weld metal, HAZ, and parent metal was studied by metallography and optical microscopy. The yield strength, tensile strength and percent elongation of the weldment were determined using tensile testing. Impact toughness and lateral expansion were determined using Charpy impact testing.

1.5 Thesis Outline

This thesis is divided into five chapters. Chapter 1 presents an overview of the research project, its motivation and main objectives. A comprehensive literature review pertinent

to this project is presented in Chapter 2. Chapter 3 discusses materials and experimental methods used in this study. Chapter 4 presents and discusses the experimental results, while Chapter 5 summarizes the conclusions deduced from the results and suggests recommendations for future work.

2 LITERATURE REVIEW

In this chapter, the properties and applications of HSLA steels will be discussed. Fundamental information about the SAW process, weld discontinuities and detection methods, weld microstructures, SAW parameters, and the effect of these parameters on the properties of HSLA steels, weld performance, and weld melting efficiencies will also be introduced.

2.1 High Strength Low Alloy (HSLA) Steels

HSLA steels were developed in the 1960s, originally for large diameter oil and gas pipelines. They have high strength combined with improved toughness and good weldability. Typically, they contain 0.05 wt.% to 0.25 wt.% carbon, up to 2 wt.% manganese and small additions of niobium, vanadium and titanium (less than 0.1 wt.%) in various combinations. The standard carbon manganese steel is strengthened by small amount of niobium and vanadium without interfering in subsequent processes such as machine and welding processes [1, 13, 14]. The hardness and the weldability of steels are evaluated using the carbon equivalent (CE). The CE can be calculated according to equation (2.1) using wt. % of elements [15]:

$$CE = C\% + \frac{Mn\%}{6} + \frac{Ni\% + Cu\%}{15} + \frac{Mo\% + Cr\% + V\%}{5} \qquad 2.1$$

Low CE is desirable because it helps to prevent hard phases such as matensite forming when the weldment cools to room temperature. Generally, matensite causes high

hardness, high residual stress and easy cracking of the weldment. Therefore, reducing carbon content can significantly change the carbon equivalent. Both weldability and toughness can be improved when carbon content decreases in the steel. The strengthening effect of small quantities of alloying elements in HSLA steels, such as niobium and vanadium, can compensate for the reduction in strength due to the reduction in carbon content.

Although the microalloying elements in HSLA steels can improve their mechanical properties, the rolling technique is a very important method to improve the strength of hot-rolled HSLA steels through grain refinement. The use of controlled rolling method in the austenite condition can improve toughness and result in high yield strength in the range of 345 MPa to 620 MPa in typical HSLA steels [13]. The development of controlled rolling processes allows for a reduction in the carbon content of steel without adversely affecting its mechanical properties. The yield strength of many microalloyed steels can reach up to 485 MPa even when the carbon content is as low as 0.06 wt.% [13]. Thus, high yield strength of HSLA steels is achieved by the combination of fine grain size forming during controlled hot rolling and precipitation strengthening due to the presence of small quantity alloy elements. Typically, ferrite and pealite form the main microstructures of HSLA steels with manganese providing solid solution strengthening of the ferrite.

The effects of the addition of alloying elements on the properties of HSLA steels differ according to the application. The addition of molybdenum played an important role in the initial development of HSLA steels [1]. The addition of 0.1-0.2 wt.% molybdenum produces a fine grain structure of acicular ferrite and substantially enhances the precipitation hardening effect achieved with the other alloying elements. Niobium, titanium, and vanadium can enhance the yield strength of HSLA steels by forming interphase precipitates and controlling grain size during hot rolling. The strengthening due to vanadium addition is between 5 and 15 MPa per 0.01 wt.%, depending on the carbon content and the rate of cooling from hot rolling. Strengthening by niobium addition contributes 35 to 40 MPa per 0.01 wt.% addition [13]. Titanium forms several

compounds that provide grain refinement, precipitation strengthening, and sulfide control in low carbon steels. Copper is another element that improves strength through solid solution strengthening of ferrite and contributes greatly to the corrosion resistance of carbon steels by retarding the rate of rusting at room temperature through a formation of the protective oxide (CuO) film [13]. Zirconium and rare earth elements are used to control the shape of iron sulfide (FeS_2) and oxide inclusions such as γ-Al_2O_3, titanium oxide (Ti_xO_y), $MnOSiO_2$, and galaxite (MnO-Al_2O_3) [16].

2.2 Submerged Arc Welding (SAW)

Figure 2.1 shows a typical equipment set-up for single wire SAW process. The controlled welding current provides the heat to fuse the filler rod, parent metal and flux which is supplied from flux hopper. The flux forms a glasslike slag that is lighter in weight than the deposited weld metal and floats on the surface as a protective cover against oxidization of the steel. The wire speed is controlled by a wire feeder to adjust the deposition rate according to different heat input. The infused flux is collected by vacuum for recycling and thus keeping the shop air clean.

The SAW process is quite different from other arc welding processes such as shield metal arc welding (SMAW), gas tungsten arc welding (GTAW) and gas metal arc welding (GMAW). SMAW is a manual arc welding process that uses a consumable electrode with coated flux. GTAW is also a manual arc welding that uses a nonconsumable tugsten electrode with filler wire. GMAW is a semi-automatic or automatic arc welding process that uses a continuous consumable welding wire with a shielding gas such as argon or carbon dioxide. The greatest advantage of SAW is its high welding productivity due to its high deposition rate, ease of automation and low operator skill requirements. Its productivity level is about 4 to 10 times that of the SMAW process. Since the electric arc is covered by the granular flux or molten slag, minimal welding fume or arc light is emitted. Therefore, the working environment is very comfortable to operators who may not need to wear goggles and thick clothes to protect themselves. At the same time, the

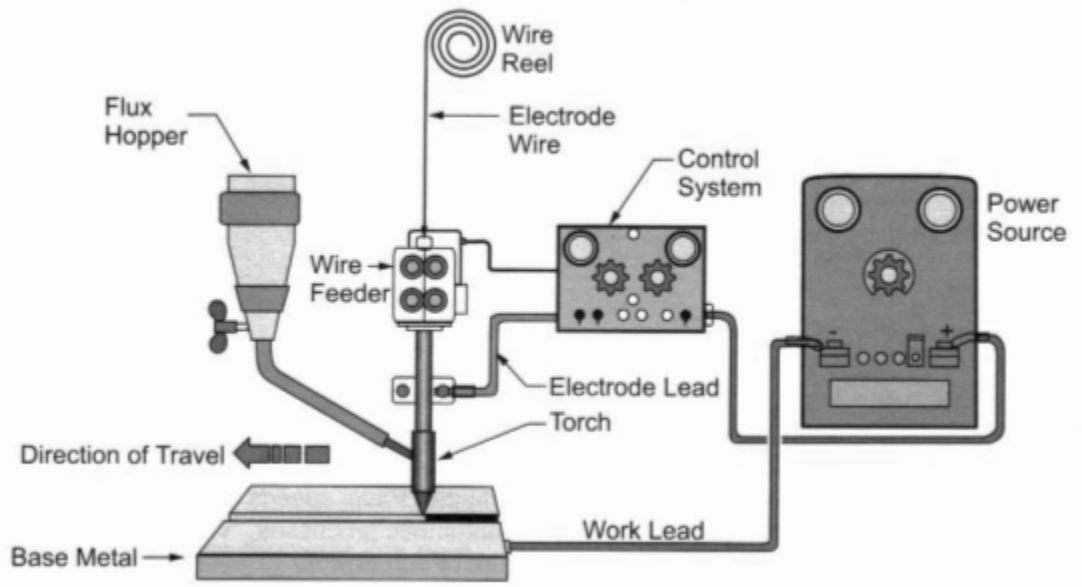

Figure 2.1. Equipment set-up for single wire submerged arc welding [17].

high welding current (300 A to 1600 A), combined with its fast travel speed, can be used to increase the heat input and deposition rate. The thermal efficiency (ratio of energy output to the energy input) of the SAW process is as high as 60% because of low heat loss to the environment [18]. It is ideally suited for longitudinal and circumferential butt and fillet welds. However, the SAW process is generally carried out on butt welded joints in the flat position, and in both flat and horizontal-vertical positions for fillet welded joints, due to high fluidity of the weld pool, molten slag and loose flux layer. For circumferential welded joints, the workpiece is rotated under a fixed welding head, with welding taking place in the flat position. Like the SMAW process, the interpass and post weld slag and flux of SAW process should be removed from the weldment. The welding materials are limited to carbon-manganese steels, HSLA steels, low alloy steels and stainless steels.

There is no restriction on the material thickness, provided suitable joint preparation and welding procedures are used. Either single-pass or multiple-pass welding procedures should be carried out depending on the thickness of the workpiece. With the development of SAW technologies, some setups allow two or more wires to be fed simultaneously into

the joint, further increasing the deposition rate and speed. The SAW process is able to produce larger products such as pressure vessel, wind turbine tower and bridge beams.

2.2.1 The Structure of a Weld Joint

A weld joint can be divided into four different microstructural zones. They are the weld metal (WM), weld interface (WI), HAZ, and the unaffected parent metal (PM) zone. Figure 2.2 shows the zones of a typical butt welded joint.

The weld metal, also called the fusion zone, is a mixture of the filler rod, flux, and parent metal that has completely melted during fusion process. Figure 2.3 shows that the central temperature of the weld metal is higher than 1700 ^{o}C [19].

The weld interface, also called fusion line, is a narrow boundary that separates the weld metal and the HAZ. This interface consists of a thin band of the parent metal that is melted or partially melted during the welding process, but immediately solidifies before any mixing can take place.

The HAZ is adjacent to the weld metal. The metal in this region experiences temperatures below its melting point, but high enough to change its microstructure so that its properties are altered. As shown in Figure 2.3, the temperature of HAZ during welding ranges from 700 ^{o}C to 1400 ^{o}C. In region 1, austenite grain can grow because of high temperatures in this region close to the weld interface. Therefore, the coarse grain HAZ (CGHAZ) is formed in this region. Region 2 is not significantly affected by grain growth. In region 3, the austenite grains are very fine since some grains transform to austenite and some do not. Thus this region is called the fine grain HAZ (FGHAZ). No austenite transformation takes place in region 4, but the ferrite grain may be tempered by the heat of welding.

The parent metal, near the HAZ, has no metallurgical change since the temperature is not high enough. However, the parent metal surrounding the HAZ is likely to be in a state of high residual stress due to shrinkage of the weld metal.

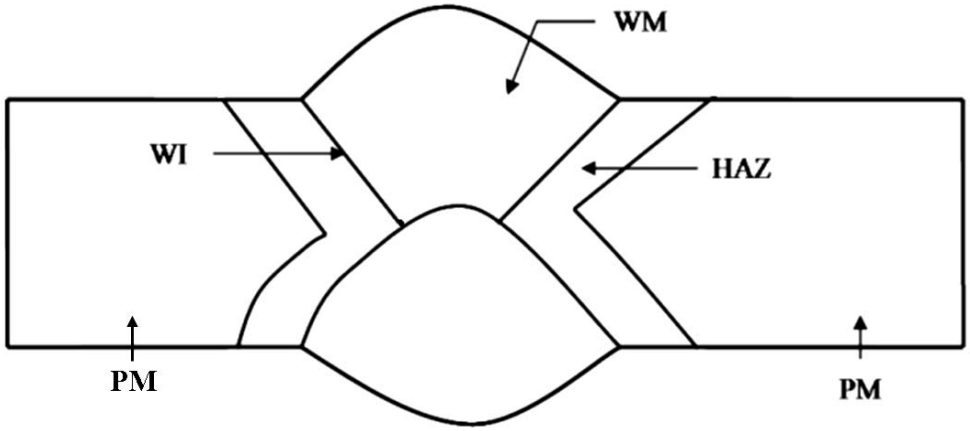

Figure 2.2. A sketch of two passes SAW joint zones.

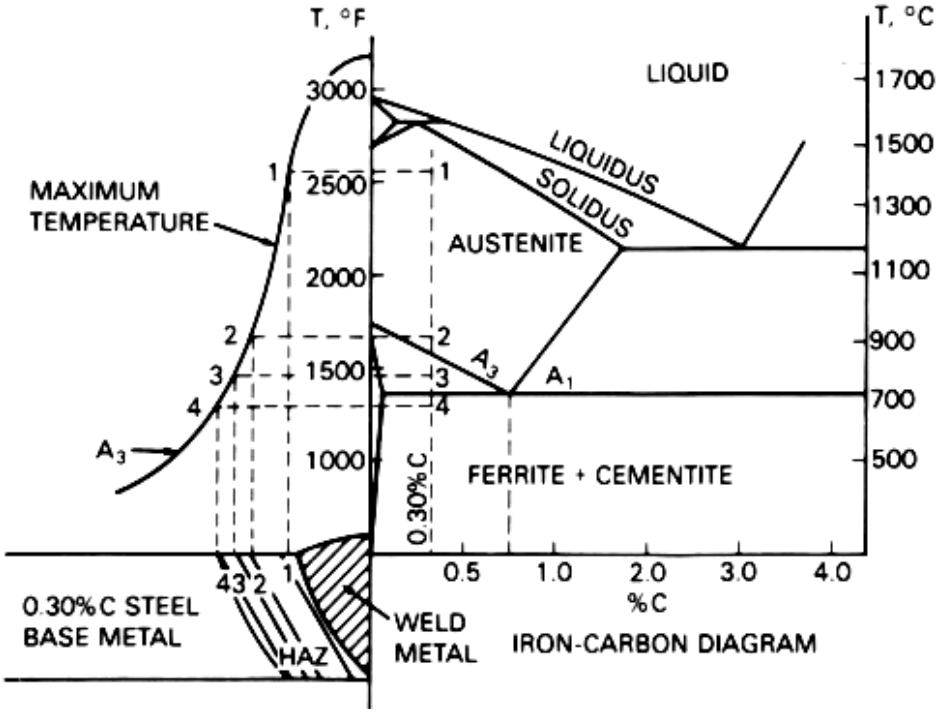

Figure 2.3. Approximate relationships among peak temperature, distance from weld interface, and the iron-carbon phase diagram [19].

2.2.2 SAW Microstructures and Properties

SAW involves many metallurgical phenomena, such as melting, freezing, solid state transformations, thermal strains and shrinkage stresses. The metallurgy of SAW is complex and depends on the compositions of the parent metal, the filler rod, and the flux, as well as on the welding parameters such as polarity, heat input, number of passes, etc. Although the composition of the filler rod is generally similar to that of the parent metal, the weld metallurgy is complicated because the weld metal composition comes from the filler rod, parent metal and microelements of the flux. At the same time, the different temperatures to which different weld zones are subjected result in a heterogeneous cooling rate in the weld joint. Thus, the microstructures of a weld joint are different from zone to zone, as shown in Figure 2.4. The microstructure of the weld metal is mainly coarse columnar gains, due to the relatively high heat input, large weld pool and fast solidification. Low toughness and hydrogen cracking of the weld metal results from the columnar microstructure in the weld metal [20]. The large grains in the CGHAZ near the weld interface result in high strength and low toughness in this region. Good mechanical properties are obtained from the FGHAZ due to its very small grain size. The microstructure of the parent metal remains unchanged.

The decomposition of austenite is generally shown in the form of a continuous cooling transformation (CCT) diagram such as that in Figure 2.5. The microstructural transformations that take place are largely dependent on the cooling rate and composition. The as-deposited or primary microstructure of the weld metal is the microstructure obtained as the weld cools from the liquid phase to room temperature. It consists of allotriomorphic ferrite (also called polygonal ferrite (PF) or proeutectoid grain boundary ferrite (PGBF)), aligned side plate ferrite (ASPF), block ferrite (BF), widmanstatten side plate ferrite (WSPF), acicular ferrite (AF), and microconstituents such as martensite, retained austenite, degenerate pearlite, and bainite [4, 22-26]. The morphologies of these microstructures are shown in Figures 2.6 and 2.7.

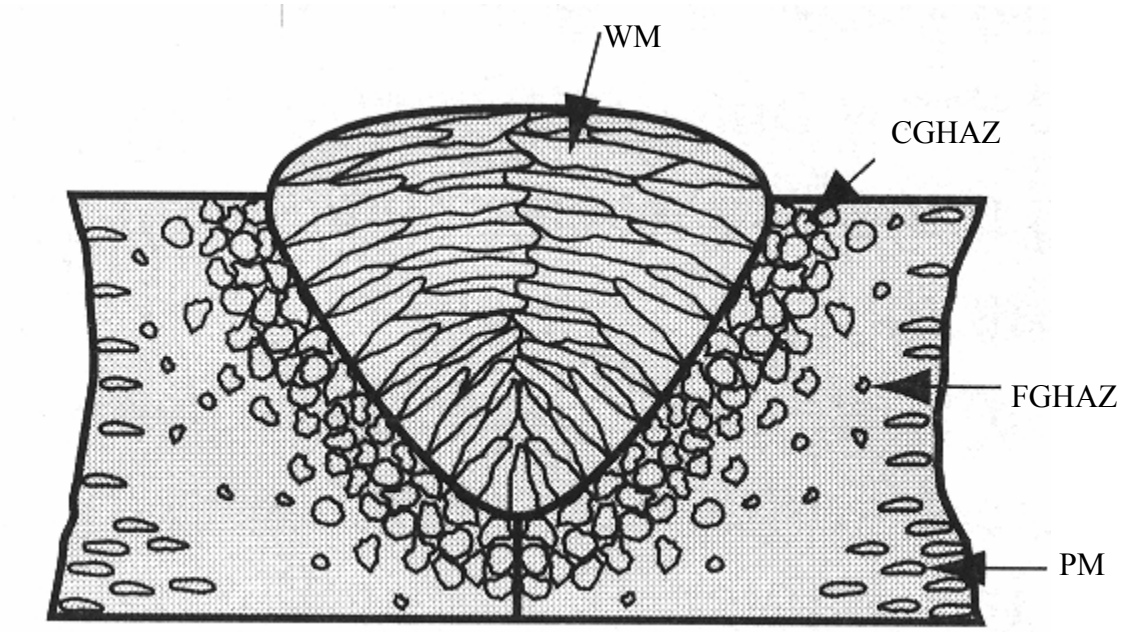

Figure 2.4. An illustration of the microstructure of a weld joint [21].

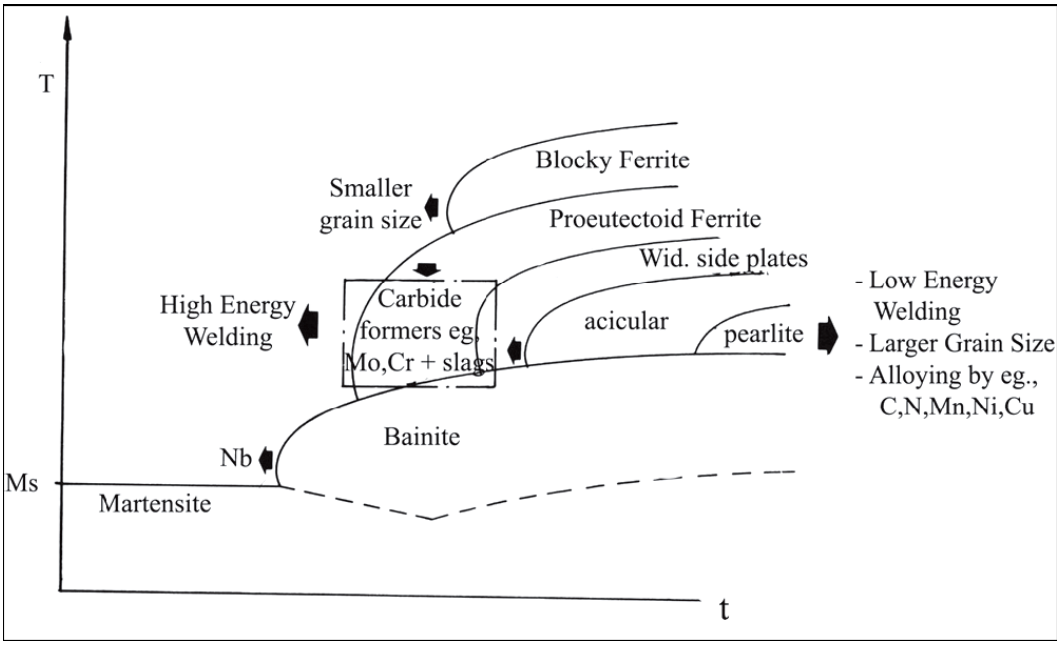

Figure 2.5. CCT diagram for steel WM summarizing the possible effects of microstructure and alloying on the transformation products for different weld cooling times [22].

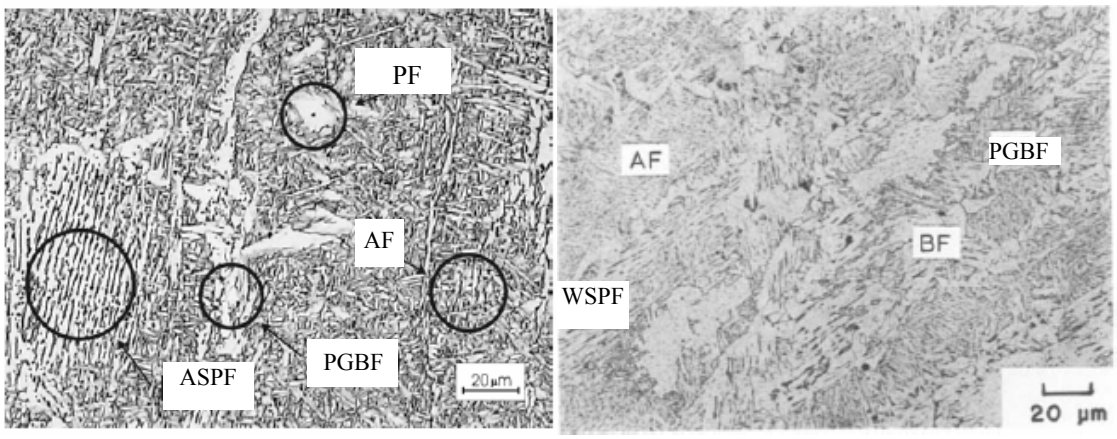

Figure 2.6. Optical micrographs of the weld metal in the as-weld condition showing AF, PGBF, PF, ASPF and WSPF [23, 24].

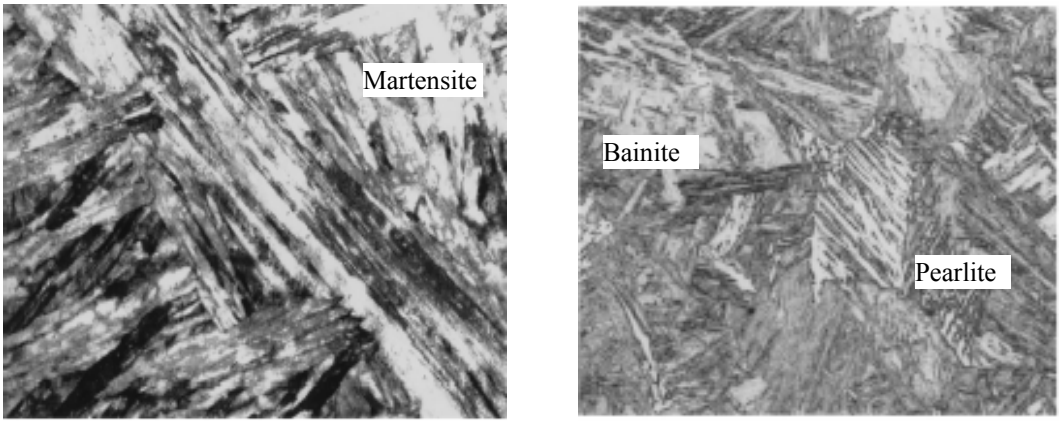

Figure 2.7. Microstructure of martensite, pearlite and bainite of a weldment [25].

The allotriomorphic ferrite is the first phase to form on cooling below the A_3 temperature shown in Figure 2.3, and nucleates heterogeneously at the boundaries of the columnar austenite grains. It is a relatively soft phase in the weld metal due to its low carbon content (0.02 wt. %) and has low toughness because it offers little resistance to cleavage crack propagation [26].

The acicular ferrite (AF) nucleates on small inclusions in the austenite grains in weld metal as temperature drops down [4, 26, 27]. The morphology of AF is called acicular due to its needle-like shape in two dimensional sections as shown in Figure 2.8. The shape of AF in three dimensions is plate or needle like-lath with typical dimensions of about 5 to 10 μm in length and around 1 μm in diameter [26, 28]. The AF microstructure provides the best combination of high strength and good toughness due to its superior resistance to cleavage crack propagation and its interlocked morphology to increase density of high-angle boundaries [26, 27]. The boundaries act as obstacles to cleavage and force cleavage cracks to change the planes of their growth in order to accommodate the changing local crystallography. Therefore, the ideal microstructure of the weld metal is the one that contains a large proportion of acicular ferrite. It is generally believed that the AF content of 80–90% in the as-deposited weld metal is necessary to obtain satisfactory toughness at low temperatures [27]. It is reported that acicular ferrite and bainite are formed by the same transformation mechanism [26, 28, 29]. Figure 2.9 illustrates the effect of austenite grain size in determining whether the microstructure is predominantly acicular ferrite or bainite. A small grain sized sample has a relatively large density of grain boundary nucleation sites and hence bainite dominates, whereas a relatively large number density of intragranular nucleation sites leads to a microstructure consisting mainly of acicular ferrite [26].

2.3 Weld Discontinuities and Weld Inspection

Weld discontinuities are produced in the weldments due to operators' carelessness or lack of skill, adverse working conditions, poor design, and lack of preparation for grooves during the welding process. It is inevitable that weld discontinuities will form in the weld joint because of the specific fast solidification. All weld discontinuities can significantly influence local stress field in the vicinity of welds when a welded component is subjected to loading. In general, the weld can endure the service conditions, even with the discontinuities, if they meet with the acceptable code or criteria which vary according to the application and the requirements. If the weld discontinuities cannot meet the

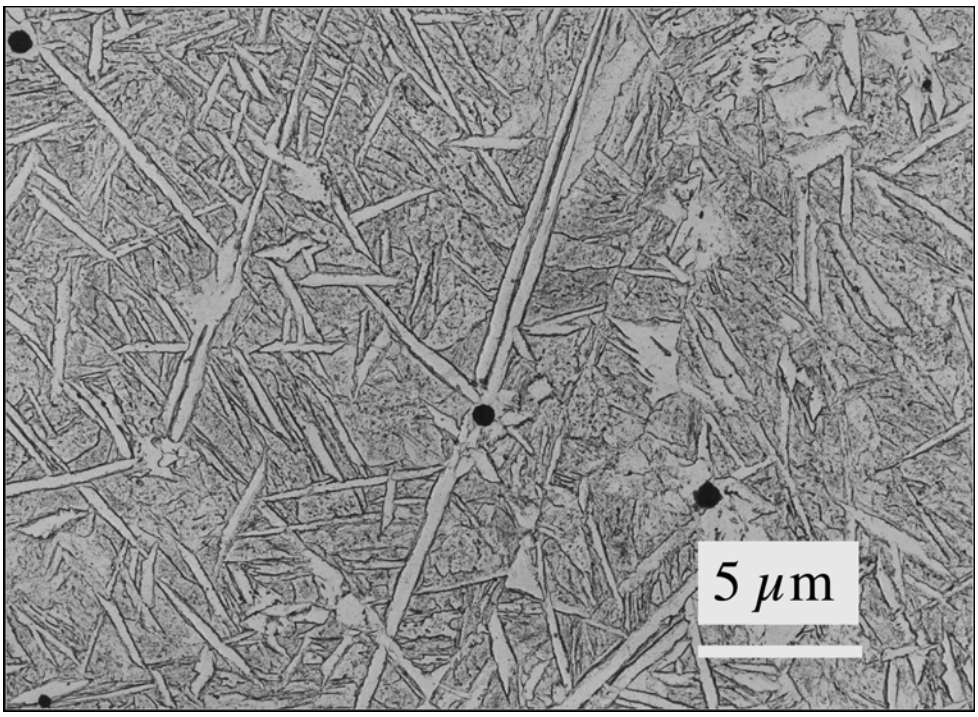

Figure 2.8. Replica transmission electron micrograph of acicular ferrite plates in a steel weld deposit [26].

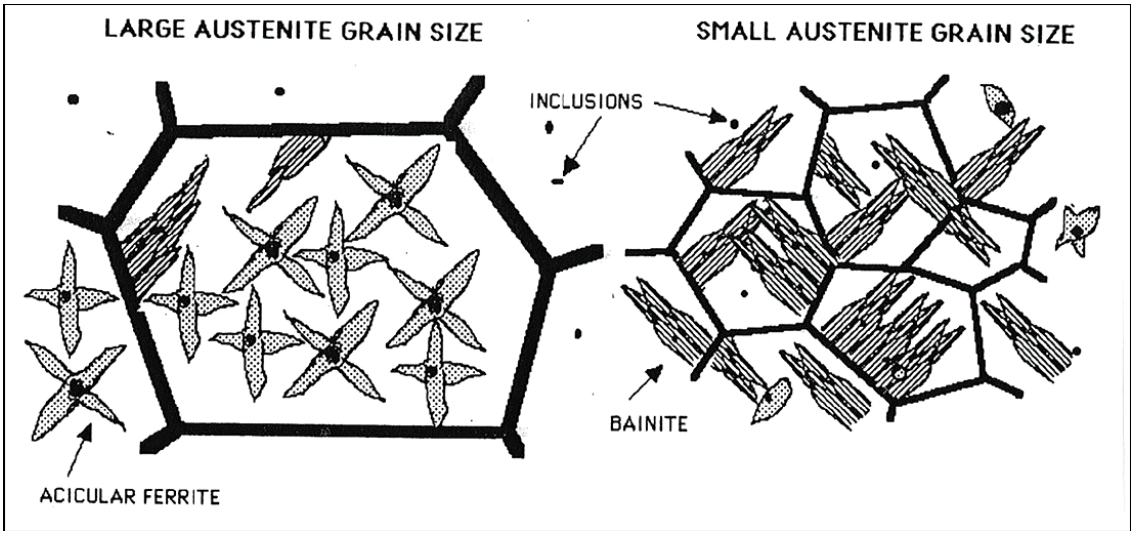

Figure 2.9. An illustration of nucleation and growth mechanisms for acicular ferrite and bainite [26].

acceptable criteria, they are called weld defects. The many types of weld defects that are found in weld metal can be divided by surface defects and internal defects. The characteristic features and principal causes of surface and internal defects are described in the remaining part of this section.

2.3.1 Surface Defects

Typical surface defects found in weld joints include surface porosity, misalignment, undercut, excessive reinforcement, crater hole, and solidification cracks. Figure 2.10 shows examples of surface defects. The surface conditions, welding variables, welding designs and weld preparation cause surface defects. When the surface of the weldment is contaminated by excessive grease, dampness or atmospheric entrainment, surface porosities (Figure 2.10(a)) may occur during the welding process. If the gap between two pieces of parent metal plates is too big for fit-up, misalignment (Figure 2.10(b)), distortion or deformation occurs due to excessive solidification force of the weld metal. The use of unsuitable welding parameters will also cause surface defects. An undercut (Figure 2.10(c)) is most commonly caused by improper welding parameters, particularly the travel speed and welding arc voltage. The forces of surface tension will draw the molten metal along the edges of the weld bead if it is very narrow because of fast travel speed [19]. Therefore, the metal is piled up along the center resulting in undercuts. If the heat input is excessive, it will cause excessive reinforcement (Figure 2.10d), which causes excessive stress concentration in the weldment. The crater hole (Figure 2.10e) results from shrinkage at the end crater of a weld run. The cause of solidification cracks (Figure 2.10f) is the large depth/width ratio of the weld bead that results in insufficient strength to endure the contraction stresses generated as the weld pool solidifies.

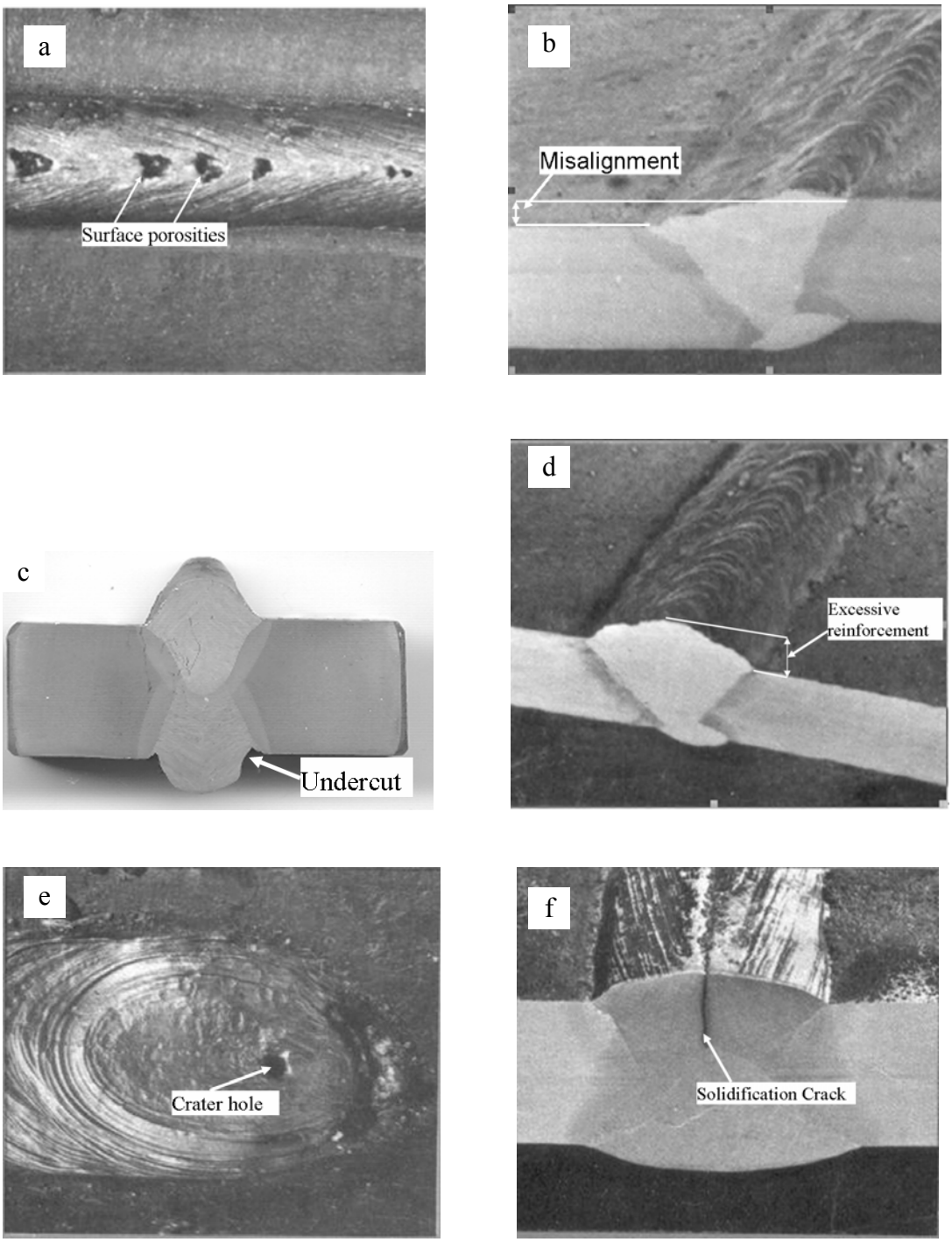

Figure 2.10. Typical examples of surface defects: (a) surface porosities, (b) misalignment, (c) undercut, (d) excessive reinforcement, (e) crater hole and (f) solidification crack [21].

2.3.2 Internal Defects

The internal defects that form in weld joints include lack of penetration, lack of side fusion, internal porosity, internal slag inclusion, hydrogen cracks, and reheat cracks. Compared to surface defects, internal defects bear more potential dangers and are more difficult to be inspected. Figure 2.11 shows the internal defects that can form in the weld joints. Lack of penetration (Figure 2.11(a), Figure 2.11(b)) occurs when a weld will not be adequately filled with weld metal. It maybe caused by too small root opening, too large electrode, insufficient weld current, and poor groove preparation. When gas pockets from moisture, surface impurities, or contaminations are trapped inside the weld metal, then internal porosity (Figure 2.11(c)) will form. An internal inclusion (Figure 2.11(d)) contains slag that has been trapped in the deposited metal during solidification. The hydrogen from electrodes or insufficient pre-weld and post-weld heat treatment will cause cold cracks, which may occur in the weld metal or in the HAZ as illustrated in Figure 2.11(e). Reheat cracking (Figure 2.11(f)) may occur in welds that are given a post heat treatment such as stress relief heat treatment, or has been subjected to high temperature service. The principal cause is that when heat treating susceptible steels, the grain interior becomes strengthened by carbide precipitation, forcing the relaxation of residual stresses by creep deformation at the grain boundaries [30].

2.3.3 Weld Inspection Methods

The two main categories of welding inspection methods widely used in industries are destructive testing (tensile testing, bending testing, Charpy impact testing and metallurgical examination) and non-destructive testing (NDT). The mechanical properties of weld metal and the microstructures of weld joints can be obtained through the destructive testing. This method is typically used in weld procedures specification qualification and failure analysis to find the root cause of failures. In the contrary, the

NDT methods are widely used in weld inspection after the welding process and in in-service weld inspection to test whether the weld quality meets the requirements of

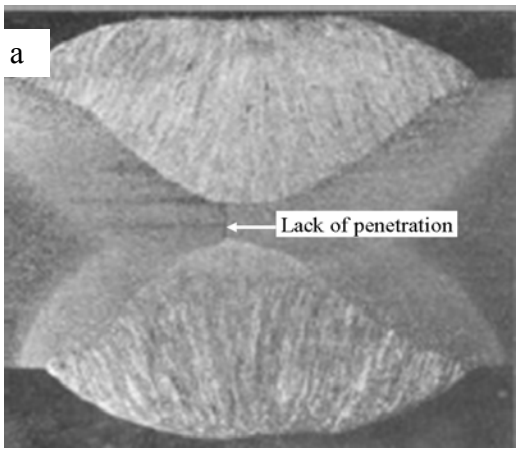

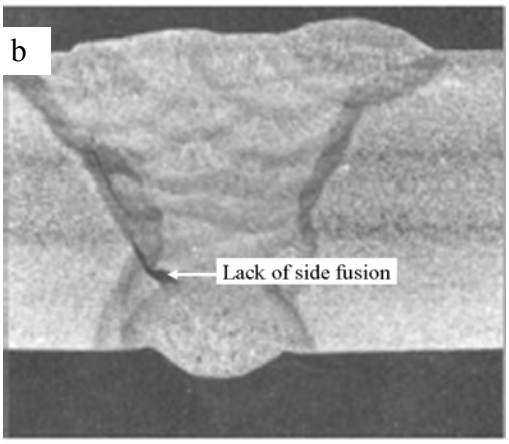

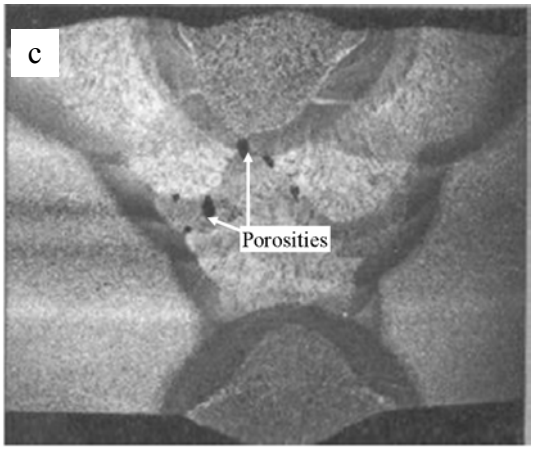

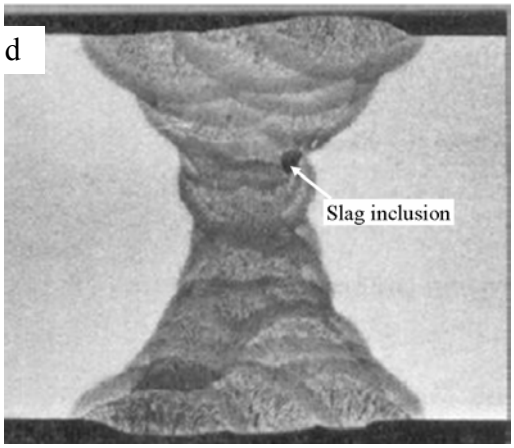

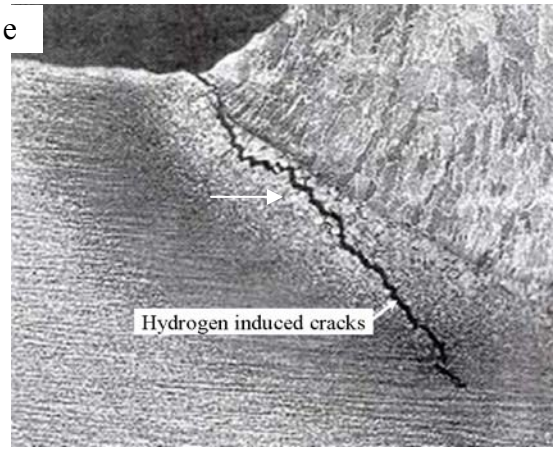

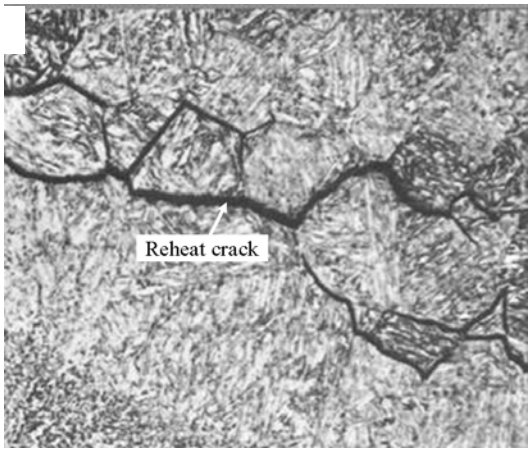

Figure 2.11. Typical examples of internal defects: (a) lack of penetration, (b) lack of side fusion, (c) internal porosities, (d) slag inclusion, (e) hydrogen-induced cold cracking and (f) reheat cracking [21, 30].

acceptance criteria according to its application.

Generally, six main NDT techniques are used in industries namely: visual inspection, liquid penetrant inspection, magnetic particle inspection, ultrasonic inspection, and radiographic inspection，eddy current inspection. Surface defects can be tested by visual inspection, liquid penetrant inspection, and magnetic particle inspection techniques while internal defects can be detected using ultrasonic inspection and radiographic inspection. Although eddy current inspection can also detect the internal or surface defects, it is typically used to detect the wall loss of small pipes such as heat exchangers in power plant or refinery companies. The following sections will briefly discuss each of these methods.

2.3.3.1 Visual Inspection

Visual inspection is the most extensively used NDT methods for weldments because it is easy to apply, simple, and relatively inexpensive. Visual inspection begins prior to the actual fabrication operations to ensure that the weld joint conforms to the specification requirements. After welding and heat treatment (where required) is completed, the finished weldment is inspected for weld bead width, bead appearance, or surface defects, such as surface cracks, porosity, undercut and other surface discontinuities. This method often proves to be a useful supplement to other NDT techniques.

2.3.3.2 Liquid Penetrant Inspection

Liquid penetrant inspection is a method capable of locating discontinuities such as cracks and porosities, shrinkage areas, laminations, and similar discontinuities which are open to the surfaces of nonporous materials. The method is based on the ability of the penetrating liquid to be drawn into a discontinuity using capillarity action. Then the white developer

bleeds out the penetrant from the discontinuties. In practice, it is relatively inexpensive and reliable method to utilize and control.

2.3.3.3 Magnetic Particle Inspection

Magnetic particle inspection is a method capable of locating the surface and subsurface discontinuities in ferromagnetic materials. The presence of a surface or near surface discontinuities in the material causes distortion in the magnetic flux through it, which in turn causes leakage of the magnetic fields at the discontinuities. Two perpendicular magnetic fields are used to detect the discontinuities because no indication is formed if orientation of discontinuities is parallel to the magnetic field. The limitation of this method is applicable only to ferromagnetic materials. It can not be used to detect defects in austenitic steels such as austenitic stainless steels and high manganese steels.

2.3.3.4 Radiographic Inspection

Radiographic inspection is the method capable of detecting the external or internal discontinuities using X-rays or gamma rays to penetrate a part to inspect any discontinuities that produce a permanent image on a film. Because of difference density and differences in absorption characteristics caused by variation in composition, different portions of an object absorb different amounts of the penetrating radiation. In general, radiography can detect only those features that have an appreciable thickness in a direction parallel to the radiation beam. This method is expensive and hazardous resulting in special precautionary measures which must be taken when entering or approaching a radiographic area.

2.3.3.5 Ultrasonic Inspection

Ultrasonic inspection is a technique in which beams of high frequency sound waves (100 kHz – 25 MHz) are introduced into a material for the detection of external and internal discontinuities. The sound waves travel through the material with some attendant loss of energy (attenuation) and are reflected at interfaces. The reflected beam is displayed and

then analyzed to define the presence and location of discontinuities. Cracks, laminations, internal porosities, lack of fusion, incomplete penetration that produce reflective interface can be easily detected. Inclusions and other homogeneities can also be detected by causing partial reflection or scattering of the ultrasonic waves.

2.4 SAW Process Variables

The welding process variables are the main factors influencing the properties of weldments, such as the bead size, penetration depth, HAZ size, weld defects, strength and toughness. The following sections will discuss each variable and its effect on the properties of weld joints.

2.4.1 Heat Input

Three variables govern the heat input to the workpiece, irrespective of whether the heat is applied on the weldment surface or internal to the weldment. These are: (1) the heat input, (2) the heat distribution, and (3) the weld travel speed. The heat input per unit length is calculated according to the following equation [31]:

$$H = \frac{KVA}{1000S} \qquad 2.2$$

where H = the welding heat input (kJ/mm), V = arc voltage (V), A = welding current (A), S = travel speed (mm/s) and K = coefficient of welding efficiency.

Usually, SAW has a high K value while GTAW has a low K value. Both SMAW and GMAW have an intermediate K value [19]. It is generally reported that the hardness of weld metal and HAZ decreases with increasing heat input. Generally, automated welding processes such as SAW and GMAW require constant voltage power supply so that one can hold the voltage constant and vary the welding current. Thus welding current and

travel speed are the main factors controlling heat input [32]. Nowacki and Rybicki [31] reported that welds with heat input up to 3.0 kJ/mm reduced weld imperfections such as slags, lack of penetration, and cracks. In newly developed high toughness steels, it is vital that the lowest possible heat input is maintained during welding so as not to unduly affect the weld metal and the HAZ properties. The mechanical properties, particularly toughness of high heat input welds, are known to be inferior to toughness due to grain coarsening in the HAZ and segregation in the weld metal. Thus, any attempt to increase productivity by increasing the heat input is at the expense of the mechanical properties. This factor is becoming increasingly more important due to the emergence of high strength and heat-input-sensitive materials such as HSLA steels [32]. Theoretically, the heat input can be reduced by increasing the travel speed. It is reported by Chandel and Bala [33] that the weld defects, such as undercuts and lack of penetration, will occur when the travel speed is high.

2.4.2 Arc Voltage

Although it is reported that the arc voltage has no significant effect on the HAZ dimension, the shape of the weld bead cross-section is controlled by the arc voltage [34]. The arc length increases with increasing arc voltage and vice versa. If the welding current and travel speed are kept constant, the heat input will be almost constant because the change of arc voltage has little effect on the heat input. The amount of the flux melted increases with increasing arc length. Therefore, an increase in the arc voltage will result in flat and wide weld beads forming to reduce porosities caused by rust and mill scale [35].

2.4.3 Welding Current and Wire Feed Speed (WFS)

If all other SAW parameters are kept constant, then welding current and wire feed speed (WFS) are directly related to each other because welding current increases with increasing WFS, and vice versa [34].

Welding current and WFS control wire melting rate, depth of penetration, and dilution of parent metal (i.e., mixing of the base metal, wire material and flux). Very high a welding current or WFS, at a given travel speed, will result in a large depth of fusion or penetration. The weld may penetrate so deep that molten metal may go through the backing to cause unwanted weld defects. It will also cause excessive reinforcement, large weld shrinkage, increased stress, and a high chance of distortion. Gunaraj and Murugan [36] reported that depth of penetration, reinforcement size and dilution increase with increasing WFS, while weld bead width is unaffected. Equation 2.2 shows that heat input increases with increasing welding current. Therefore, if other welding parameters are fixed, high welding current translates to high heat input. Lee *et al*. [37] reported that for a given heat input, the HAZ-to-bead size ration decreases as the welding current increases. Although the weld bead size and HAZ size increase with the increasing welding current, there is a greater increase in the bead size compared to the HAZ size. Yang *et al.* [38] reported that for a particular electrode diameter and extension, the bead width increases initially as the current is increased up to a maximum after while it decreases as the welding current is increased further.

2.4.4 Travel Speed

Travel speed (i.e., the speed of the welding equipment across the sample) is one of the most important variables affecting penetration and bead size. Gunaraj and Murugan [37] reported that the weld bead width and depth of penetration decrease with increasing welding speed. Yang *et al.* [38] however reported that bead width increases initially as the welding speed is increased up to a maximum size, after which it decreases as the speed is increased. Surface defects such as undercut, arc blow, porosity and non-uniform bead shape result from the high travel speed [33]. Using appropriate travel speed gives gases enough time to escape from the molten metal before it solidifies, hereby reducing porosity. Very low travel speed leads to uncontrollable molten pool which will result in rough bead and possible slag inclusions. For single-pass welds, the current and travel speed can be as high as possible and still give proper weld bead size and penetration

depth without burning through. In multiple-pass welds, the travel speed can be varied to obtain the desired fill for the joint [34].

2.4.5 Wire Size

The electrode wire diameter affects the deposition rate. Normally, the small wire size requires lower welding current than the large wire. If kept the welding current constant, the small wire has higher current density than a larger wire. For a given diameter, a high current gives a high current density with deep penetration of the base plate while a low current gives a less penetrating arc. Wire size also affects arc starting. Small diameter wire arc starts are more consistent than those of big diameter wire [30]. Yang *et al.* [38] reported that a large electrode diameter encourages large bead width at high currents (600 A to 1000 A).

2.4.6 The Flux

The flux used in SAW is similar to the coating of electrodes used in SMAW to protect the melting metal from oxidation and add small amounts of elements into the metal to get good quality welds. The composition of the granular fusible flux includes oxides of Mn, Si, Ti, Al, Ca, Zr, Mg and other compounds [33]. The weld metal chemistry is affected by the electrochemical reactions at the weld pool-flux interface. The main characteristics of SAW are affected by the flux type and its physicochemical properties [39]. Butler and Jackson [40] reported that calcium ions in fluxes increase the electric arc stability. It is also known that quartz and corundum increase the viscosity of flux, while the addition of manganese oxide, calcium fluorite and titanium oxide reduce viscosity [41]. Manganese oxide and quartz have been observed to have a beneficial effect on the mechanical properties of welds [42]. Titanium oxide can promote the formation of AF, which is less susceptible to cracking [26, 43]. In order to obtain the desired properties of the weld metal, the flux must be formed to be compatible with a given electrode wire type. SAW

fluxes can be divided into four categories according to their basicity index which is calculated using the Tuliani's formula [44].

$$B = \frac{\%CaO + \%MgO + \%BaO + \%SrO + \%Na_2O + \%K_2O + \%Li_2O + \frac{1}{2}(\%MnO + \%FeO)}{\%SiO_2 + \frac{1}{2}(\%Al_2O_3 + \%TiO_2 + \%ZrO_2)} \qquad 2.3$$

where B = basicity index and % refers to wt.%. Basicity index ranges are classified as follows: acid, < 1; neutral, 1-1.5; semibasic, 1.5-2.5; and basic, > 2.5.

B can be adjusted with the contents of elements such as silicon, sulfur, and oxygen in the weld metal. Comparing the different types of fluxes, semibasic fluxes have more advantages than others due to their low oxygen content, excellent toughness and good operating characteristics. The toughness of the weld metal is reduced because of high oxygen levels coming from acid fluxes. Low weld quality is also caused by low oxygen levels coming from basic fluxes. It is reported by Thomas Jr. [45] that semibasic fluxes give desirable welding conditions and high toughness at low temperatures. The content of Mn and Si in the fluxes are strictly controlled because Mn or Si may cause a harmful effect on microstructural distribution [43].

2.4.7 Preheat and Interpass Temperatures

Preheat is essential for steels with high CE (> 0.45%) or larger thickness. The purpose of preheat is to reduce shrinkage stresses in the weld, prevent excessive hardening, and provide a slow rate of cooling through the 204 ^{o}C (400 ^{o}F) to allow hydrogen diffusion away from the weld and adjacent zone [15, 46, 47]. For a multiple-pass weldment, the interpass temperature is defined as the temperature of the work piece before each weld run is deposited. The interpass temperature between weld passes must be kept in the same range as the preheating temperature. Increasing preheat or interpass temperatures causes a reduction in strength, but increases low temperature toughness. Although a high interpass temperature has little effect on the cross-sectional area of the weld bead, the proportion of

recrystallized area increases with increasing interpass temperature [48]. Recently, Lord [49] reported that both chemical composition of steel and process parameters such as interpass temperature are the factors that can alter the yield strength of high strength steel weldments .

2.4.8 Post Weld Heat Treatment Temperature

Post weld heat treatment (PWHT), also called stress-relief heat treatment, is defined as heating the weldment to a suitable temperature, holding long enough to reduce the residual stresses and then cooling slowly enough to minimize new residual stresses. PWHT is done after welding in order to obtain such desirable material properties as hardness and strength. Most of the SAW products in use today are designed to be used in the as-welded condition, or after simple stress relieving heat treatment [50]. In most cases, manufacturers and repair organizations routinely specify a temperature range (645 ± 14 °C) and a minimum holding time (24 min/cm, 15 minutes minimum) [51]. Low temperatures with long hold time can also be used to get better mechanical properties.

Most of the work on PWHT of HSLA steels carried out in the past has concentrated on the effect of stress-relieving on weld metal toughness in the presence of microalloying elements such as Nb and V, which are diluted from the parent metal [52, 53]. Croft *et al.* [50] reported that a significant increase in impact transition temperature (ITT) was observed after stress relieving for 1 hour at 650 ^{o}C. This was associated with the precipitation of Nb(C,N) particles both within the individual grains of acicular ferrite and at the high angle acicular ferrite boundaries.

2.5 Welding Performance

Welding performance of the weldment is evaluated by three parameters, namely: deposition rate, hardness, and dilution [36]. The bead shape parameters necessary for determining welding performance are shown in Figure 2.12, where *R* is the

reinforcement, b is the weld bead width, P is the penetration depth, and w is taken as the HAZ size. The bead contact angle, θ, is defined as $(\theta_1+\theta_2)/2$.

From these measurements, the area of penetration (A_p), which is the cross-sectional area of the weld deposit below the surface of the parent metal, the deposition area (A_d) (or reinforcement area (A_r)), and the area of the HAZ (A_{HAZ}) can be determined. The deposition rate (R_d) is the weight of metal deposited per unit time and is calculated according equation 2.4 (Appendix B1 shows the derivation):

$$R_d = \rho A_d S \qquad 2.4$$

where R_d is deposition rate (g/s), ρ is the density of the welding metal (g/mm^3), A_d is the deposition area (mm^2) and S is the travel speed (mm/s).

The deposition rate is an important variable in welding economics. A high deposition rate results in a fast speed or a short time for welding. Short welding time can reduce labor costs. The hardness of the weldment is determined by taking hardness measurements in the longitudinal and transverse directions. Moon *et al.* [54] reported that the HAZ is the

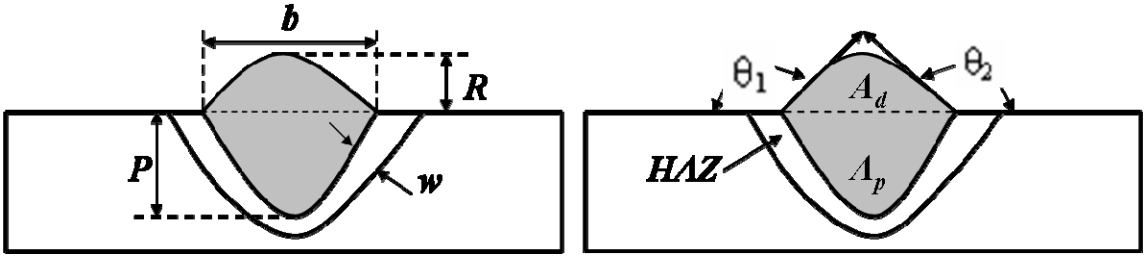

Figure 2.12. Schematic illustration of the measurements required for determining welding performance.

hardest region in every weldment, regardless of the filler metal type, base metal or heat input, and that the hardness reaches a maximum value midway through the HAZ.

Dilution is defined as the ratio of A_p to the total area of the weld metal (A_f) [55]. The interactions between welding parameters and bead parameters as well as the interactions between welding variables and welding performance parameters are usually determined statistically by means of analysis of variance (ANOVA) [36].

2.6 Weld Melting Efficiency

Welding parameters influence the size of the weld bead and the HAZ differently and this is attributed to the way these parameters affect the various melting efficiencies. The HAZ is an undesirable but unavoidable region in a fusion weld joint because of the heat transfer from the weld metal to the parent metal. To a certain extent, the HAZ size reflects on the grain coarsening and toughness [37]. Poor toughness can result from the large grains in a large/wide HAZ. On the other hand, a narrow HAZ indicates a steep thermal gradient and thus a fast cooling rate and a short soaking time as well as fine grain size and high toughness [37].

The effect of welding process variables on electrode melting and plate melting efficiencies of submerged arc welding has been variously studied and it was found that there is an increase in the plate melting efficiency (PME) with increasing welding current and voltage. On the basis of the work of Niles and Jackson [56], Chandel [57] derived parameters for quantifying weld melting efficiency. In the analysis, the percentage of energy consumed in melting the electrode is called the electrode melting efficiency (EME), whereas that consumed in melting the base metal is called the PME. The sum of these two efficiencies is termed the welding process melting efficiency (WPME). Equations for calculating the three melting efficiencies for submerged arc welding are given as follows [57]:

$$EME(\%) = \frac{100SA_d}{0.0854VI} \qquad 2.5$$

$$PME(\%) = \frac{100S\left(A_f - A_d\right)}{0.0854VI} \quad 2.6$$

$$WPME(\%) = \frac{100SA_f}{0.0854VI} \quad 2.7$$

where V = the welding voltage (V), I = the welding current (A), S = the travel speed (mm/min), A_d = the deposition area (mm^2), and A_f = the total fusion area.

Lee *et al.* [37] reported that the HAZ size related to the PME. The welding parameters that promoted the plate melting will increase the HAZ size. They assumed that most of the heat from the deposition area melted the flux, while almost all the heat from the parent metal melting formed the HAZ.

3 MATERIALS AND EXPERIMENTAL METHODS

The materials and experimental techniques used in this study are described in the following sections.

3.1 Materials

Two materials were used in this study, namely: pressure vessel (PV) steel (ASME SA516 Grade 70), and wind turbine tower (WT) steel (ASTM A709 Grade 50). The former material was tested in the as-rolled condition, while the latter was tested in the normalized condition. Both materials were supplied as plates measuring 915 mm x 122 mm x 17 mm. Table 3.1 shows the chemical compositions of both materials based on the test certificates documents provided by Hitachi Canadian Industries (HCI) Ltd., Saskatoon.

3.2 Welding Procedure and Parameters

The SAW technique was used to fabricate all experimental weldments analyzed in this work. The weld joints are no-bevel butt welds with single pass per side. Figure 3.1 shows the diagram of a typical weld joint. All the plates were welded by the personnel of HCI, Saskatoon.

The electrode used for welding the plates was ESAB, Spoolarc 81, which is classified by the American Welding Society (AWS) as No. EM12K. This electrode is a manganese-containing electrode manufactured from silicon-killed steel. The chemical composition is given in Table 3.2 based on the documents provided by HCI.

Table 3.1. Chemical compositions of ASME SA516 and ASTM A709 steels.

Material	Elements (wt. %)											
	C	Mn	Si	S	P	Cu	Cr	Ni	Mo	Nb	V	Ti
SA516	.22	1.14	.24	.008	.019	.02	.01	.01	.002	---	---	.004
A709	.04	1.3	.06	.007	.01	.31	.31	.14	.04	.045	.003	0.01

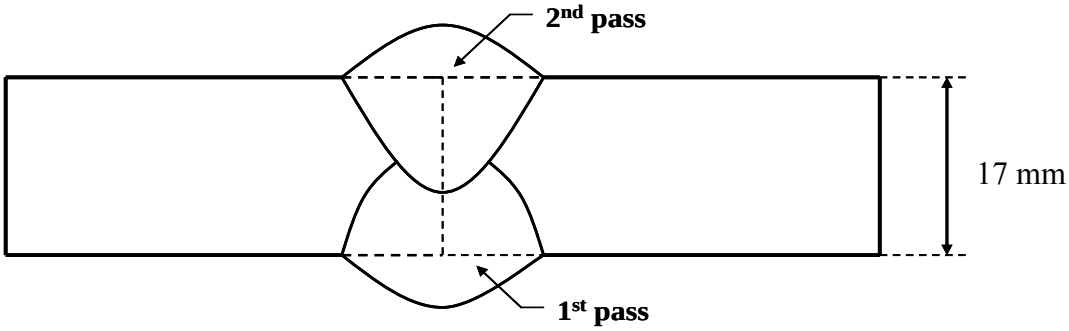

Figure 3.1. Schematic drawing showing the SAW weld joint geometry.

Table 3.2. Chemical composition of AWS No. EM12K.

Material	Elements (wt. %)						
	C	Mn	Si	S	P	Cu	Others
EM12K	0.10	0.99	0.24	0.01	0.006	0.13	< 0.50

The flux used in the welding was ESAB OK 10.72, which is classified by the AWS as F7A6-EM12K-H8. This flux, an agglomerated aluminate-basic flux, is designed especially for applications with good toughness requirements at low temperatures. Its basicity index is 1.9. The chemical composition is given in Table 3.3 based also on the documents provided by HCI.

Table 3.3. Chemical composition of the flux.

Material	Elements (wt. %)			
	SiO_2+ TiO_2	CaO + MgO	Al_2O_3+ MnO_2	CaF_2
ESAB OK 10.72	20	25	30	20

The *CEs* of SA516 and A709 are 0.41 and 0.38, respectively. Since they are less than .45, no post-weld heat treatment was applied to the weldments. For obtaining sufficiently wide range of weld heat input, three welding currents and four travel speeds were used to weld the steel plates. The SAW process parameters that were used for both materials are shown in Tables 3.4 and 3.5, respectively.

3.3 Experimental Methods

Eight principal experimental methods were used to evaluate the weld quality and mechanical properties of the test materials in this work. These include: nondestructive tests (visual and ultrasonic examinations), weld geometry measurements, microhardness measurements, metallographic examination, Charpy impact test, lateral expansion measurements, tensile testing and Scanning Electron Microscopy (SEM).

3.3.1 Nondestructive Tests

In this work, surface defects were evaluated by visual examination, while internal defects were studied by ultrasonic examination.

3.3.1.1 Visual Examination

Direct visual examination was used for inspecting such features as surface conditions of the weldments, undercut, excessive reinforcement, alignment of mating surfaces and

Table 3.4. SAW parameters used for SA516 steel plate.

SA516 Gr.70	Weld current (A)	Weld voltage (V)	Speed (mm/s)	Preheat Temp. (^{o}C)	Interpasss Temp. (^{o}C)
PV-1	700	35	5.9	20	107
PV-5	800	35	5.9	20	107
PV-6	800	35	9.2	20	70
PV-7	800	35	12.3	30	107
PV-8	800	35	15.3	20	100
PV-9	850	35	5.9	35	75
PV-10	850	35	9.2	30	75
PV-11	850	35	12.3	30	100
PV-12	850	35	15.3	30	60

Table 3.5. SAW parameters used for A709 steel plate.

A709 Gr.50	Weld current (A)	Weld voltage (V)	Speed (mm/s)	Preheat Temp. (^{o}C)	Interpasss Temp. (^{o}C)
WT-1	700	35	5.9	20	107
WT-2	700	35	9.2	20	107
WT-3	700	35	12.3	20	80
WT-4	700	35	15.3	20	80
WT-5	800	35	5.9	20	107
WT-6	800	35	9.2	20	75
WT-7	800	35	12.3	25	107
WT-8	800	35	15.3	20	100
WT-9	850	35	5.9	30	100
WT-10	850	35	9.2	30	70
WT-11	850	35	12.3	36	70
WT-12	850	35	15.3	40	60

weld bead shape. The evaluation method and acceptance criteria adopted in this study were the 2004 ASME Boiler and Pressure Vessel Code, Section V, Article 9 [58].

3.3.1.2 Ultrasonic Examination

Ultrasonic test was conducted using a Panametrics Epoch III Model 2300 Ultrasonic flaw detector with 60^{o} and 70^{o} angle beam transducers. The coupling medium was Ultragel II couplant. In order to establish a general level of consistency in measurements, an International Institute of Welding (IIW) Type I reference standard block was used to calibrate the equipment range and sensitivity. The Distance Amplitude Correction curve (DAC) was set up using an A709 steel reference block with eight artificially induced 2.5 mm diameter holes. All defects reflectors that produced a response equal to or greater than 20% of the DAC curve were recorded according to the 2004 ASME Boiler and Pressure Vessel Code, Section V, Article 4 [59].

Figure 3.2 shows a schematic of the ultrasonic testing equipment using angle beam transducers. In order to improve detectability of flaws in and around welded areas, the direct sound beam and sound beam to be reflected from the back wall were used in this work. Figure 3.2 (a) shows the identification of the location of a flaw once the unacceptable defect reflectors are generated. Figure 3.2 (b) shows the total skip distance from the edge of the weld. Ultrasonic test using was performed on both sides of the plate using two angle transducers to avoid the defects being omitted. The unacceptable categories and dimensions of the flaw were calculated using the recorded data during the ultrasonic testing.

3.3.2 Weld Geometry Measurements

In order to keep the measured data consistent, the locations on the samples with severe surface defects such as burn through and excessive reinforcement were avoided. The

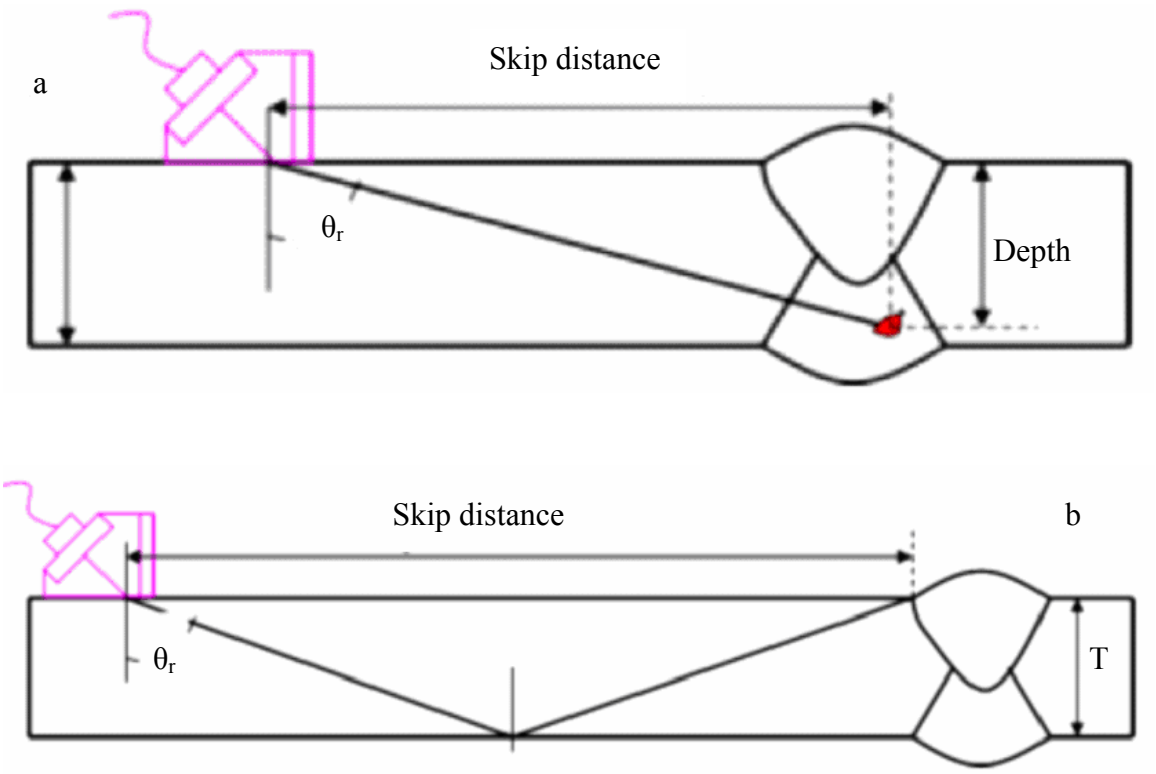

Figure 3.2. Sketches of the ultrasonic test: (a) identification of the location of a flaw using direct sound beam, (b) identification of total skip distance using sound beam reflected from the back wall.

bead width, reinforcement and contact angle were measured on both sides of the plates. In order to get enough data for the analysis, eight locations were randomly selected along the plate. Figure 3.3 shows the locations for the measurement marked with white arrows. The regions with very severe surface defects were marked with white rectangles.

Other weld geometry measurements were performed from transverse cross sections that were polished and etched using 2% nital before examination under an optical microscope. Figure 3.4 shows the typical cross section pictures for geometry measurement. Using the IMAQ Vision Builder 5.0 software, the bead width, reinforcement, penetration size, HAZ size, contact angle, deposition area (A_d), and penetration area (A_p) were measured once the picture was downloaded into this software. For each weldment, three cross-sectioned

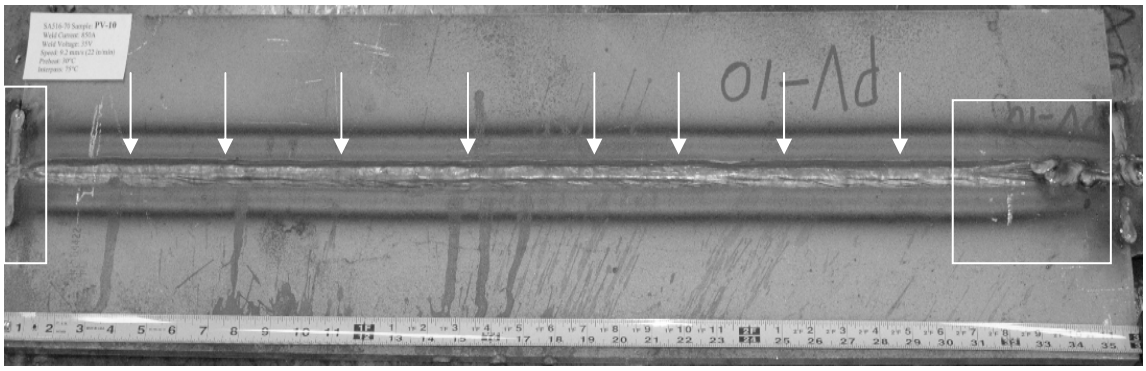

Figure 3.3. Identification of the regions where weld geometry measurements were conducted.

Figure 3.4. Typical etched cross-sections used for geometry measurements.

specimens were prepared for geometry measurements. Figure 3.5 shows a typical section of area measurement during the experiment after the calibration was completed. The thickness of the plate measured using software was set the same as the value measured using a calibrated caliper. Once all these geometry measurements were completed, EME, PME and WPME could be determined.

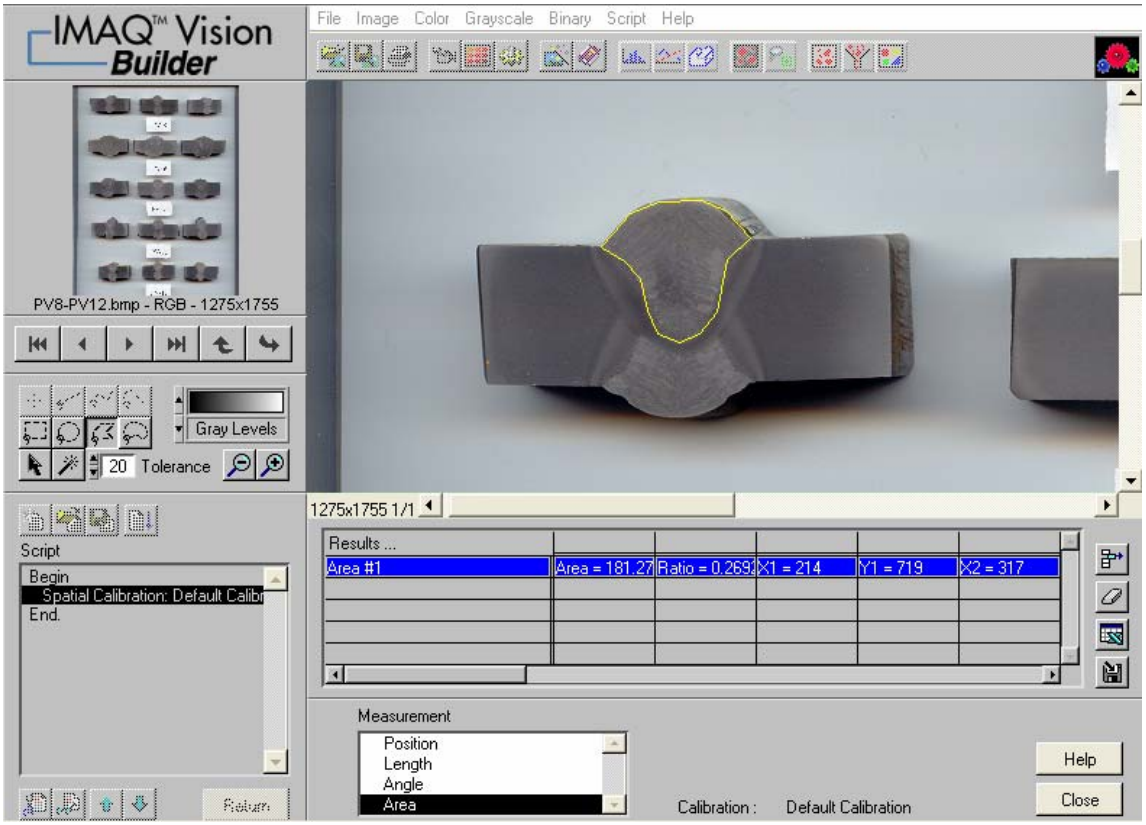

Figure 3.5. Typical area measurement using the IMAQ Vision Builder 5.0 software.

3.3.3 Metallographic Examination

The microstructures of the PM, FGHAZ, CGHAZ, WI, and WM zone of SA516 and A709 were studied by metallographic examination. The primary objective here was to examine the microstructures and to establish the relationship between the mechanical properties and microstructures of both materials. All the specimens used for metallographic examination were initially ground using emery papers of different grit sizes and subsequently polished using 1 μm diamond paste on a nylon cloth followed by etching in 2 vol. % Nital. The microstructures of the polished and etched specimens were studied using an optical microscope.

3.3.4 Microhardness Measurements

Hardness measurements were carried out on polished and etched specimens using a Buehler Vickers Microhardness Tester - Micromet II. The indentation load was 200 g and the resident time was 15 seconds. Transverse hardness readings were taken across the PM, FGHAZ, CGHAZ and WM on both passes as shown in Figure 3.6. At least 15 readings were taken in each region. The two base diagonals of the pyramid imprinted on the specimen by the indenter were measured. Calculation of the Vickers hardness number was based on the average length of the diagonals. Diagonal length values that differed by more than 5 μm were discarded to avoid too much fluctuation.

3.3.5 Charpy Impact Testing

For Charpy impact testing, transverse specimens were machined in accordance with ASTM E23 standard [60]. The dimensions of Charpy impact test specimens are shown in Figure 3.7. To distinguish between the weld metal and HAZ of the weldments, the blank Charpy specimens without grinding and polishing were etched using 5% nital. These were then notched in the weld metal center and HAZ in accordance with the 2004 ASME Boiler and Pressure Vessel Code, Section III, Division 1, Subsection NB [61]. The notch of the HAZ specimens was cut in such a manner as to include as much HAZ as possible to ensure that the tip of the notch was in the HAZ.

In order to establish the ductile-to-brittle transition temperature (DBTT) or impact transition temperature (ITT) for each weldment, the specimens were tested at temperatures ranging from -196 ^{o}C to 100 ^{o}C. The actual temperatures used were: -196 ^{o}C, -80 ^{o}C, -60 ^{o}C, -45 ^{o}C, -30 ^{o}C, -15 ^{o}C, 0 ^{o}C, 25 ^{o}C, 60 ^{o}C and 100 ^{o}C. The information obtained from this test included the absorbed energy and lateral expansion. The absorbed energy of each weldment was compared with the absorbed energy of the parent metal. These results were used to qualify SA516 and A709 weldments for use in low temperature applications. The lateral expansion measurements are introduced in 3.3.6.

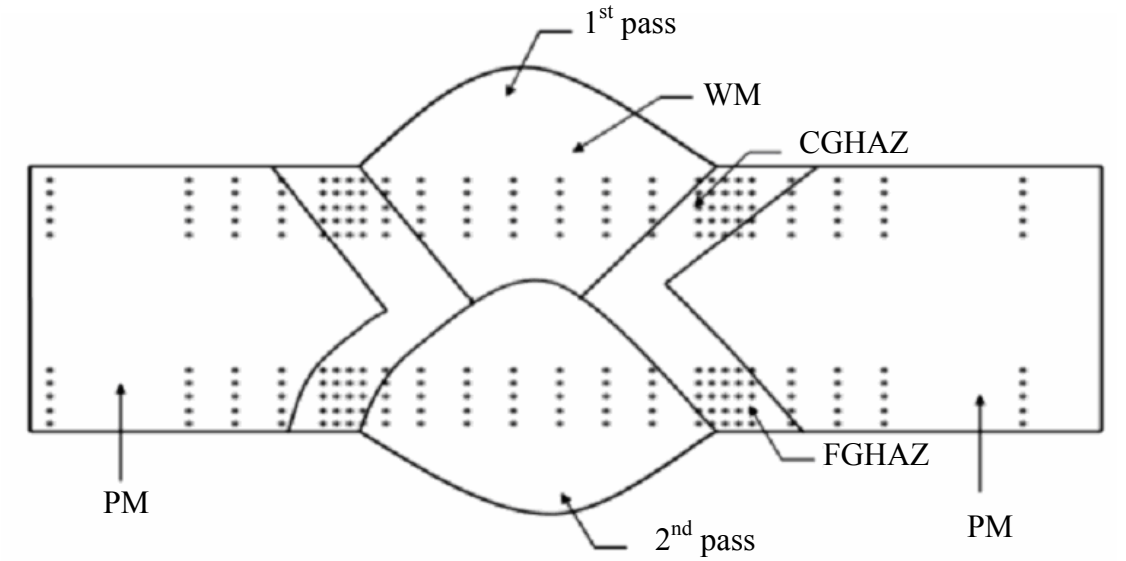

Figure 3.6. Illustration of transverse hardness measurements on the weldment.

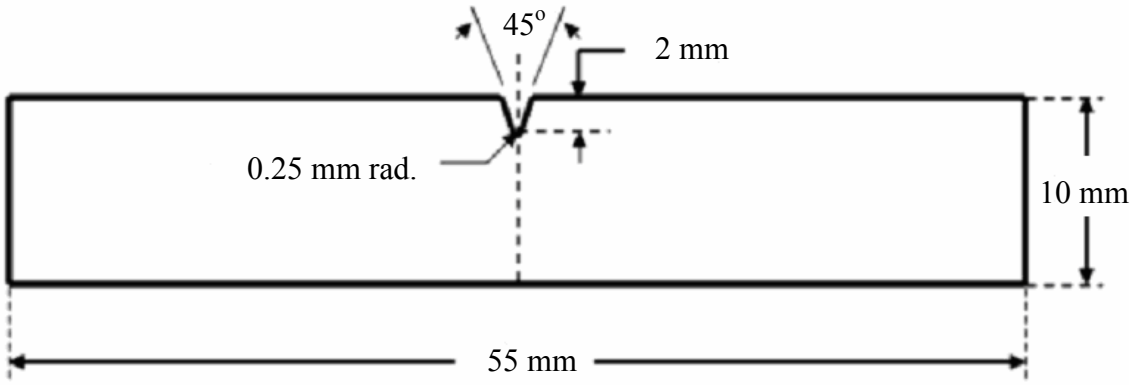

Figure 3.7. Sketch of a Charpy (single-beam) impact test specimen.

3.3.6 Lateral Expansion Measurements

According to the requirement of ASTM E23, two halves of fractured Charpy impact specimens were used in lateral expansion measurements. Since half of a broken specimen

may include the maximum expansion for both sides, one side only or neither, the expansion on each side of each half of the specimen was measured separately. Therefore, the lateral expansion measurements must provide an expansion value equal to the sum of the higher of the two values obtained for each side. As shown in Figure 3.8, if A_1 is greater than A_2, and A_3 is less than A_4, then the lateral expansion is the sum of $A_1 + A_4$. If the two halves of the specimen halves have burrs which will influence the measurements, they should be removed. The lateral expansion measurements must meet the requirement of ASTM E23 [60].

3.3.7 Tensile Testing

The standard rectangular tensile specimen was prepared in accordance with ASTM A370 [62]. Dimensions of a standard tensile test specimen are shown in Figure 3.9. Three tensile specimens were produced from defect-free sections of each welded plate. If the welded plated had internal defects such as lack of penetration, three additional tensile specimens were prepared from the defective regions to investigate the effect of weld defects on the strength of the weldments. All of the specimens were tested using an Instron Universal Testing machine, Floor Model 5500R (Figure 3.10).

3.3.8 Scanning Electron Microscopy

Fractured Charpy v-notch impact samples from SA516 and A709 tested at various temperatures were examined in a JEOL JSM840A Scanning Electron Microscope (SEM) (Figure 3.11). Valuable information regarding the mechanism and nature of the fracture such as inclusions and brittle and ductile fracture features were determined through this experiment.

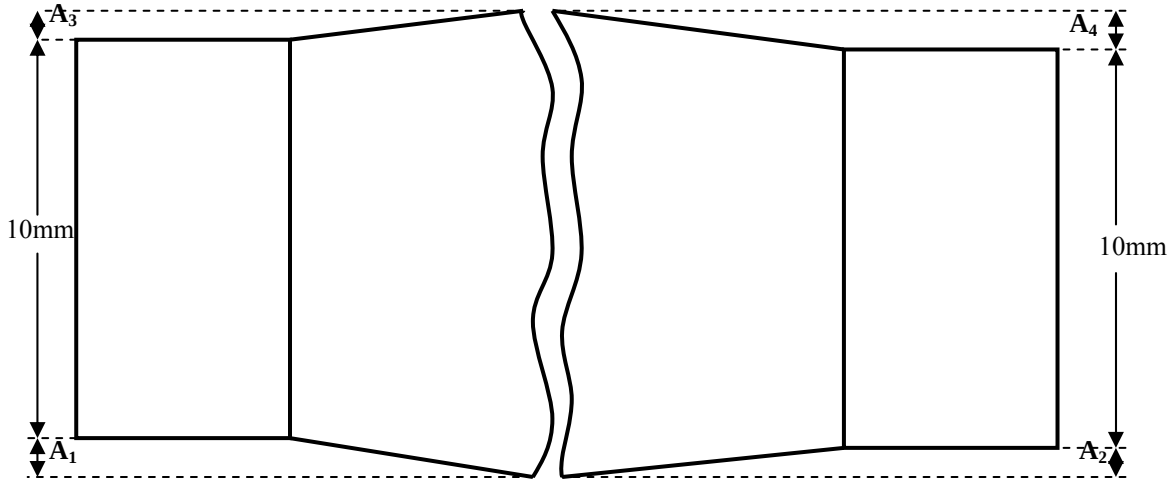

Figure 3.8. Sketch of lateral expansion measurement using fractured Charpy impact specimen haves [60].

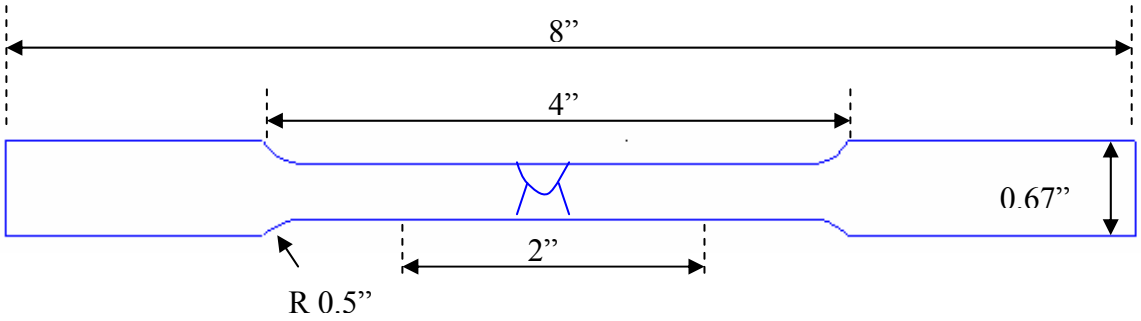

Figure 3.9. Sketch of a typical tensile test specimen [62].

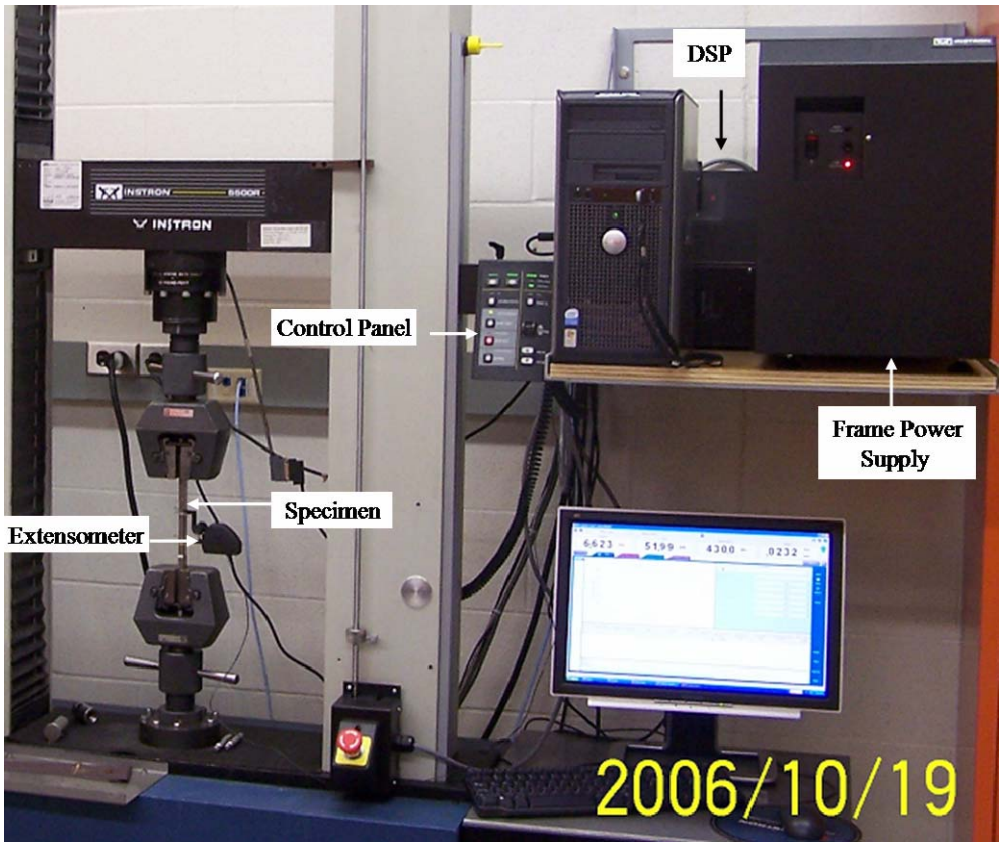

Figure 3.10. Instron Universal Testing Machine – Floor Model 5500R.

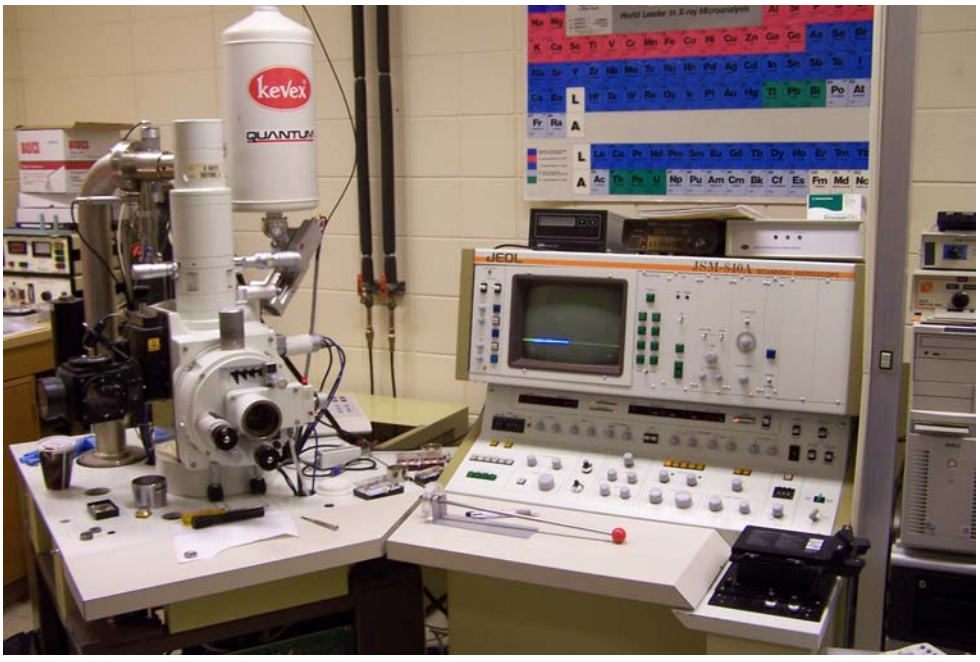

Figure 3.11. A picture of JEOL JSM 840A Scanning Electronic Microscope.

4 RESULTS AND DISCUSSION

This chapter presents and discusses the results obtained from the various experiments that were carried out in this study. The analysis of the results will lead to a better understanding of the relationship between SAW process parameters and properties of A709 and SA516 weldments.

4.1 Weld Bead Geometry

The relationship between SAW parameters and weld bead geometry is complex because a number of factors are involved such as welding current and travel speed. The effect of welding current and travel speed on weld reinforcement, bead width, penetration size, contact angle and heat affected zone size of SA516 and A709 weldments was investigated. The relationships between these geometrical factors and SAW parameters were determined.

4.1.1 Effect of Welding Current

Figures 4.1 to 4.5 show the effect of welding current on the reinforcement, bead width, contact angle, penetration depth, and HAZ size of SA516 weldments, respectively. The relationships between the welding current and these geometry parameters for A709 are shown in Figures 4.6 to 4.10. The error bars in all figures are standard deviations of the measurements. Since the trend of the first pass is similar to that of second pass in one weldment, only the trend of one pass was shown in some figures. As can be seen, Figures 4.1, 4.4, 4.5, 4.6, 4.9 and 4.10 indicate that the reinforcement, penetration depth and HAZ

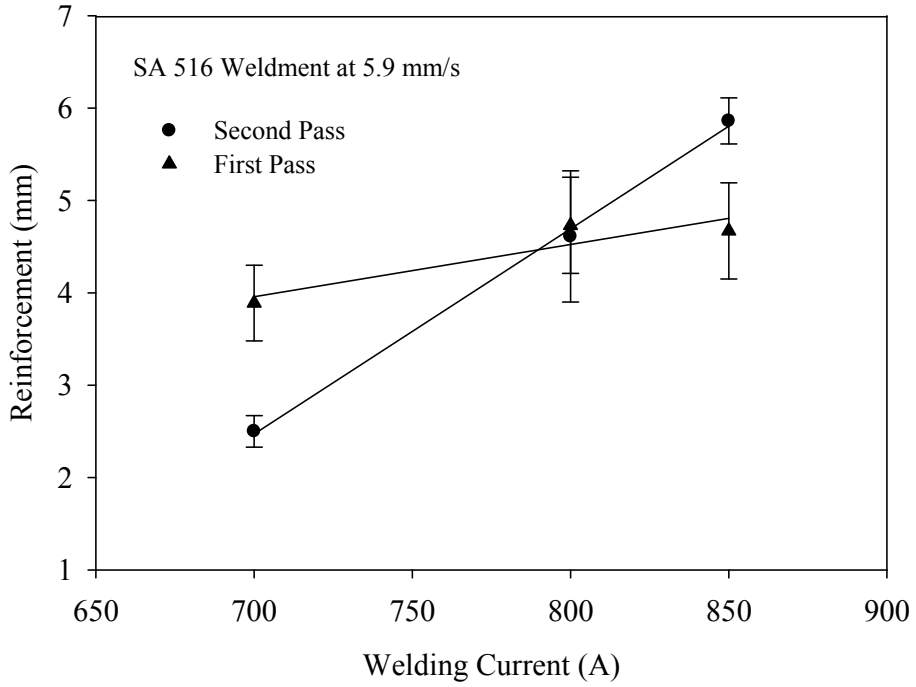

Figure 4.1. Effect of welding current on the reinforcement of SA516 weldment.

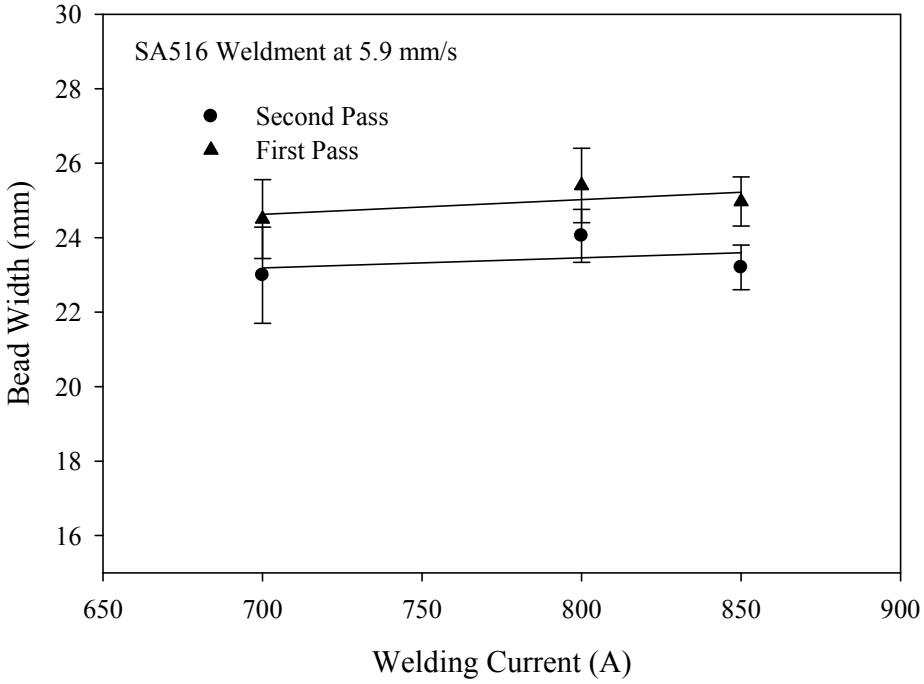

Figure 4.2. Effect of welding current on the bead width of SA516 weldment.

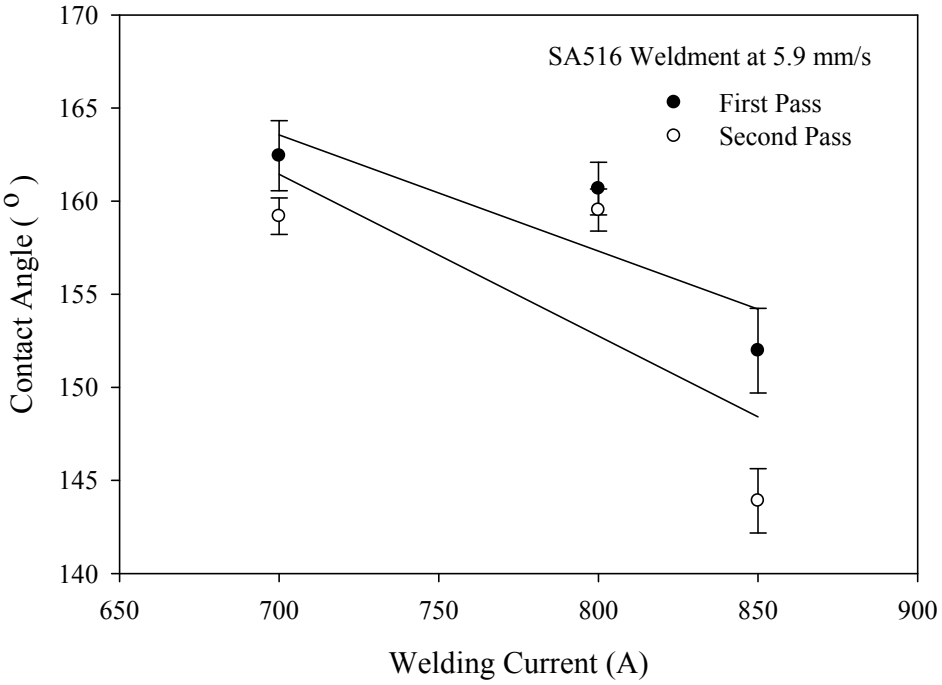

Figure 4.3. Effect of welding current on the contact angle of SA516 weldment.

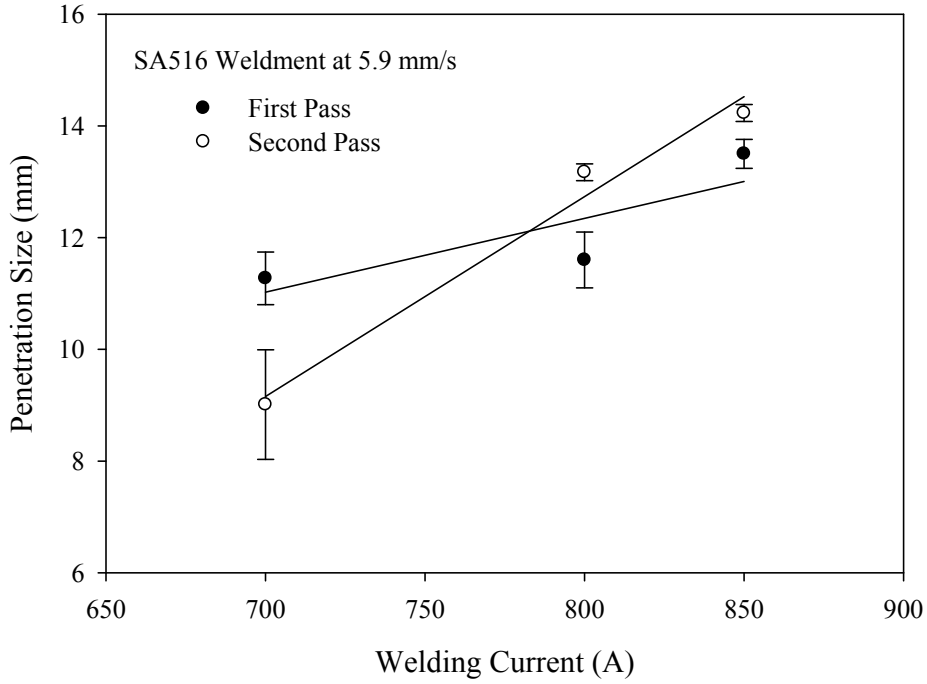

Figure 4.4. Effect of welding current on the penetration depth of SA516 weldment.

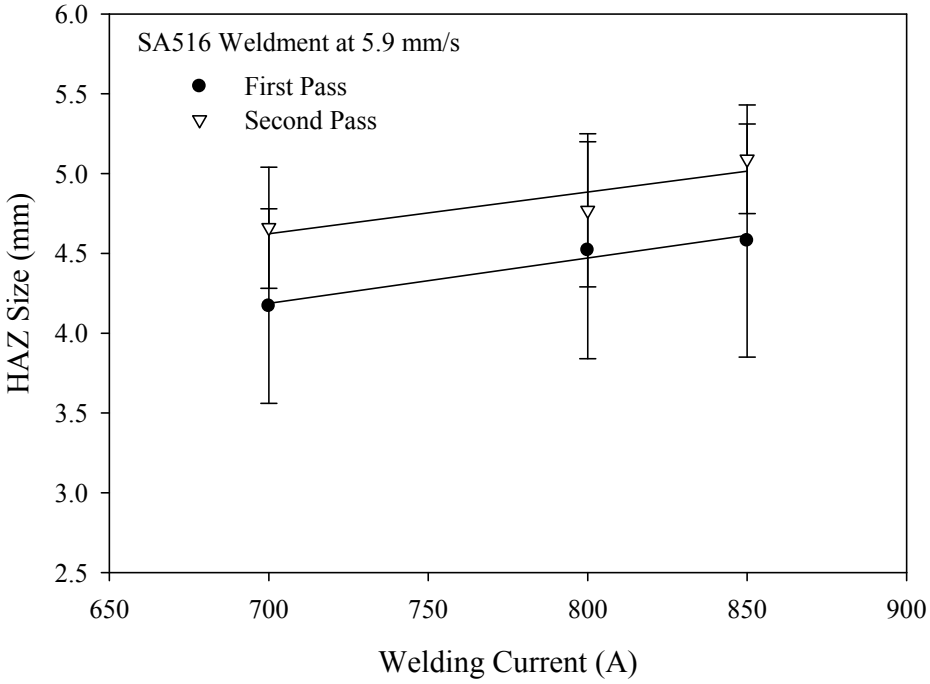

Figure 4.5. Effect of welding current on the HAZ size of SA516 weldment.

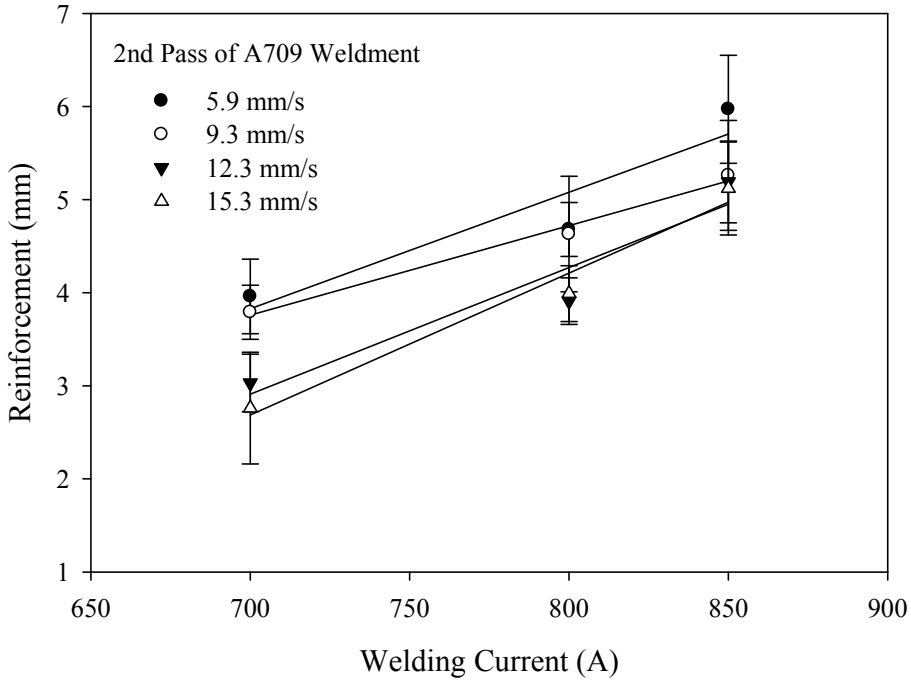

Figure 4.6. Effect of welding current on the reinforcement of A709 weldment.

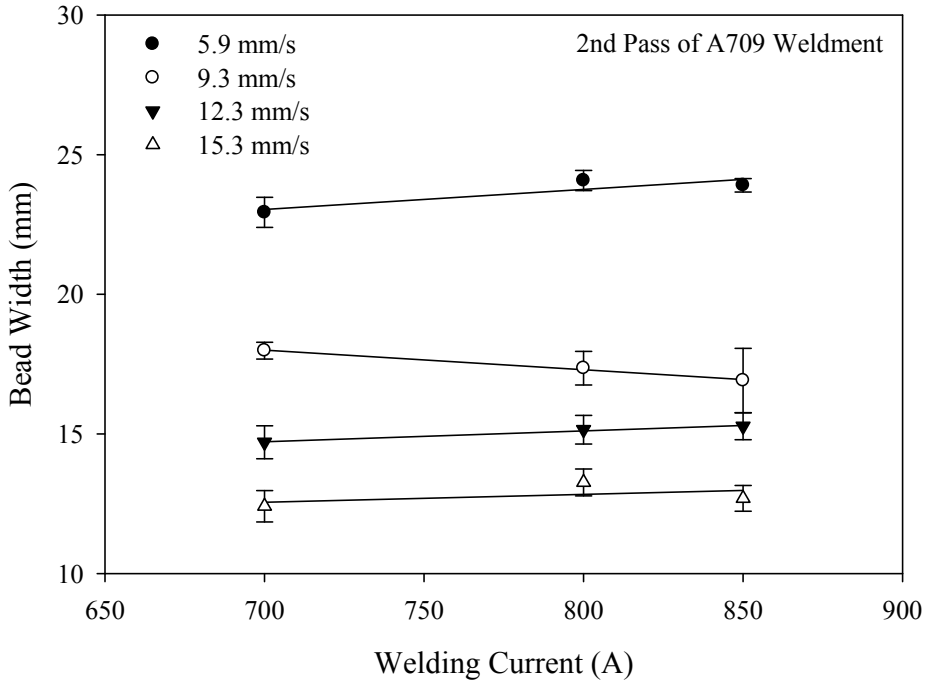

Figure 4.7. Effect of welding current on the bead width of A709 weldment.

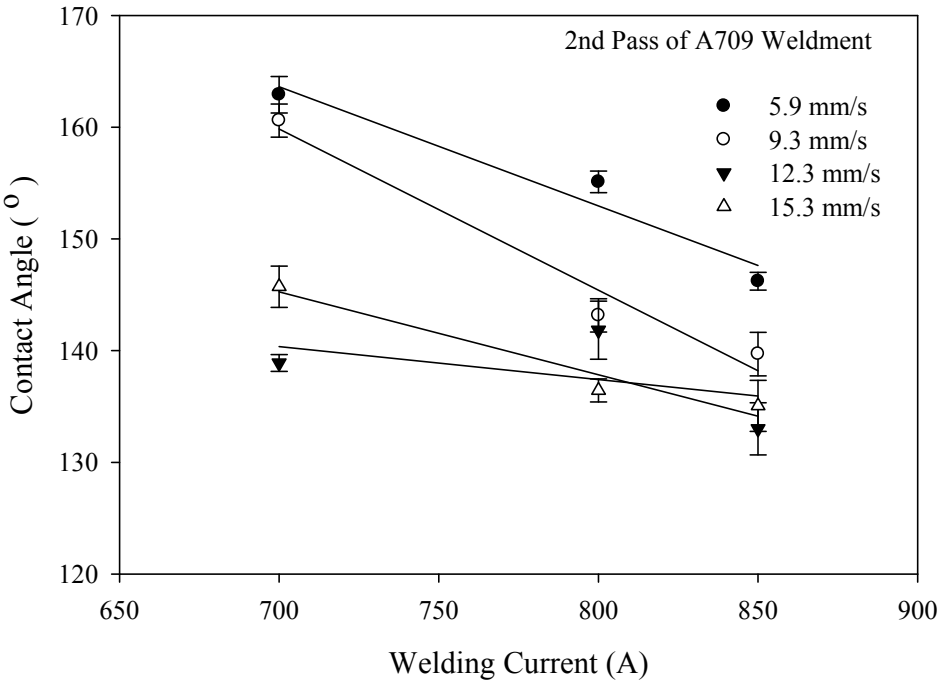

Figure 4.8. Effect of welding current on the contact angle of A709 weldment.

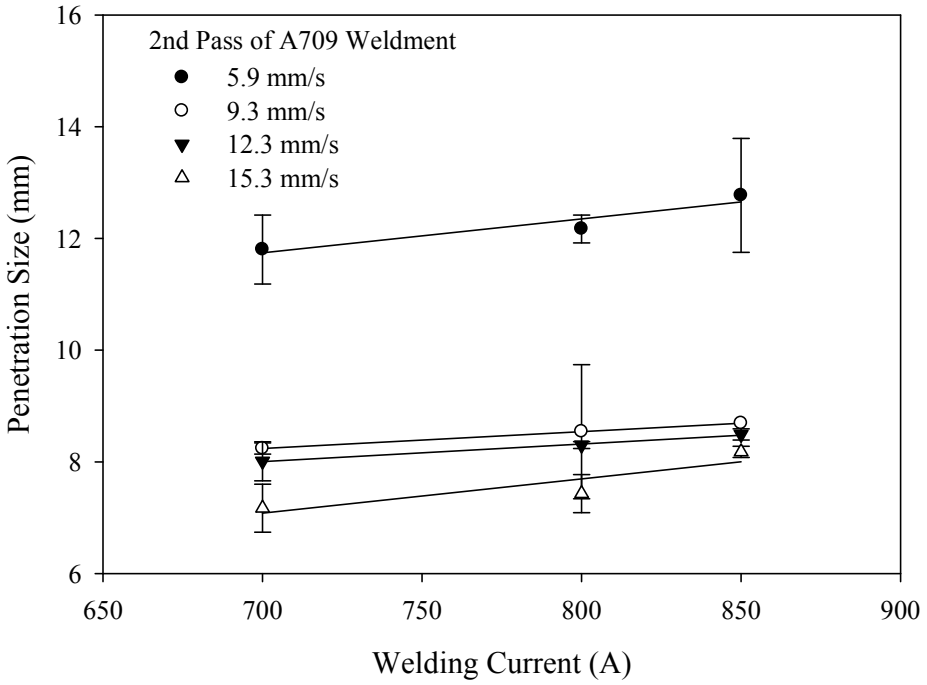

Figure 4.9. Effect of welding current on the penetration depth of A709 weldment.

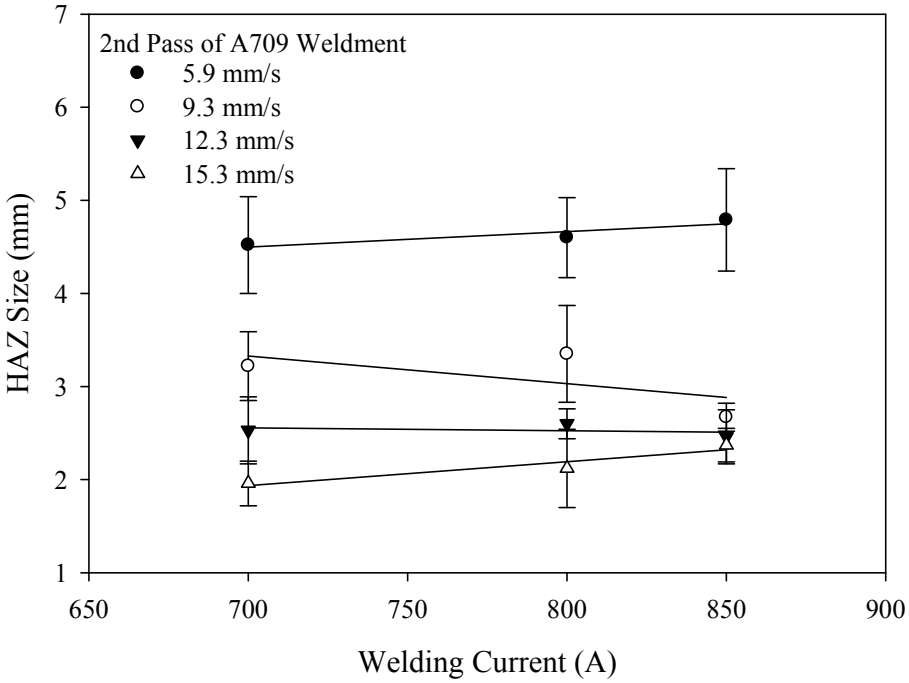

Figure 4.10. Effect of welding current on the HAZ size of A709 weldment.

size of SA516 and A709 weldments increase with increasing welding current. The contact angle of both materials decreases with welding current as shown in Figures 4.3 and 4.8. As for the weld bead width, Figures 4.2 and 4.7 show that welding current has very little effect on it. The observed changes are due to the heat input varying with the welding current. For a given travel speed and arc voltage, the heat input of SAW process increases with increasing welding current as shown in equation (2.2). In general, when heat input increases, there is a corresponding increase in both plate and electrode melting. Plate melting is related to the penetration depth and HAZ size, while the weld bead shape is related to electrode melting [36].

A large amount of heat input resulted in a large molten pool which consequently remained liquid metal for a long time, causing large penetration depth and more heat to flow out to the plate, while promoting a large HAZ size. This is why penetration depth and HAZ size increase with welding current. At the same time, electrode melting is accompanied with a change in weld shape, that is, any increase in heat input results in an increase in deposition rate or deposition area. Therefore, the deposition area will increase with increasing welding current. Reinforcement can be calculated using the following equation (Appendix B2 shows the derivation):

$$R = \frac{b \times \tan(180 - \theta)}{2} = \frac{2A_d}{b} \qquad 4.1$$

where A_d is deposition area, R is the height of reinforcement, b is the weld bead width and θ is the contact angle as shown in Figure 2.12.

According to the equation (2.2), heat input will increase with increasing welding current. The amount of deposited metal is directly related to heat input. If large heat input is used in the welding process, more electrodes will be melted. Therefore, the deposition area A_d increases with increasing welding current. Figures 4.2 and 4.7 show that welding current has very little effect on weld bead width b. According to equation (4.1), the height of reinforcement increases with increasing deposition area A_d . Since the deposition area A_d

increases with increasing welding current, therefore the height of reinforcement will increase with increasing welding current. Equation (4.1) also shows the $\tan(180-\theta)$ is proportional to the reinforcement. So, $\tan(180-\theta)$ increases with increasing welding current too. Therefore, contact angle θ will decrease with increasing welding current. Severe undercuts were found in weldments prepared using travel speeds 12.3 mm/s and 15.3 mm/s. As such, the bead widths of these weldments are very small.

4.1.2 Effect of Travel Speed

Figures 4.11 to 4.15 show the effect of travel speed on reinforcement, bead width, penetration depth, contact angle and HAZ size for SA516 weldments. The relationships between travel speed and these geometrical parameters for A709 weldments are shown in Figures 4.16 to 4.20.

It can be seen from Figures 4.11 and 4.16 that the reinforcement decreases with increasing travel speed for both materials. The bead width also decreases with increasing travel speed for both material as shown in Figures 4.12 and 4.17. This behaviour is attributed to the fact that heat input decreases with increasing travel speed in accordance with the eqution (2.2). For instance, the heat input of the weldment produced using a welding current of 700 A and a travel speed of 5.9 mm/s is about three times bigger than that produced using a welding current of 700 A and a travel speed of 15.3 mm/s. Generally, the electrode melting rate decreases with decreasing heat input. The deposition area (i.e., weld area above the weld surface) is proportional to the electrode melting rate. Therefore, the deposition area will decrease with increasing travel speed. Both reinforcement and bead width are proportional to the deposition area from geometrical viewpoint. Therefore, both reinforcement and bead width decrease with the travel speed.

Figures 4.13 and 4.18 show that the penetration size for both materials decreases with increasing travel speed. Similar results are obtained for HAZ size as shown in Figures 4.15 and 4.20. As mentioned previously, both penetration size and HAZ size depend on

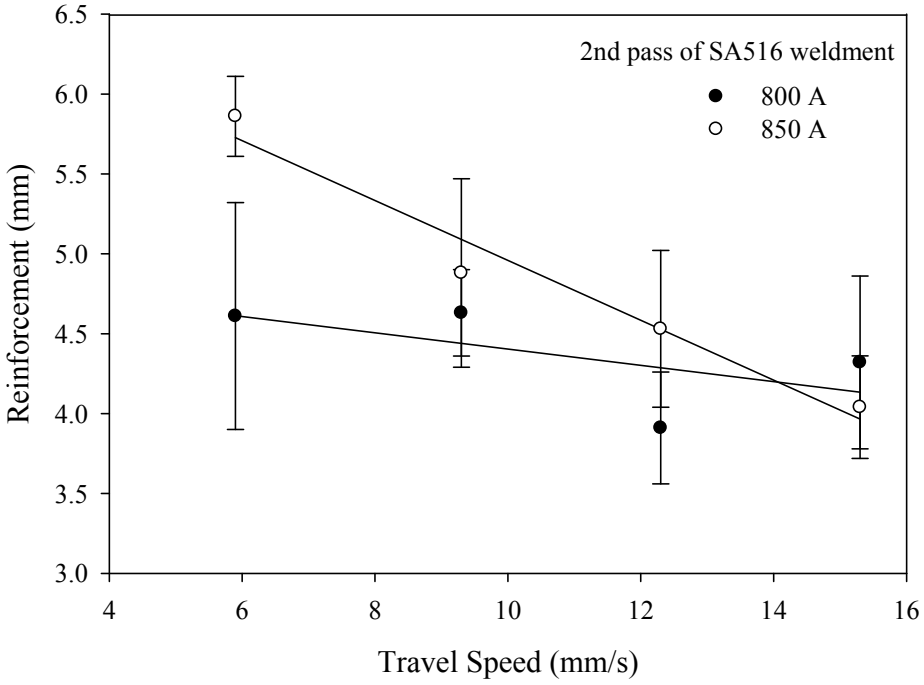

Figure 4.11. Effect of travel speed on the reinforcement of SA516 weldment.

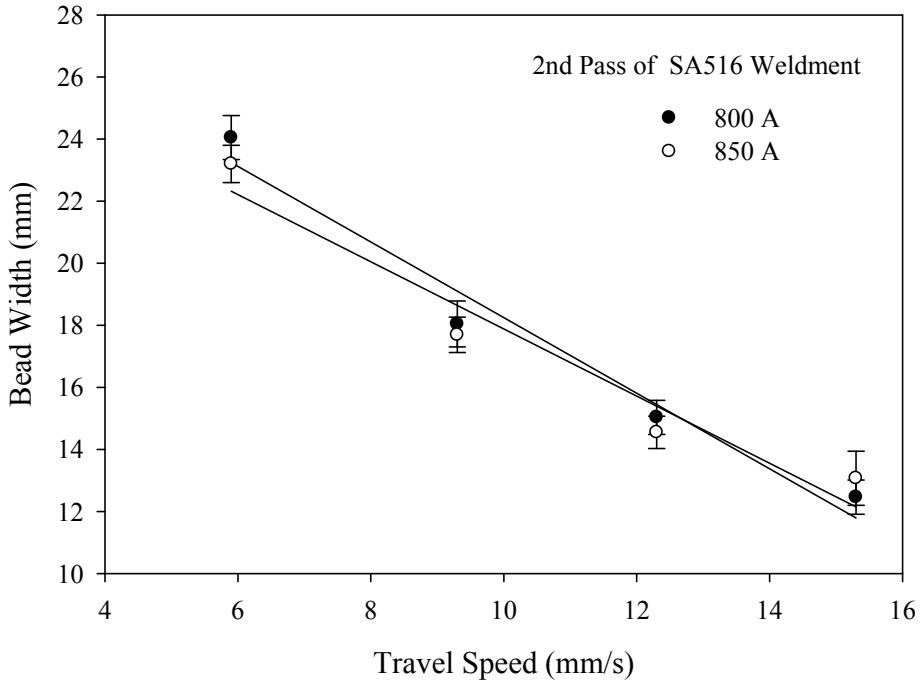

Figure 4.12. Effect of travel speed on the bead width of SA516 weldment.

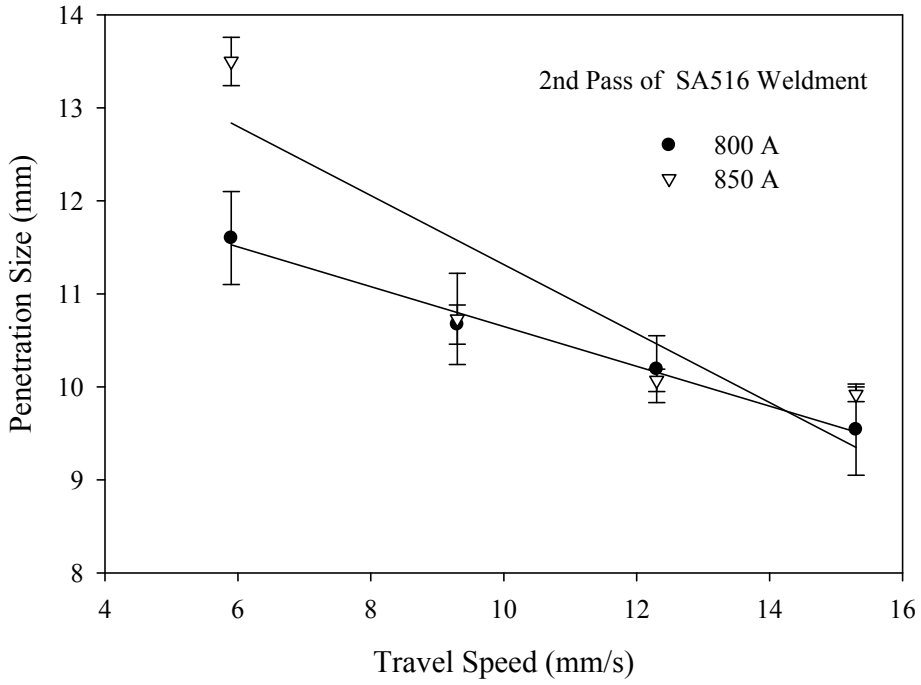

Figure 4.13. Effect of travel speed on the penetration depth of SA516 weldment.

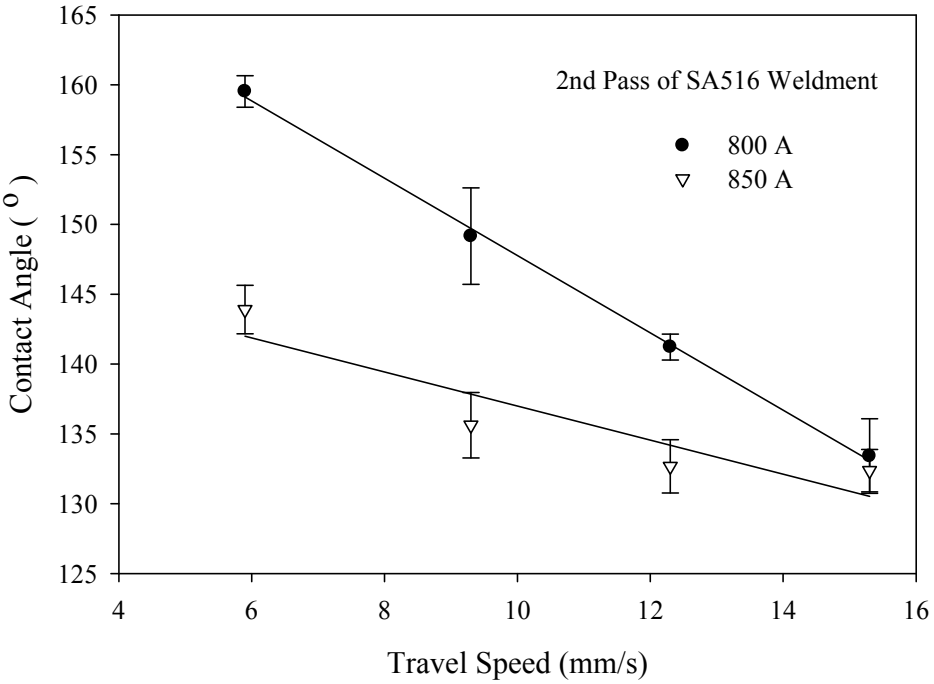

Figure 4.14. Effect of travel speed on the contact angle of SA516 weldment.

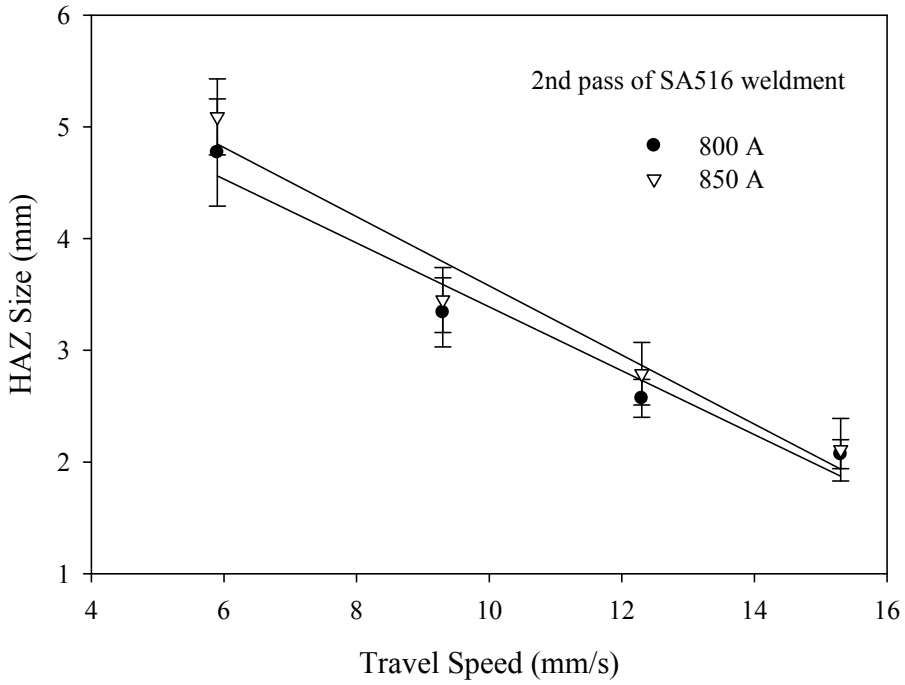

Figure 4.15. Effect of travel speed on the HAZ size of SA516 weldment.

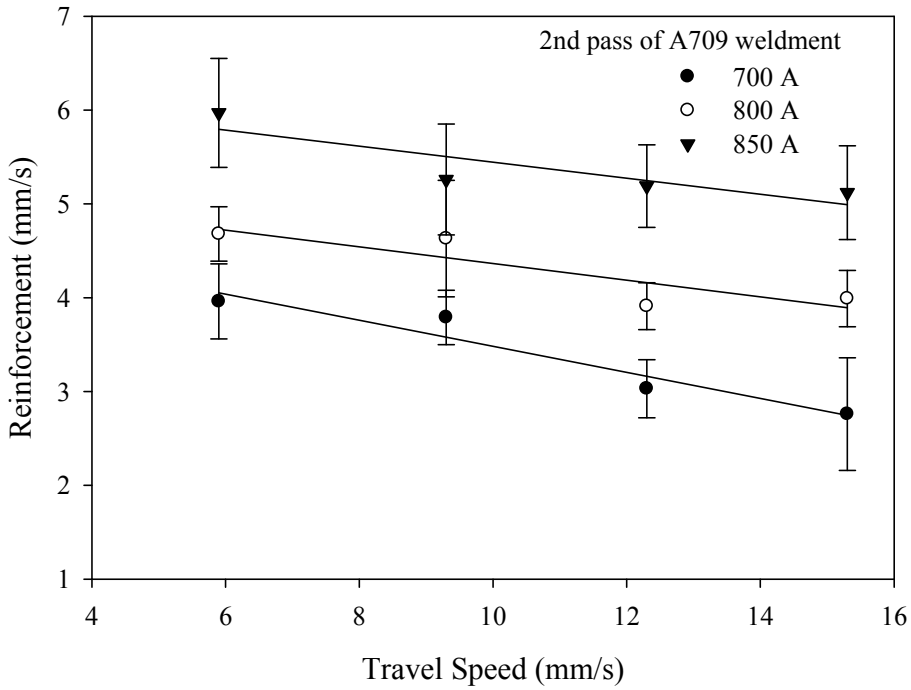

Figure 4.16. Effect of travel speed on the reinforcement of A709 weldment.

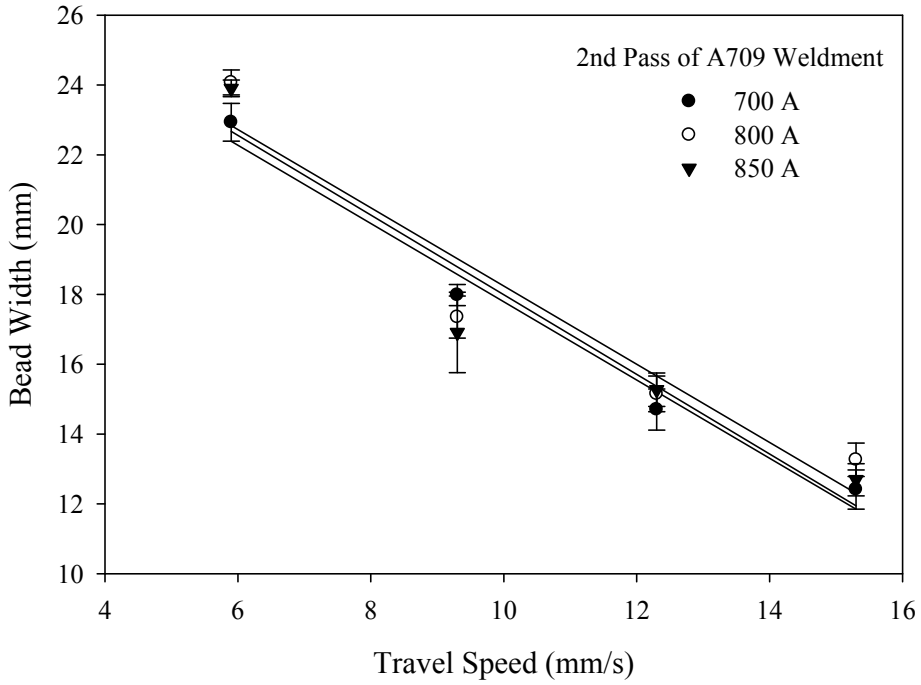

Figure 4.17. Effect of travel speed on the bead width of A709 weldment.

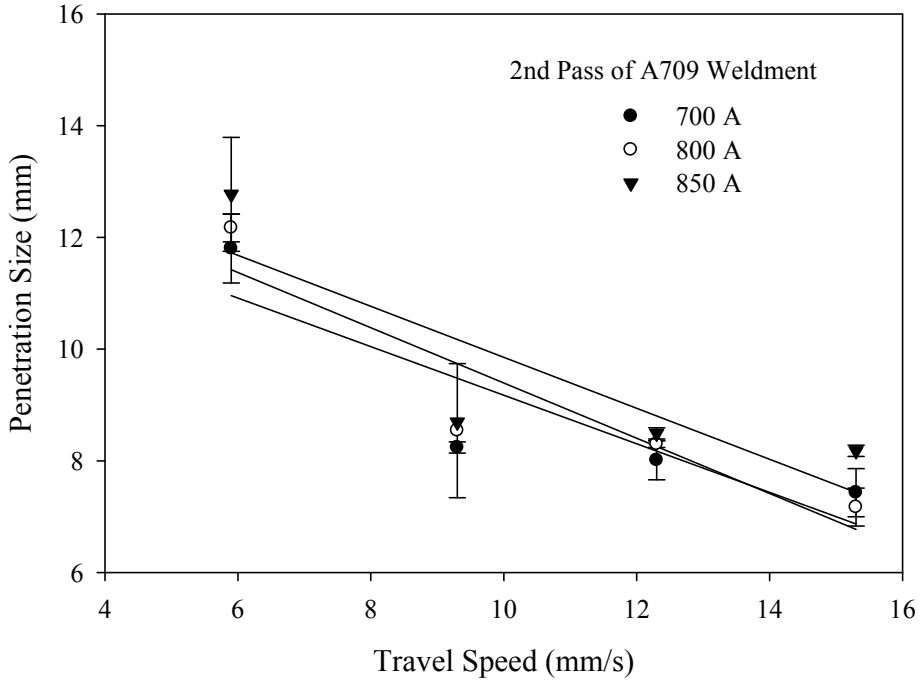

Figure 4.18. Effect of travel speed on the penetration depth of A709 weldment.

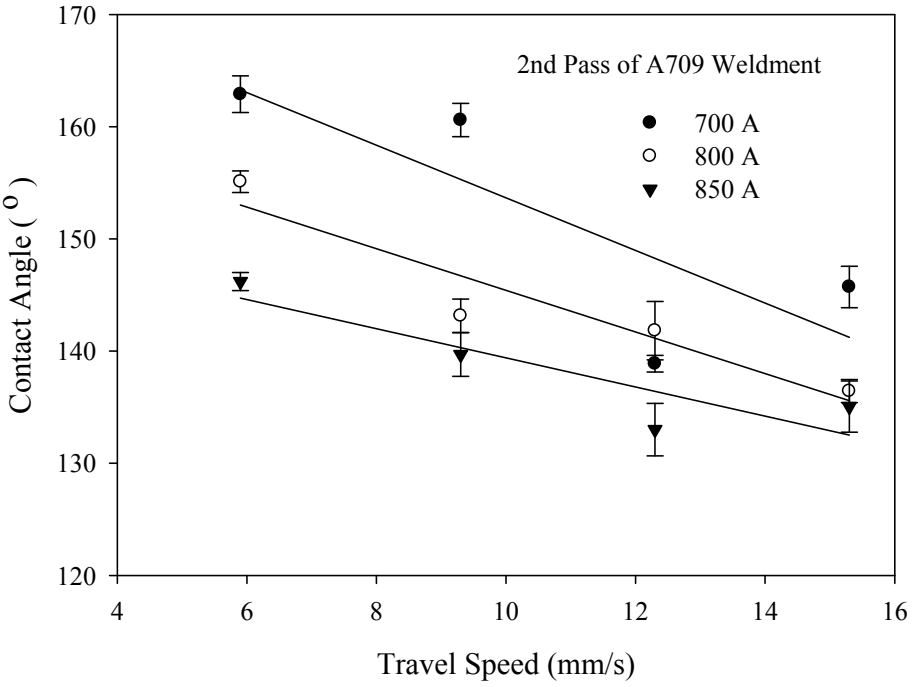

Figure 4.19. Effect of travel speed on the contact angle of A709 weldment.

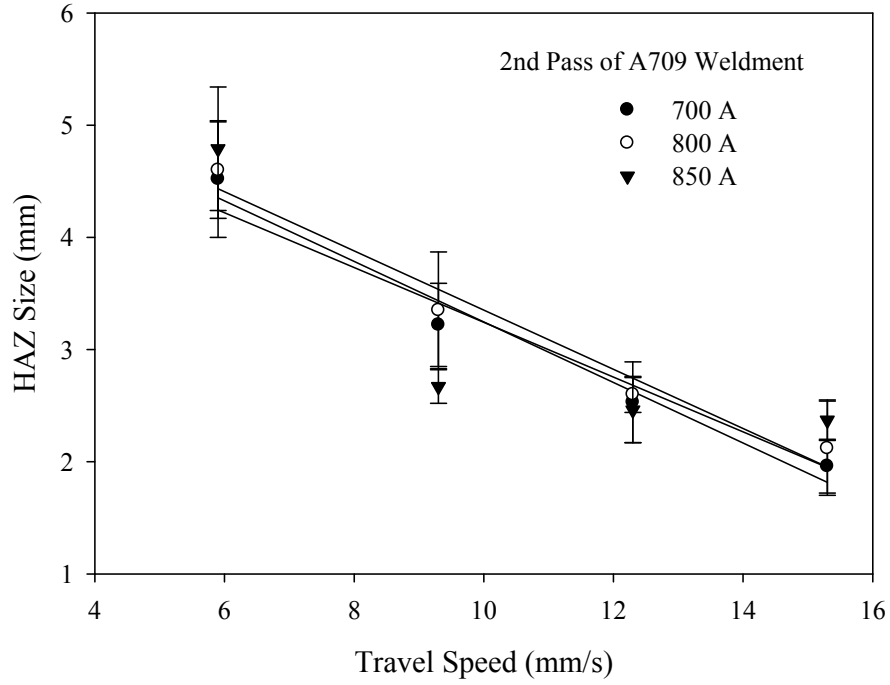

Figure 4.20. Effect of travel speed on the HAZ size of A709 weldment.

heat input. Therefore, penetration size and HAZ size decrease with increasing travel speed which resulted in decreased heat input. Figures 4.14 and 4.19 show that contact angle also decreases with increasing travel speed. The reason for this behaviour is that the cooling rate of the weld metal increases with increasing travel speed. Thus, the metal solidification rate of the weld metal will increase with increasing travel speed. With the combination of flux resistance during the welding process, the weld bead shape will become steeper as travel speed increases. Therefore, the contact angle of the weld bead decreases with increasing travel speed.

4.2 Submerged Arc Welding Defects

The welding standard used for SA516 weldments was the American Society of Mechanical Engineers (ASME) boiler and pressure vessel code, Subsection VIII, Division 1 [63]. The welding code used for A709 weldments was the American Welding Society (AWS) structural welding code – steel standard [64]. The relationship between weld defects and SAW process parameters was investigated to find the appropriate welding variables for obtaining good quality weldments which meet the requirements of the ASME or the AWS standard. Parts of the acceptance criteria pertinent to this project are listed below. The defects investigated mainly included undercuts and lack of penetration.

(a) "Butt welded joints shall have complete penetration and full fusion" [63];

(b) "The reduction in thickness shall not exceed 1 mm or 10% of the nominal thickness of adjoining surface, whichever is less" [63].

4.2.1 Surface Defects – Undercuts

Figure 4.21 shows typical undercuts that developed in SA516 and A709 weldments. The undercut in Figure 4.21(a) occurred in a SA516 weldment produced using 850 A and 15.3

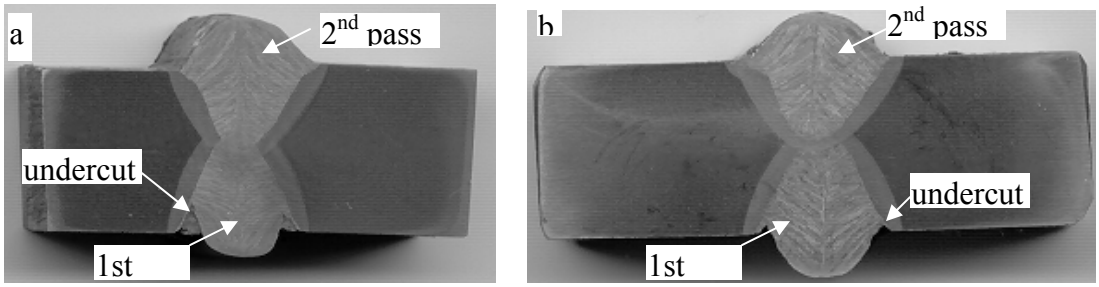

Figure 4.21. Undercuts developed in (a) SA516 weldment using 850A and 15.3 mm/s; (b) A709 weldment using 800A and 15.3 mm/s.

mm/s, while Figure 4.21(b) shows a typical undercut produced in A709 weldment using 800 A and 15.3 mm/s. As can be seen, the second pass of each sample generated no undercuts. Undercuts do not only impair the weld appearance, they impair weld strength, particularly when the weld is loaded in tension or subjected to fatigue.

Tables 4.1 and 4.2 show the average values of undercut depth and undercut ratio obtained during the first and second pass welds of SA516 and A709 weldments, respectively. Undercut ratio is defined as the total length of undercut in one weldment divided by the length of the weldment in this project. Although the undercut depth is mentioned as the acceptance criteria from the ASME standard, the undercut ratio can also show how severe the surface defects are in the whole weldment using specific welding parameters. Table 4.1 shows that undercuts were found in both passes of the weldments of PV-7, PV-8, PV-11, PV-12. Both the undercut depth and undercut ratio of the first pass are generally more severe than those of the second pass. For the weldments produced using 850 A and 12.3 mm/s (PV11) and 15.3 mm/s (PV12), the undercut ratios of the first pass for both weldments are greater than 80%. However, the undercut ratios of the second pass for both weldments are less than 3%. All the weldments produced with low welding current (700 A) have no undercuts. All the weldments produced with low speeds (5.9 mm/s and 9.3 mm/s) and high welding currents (800 A and 850 A) have no undercuts.

Table 4.2 shows similar results for A709 weldments. Severe undercuts were found in the first pass for weldments produced using 800 A and 15.3 mm/s (WT8), and using 850 A and 12.3 mm/s (WT11). Almost all weldments of WT7, WT8, WT11 and WT12 have

Table 4.1. Average values of undercut depth and undercut ratio for SA516 weldments.

Weld No.	First Pass		Second Pass	
	Undercut Depth (mm)	Undercut Ratio (%)	Undercut Depth (mm)	Undercut Ratio (%)
PV7	0.83 ± 0.17	16.67	0.75 ± 0.11	2.78
PV8	0.97 ± 0.11	44.44	0.99 ± 0.08	6.94
PV11	1.32 ± 0.3	83.33	1.23 ± 0.2	0.41
PV12	1.33 ± 0.4	88.89	0.79± 0.08	2.78
Others	0	0	0	0

Table 4.2. Average values of undercut depth and undercut ratio for A709 weldments.

Weld No.	First Pass		Second Pass	
	Undercut Depth (mm)	Undercut Ratio (%)	Undercut Depth (mm)	Undercut Ratio (%)
WT7	0.88 ± 0.12	33.33	0.79 ± 0.03	2.78
WT8	1.05 ± 0.34	100	1 ± 0.03	5.56
WT11	1.18 ± 0.4	83.33	0.97 ± 0.26	5.56
WT12	1.11 ± 0.34	11.11	0.98 ± 0.18	6.94
Others	0	0	0	0

undercuts on the first pass. The second pass of these weldments show a small undercut ratio. The weldments produced using low speeds and low welding current have no undercut at all. The reason why the undercut ratio of both passes is quite different is because of the different interpass /or preheat temperatures experienced by each side of the plate. Except the interpass temperature, the other SAW welding variables for the first

pass were the same as those of the second pass. Table 3.4 shows that the temperatures of the first pass ranged from 20 ^{o}C to 30 ^{o}C and the interpass temperature of the second pass was from 60 ^{o}C to 107 ^{o}C. Generally, the cooling rate of a weldment decreases with increasing preheat temperatures because the temperature gradient decrease with increasing preheat temperatures. Therefore, the cooling rate of the second pass was less than that of the first pass. The solidification time of molten weld metal during the second pass was longer than that of the first pass. Thus, the molten metal in the deposition area had longer time to flow to the weld toe to overcome the surface tension and eliminate undercuts. As a result of this, the undercut ratio of the second pass was less than that of the first pass. In order to get a sound weld profile, a possible way to solve the undercut problem is using high preheat temperatures.

According to the ASME acceptance criteria, the acceptable undercut depth for both materials is less than 1mm since the thickness of the plate used in this project is 17 mm. Although the average undercut depth of PV7 and WT7 was a less than 1mm, the maximum undercut depth of these weldments was more than 1mm. Therefore, all weldments listed in Tables 4.1 and 4.2 are not acceptable.

4.2.1.1 Effect of Welding Current on Undercuts

Figures 4.22 and 4.23 show respectively the effect of welding current on undercut ratio and undercut depth of SA516 weldments obtained in the first pass. Similar results obtained for A709 are shown in Figures 4.24 and 4.25, respectively. All these figures indicate that no undercut occurred in the weldments using the travel speeds of 5.9 mm/s and 9.3 mm/s. Figures 4.22 and 4.23 show that undercut ratio and undercut depth increase with increasing welding current when the travel speeds are more than 9.3 mm/s. Similar results are shown in Figures 4.24 and 4.25 for A709 weldments, except for the plot at 15.3 mm/s in Figure 4.24.

As discussed in section 4.1.1, increasing welding current will increase heat input and deposition rate during the SAW process. Thus, the reinforcement of the weldment will

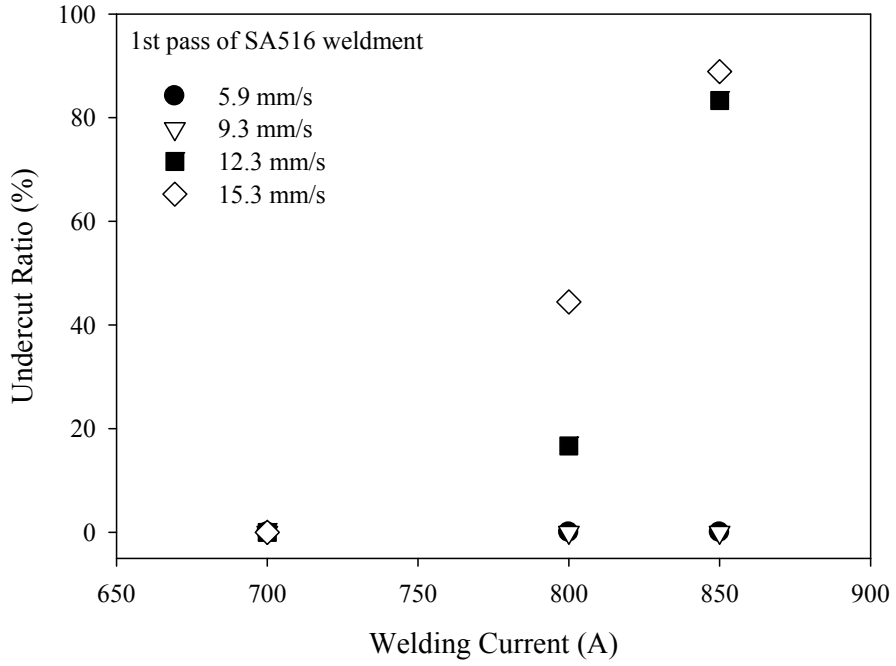

Figure 4.22. Effect of welding current on the undercut ratio of SA516 weldment.

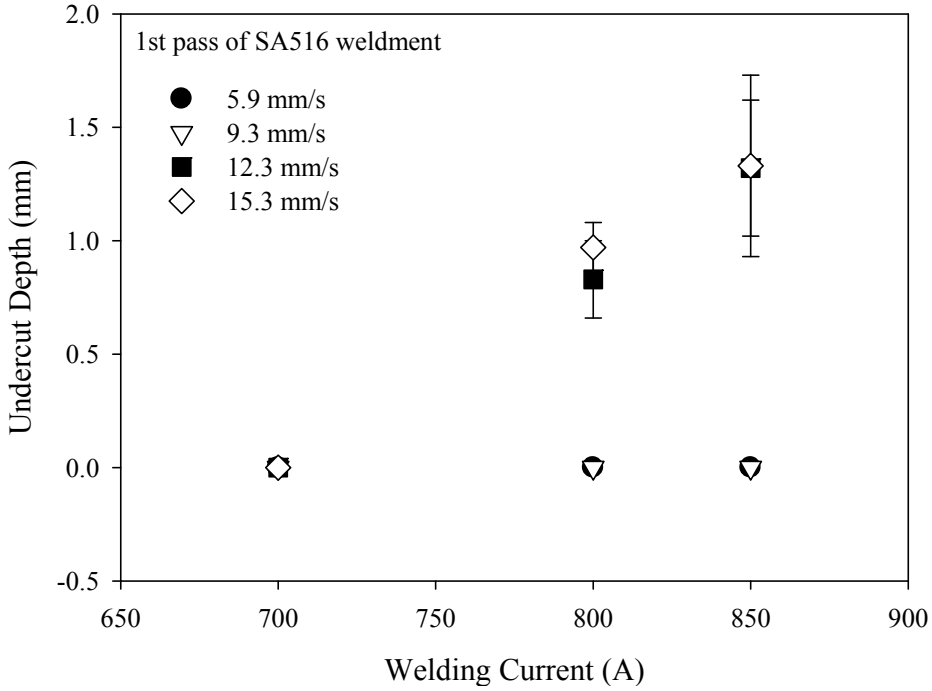

Figure 4.23. Effect of the welding current on the undercut depth of SA516 weldment.

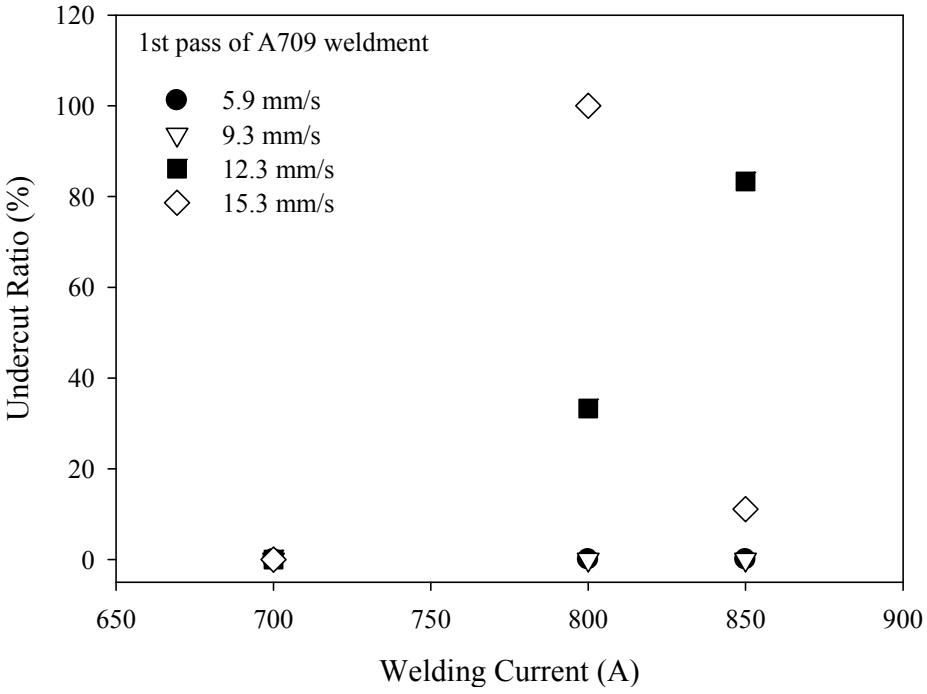

Figure 4.24. Effect of welding current on the undercut ratio of A709 weldment.

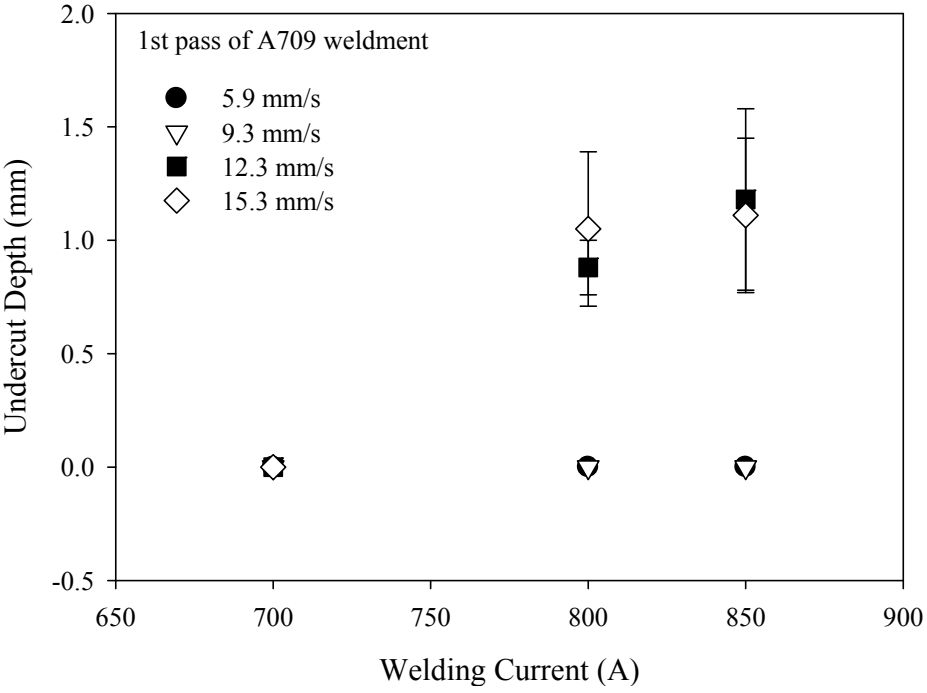

Figure 4.25. Effect of welding current on the undercut depth of A709 weldment.

increase with increasing deposition rate. Consequently, the magnitude of the contact angle will change as the reinforcement height increases. Figures 4.3 and 4.8 show that contact angle decreases with welding current. Small contact angle means the weld bead profile will be steep. The surface tension of the molten metal will increase along the perpendicular direction of weld travel direction when the weld bead is very peaked [19]. Therefore, the molten metal can be drawn from the edge to the center of weld bead when welding current is large. Undercuts will occurr after the molten metal solidifies. The reason for the different behaviour of the A709 weldment produced using 15.3 mm/s and 850 A is that the preheat temperature of this weldment was 60 ^{o}C, while the others were produced at room temperature. As cooling rate will decrease with increasing preheat temperature, high preheat temperature helps to eliminate undercuts in the weldments.

The effect of travel speed on undercut size and undercut ratio was also investigated. Figures 4.26 and 4.27 show the effect of travel speed on undercut ratio and undercut depth of SA516 weldments, respectively. Similar results for A709 weldments are shown in Figures 4.28 and 4.29. It can be seen from Figures 4.26 and 4.27 that no undercut occurred when the welding current was 700 A. The undercut ratio and undercut depth increase with increasing travel speed. Figures 4.28 and 4.29 show a similar trend. These trends are due to the fact that high travel speed results in low heat input and deposition rate. When the travel speed is high, the weld bead width will be small. Therefore, the weld bead shape will be highly peaked because of its extremely fast solidification rate. The surface tension of the molten weld metal easily draws the molten metal from the edge to the center and results in undercuts. The results presented in Figures 4.14 and 4.19 show that contact angle decreases with increasing travel speed. Alhough the result of the first pass of A709 weldment obtained using a welding current of 850 A and a travel speed of 15.3 mm/s has a different behaviour, it did not change the trend because the preheat temperature of this weldment was quite different from others. High preheat temperatures result in low solidification rate and prevent undercuts from occurring during SAW process. Therefore, the possible methods to prevent undercut from occurring in order to get a sound weldment profile are: (i) using high preheat or interpass temperature, (ii) reducing welding travel speed, and (iii) reducing welding current.

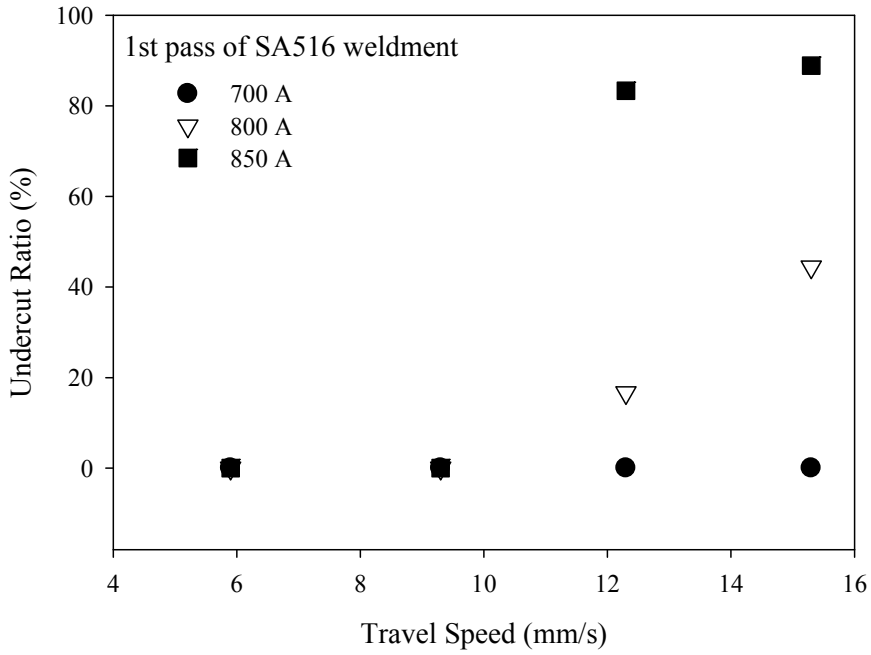

Figure 4.26. Effect of travel speed on the undercut ratio of SA516 weldment.

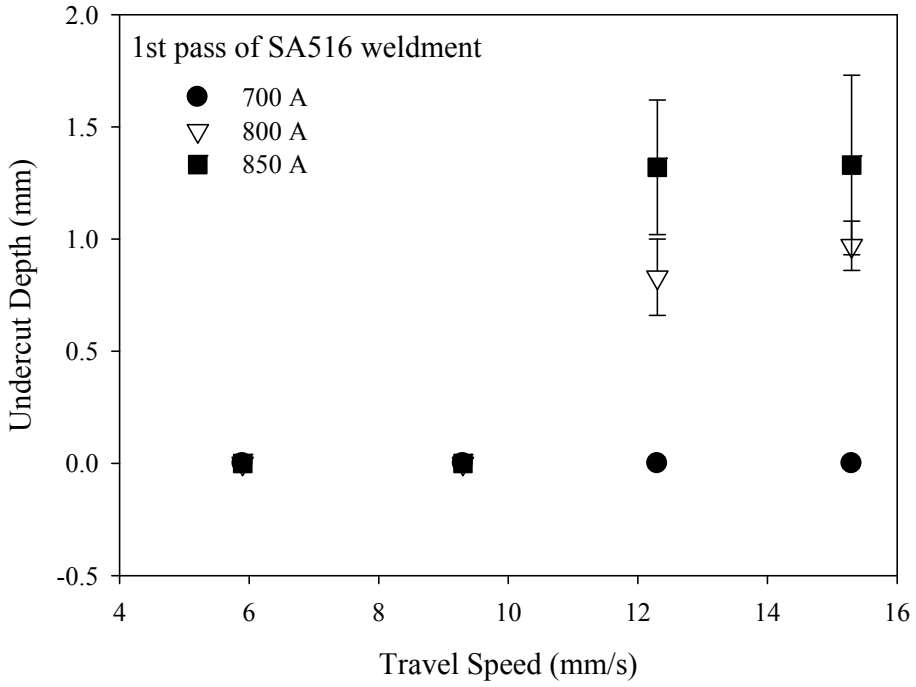

Figure 4.27. Effect of travel speed on the undercut depth of SA516 weldment.

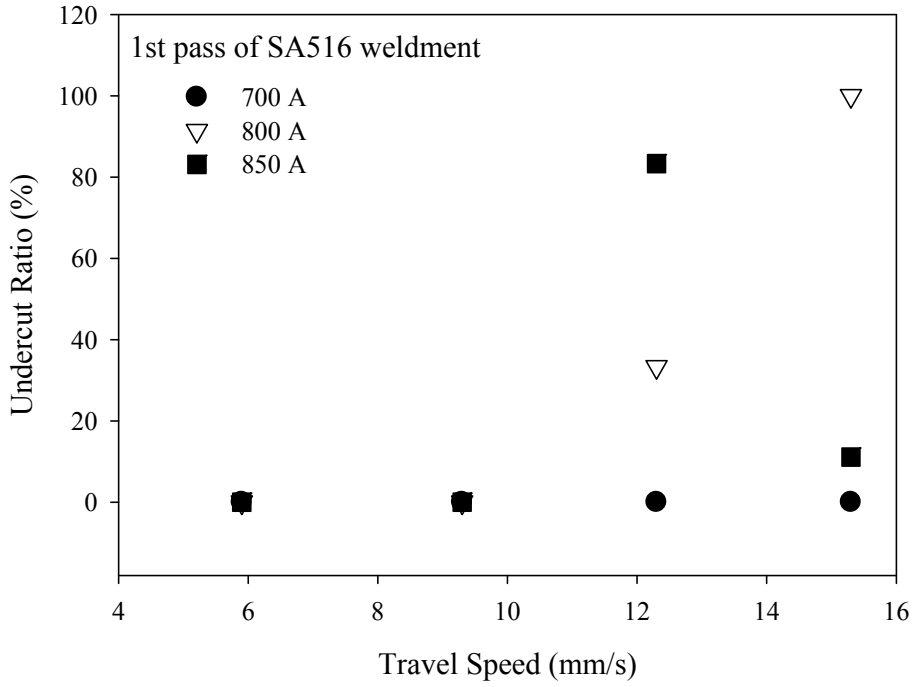

Figure 4.28. Effect of travel speed on the undercut ratio of A709 weldment.

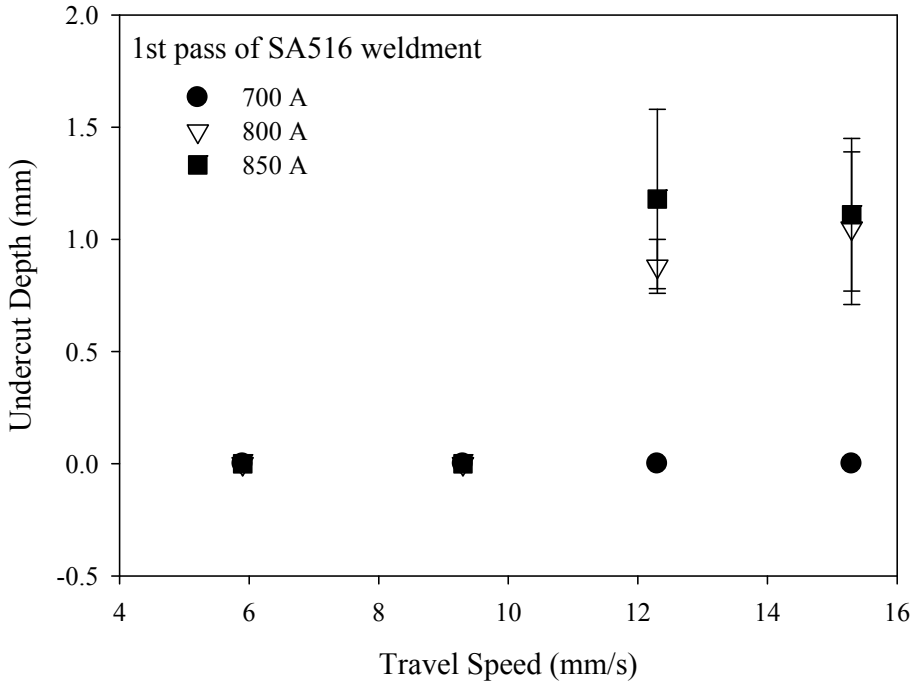

Figure 4.29. Effect of travel speed on the undercut depth of A709 weldment.

4.2.2 Internal Defects – Lack of Penetration

Lack of penetration (LOP) defect occurs when two opposing weld beads do not interpenetrate. LOP defects are serious defects because they can seriously reduce the strength, toughness and fatigue life of weldments since the weld cross sectional area is significantly decreased [35]. Figure 4.30 shows defect reflectors that produced a response greater than 20% of the distance amplitude correction (DAC) curve for different weldments using a 70^{o} angle transducer. Here, 20% DAC corresponds to an increase of 12 dB on the reference DAC curve. All defect reflectors that produced a response equal or greater than 20% of the DAC curve were recorded in accordance with ASME Boiler and Pressure Vessel Code, Section V, Article 4 version 2004 [58]. Figure 4.31 shows typical LOP defects found in SA516 and A709 weldments.

Tables 4.3 and 4.4 show the average LOP depth and LOP ratio obtained for SA516 and A709 weldments that have LOP defects, respectively. LOP ratio is defined as total length of LOP in one weldment over the whole length of the weldment in this project. Although LOP can not be accepted by the ASME standard, the LOP ratio can show how severe the internal defects are in the weldments using specific welding paramenters. Table 4.3 shows that only the weldments produced using welding current 800 A and 15.3 mm/s had LOP. Table 4.4 shows that the weldments produced using a low welding current (700 A) and high travel speed (12.3 mm/s and 15.3 mm/s) have LOP defects. The weldments produced using 800 A and 15.3 mm/s also suffered LOP. All the other weldments in this project did not suffer LOP defect.

The occurrence of LOP defect in the weldments is due to low heat input during the SAW process because heat input is related to electrode and plate melting. If the plate melting energy is too low to melt the parent metal to fuse the weld metal during the first pass, serious defects occur leading to LOP. The results of geometry measurements from Figures 4.13 and 4.18 show that penetration depth decreased with increasing travel speed, while it increased with welding current as shown in Figures 4.4 and 4.9. The thickness of the weldment is 17 mm. So, the minimum penetration depth of the weldment is 8.5 mm if

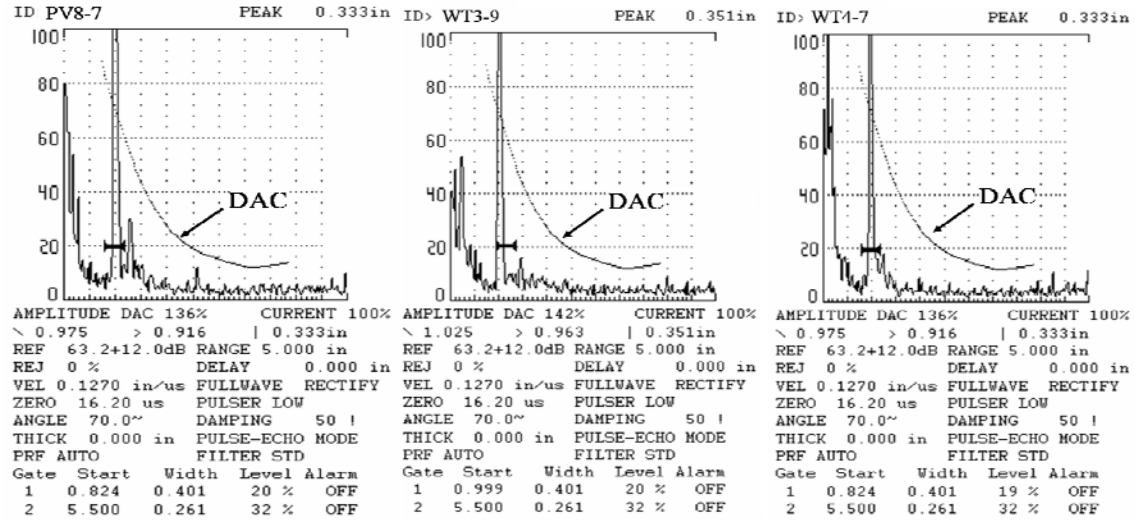

Figure 4.30. Typical LOP defect reflectors that produce responsesd greater than 20% DAC curve.

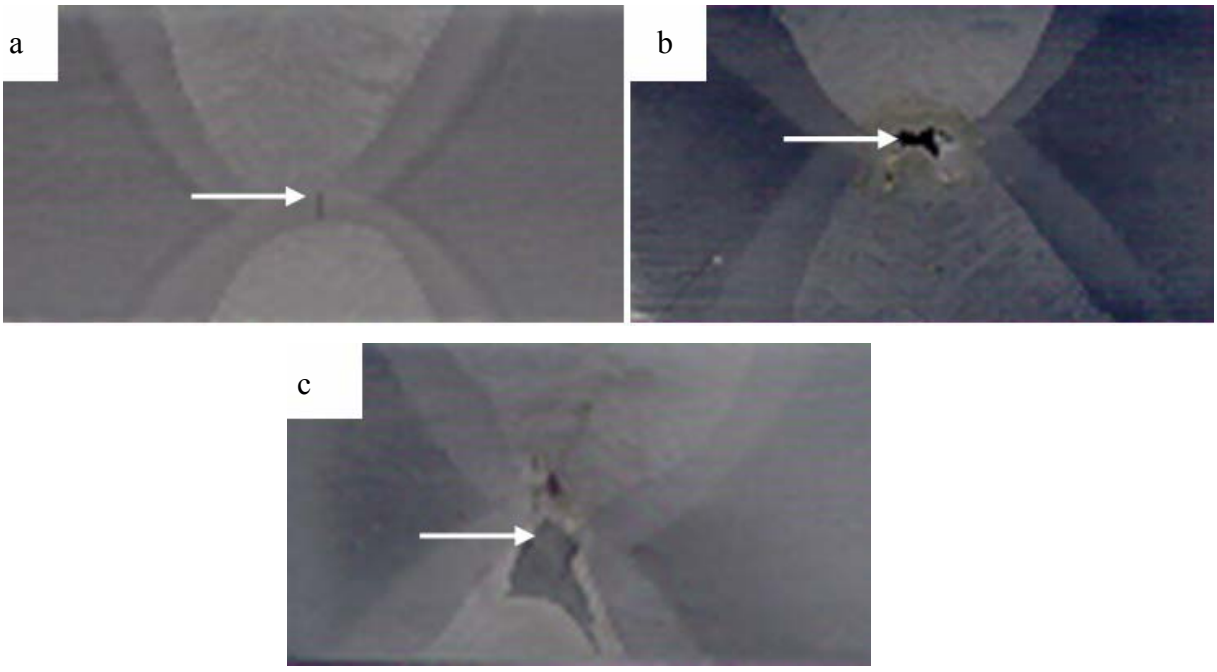

Figure 4.31. Examples of lack of penetration defect: (a) SA516 weldment produced using 800 A and 15.3 mm/s; (b) A709 weldment produced using 700 A and 12.3 mm/s and (c) A709 weldment produced using 700 A and 15.3 mm/s.

Table 4.3. Average LOP depth and LOP ratio obtained for SA516 weldment.

Weld No.	Welding Current (A)	Travel Speed (mm/s)	Heat Input (kJ/mm)	LOP Depth (mm)	LOP Ratio (%)
PV8	800	15.3	1.83	2.3 ± 0.5	67.7

Table 4.4. Average LOP depth and ratio for A709 weldments.

Weld No.	Welding Current (A)	Travel Speed (mm/s)	Heat Input (kJ/mm)	LOP Depth (mm)	LOP Ratio (%)
WT3	700	12.3	1.99	2.46 ± 0.5	66.67
WT4	700	15.3	1.60	3.56 ± 0.8	100
WT8	800	15.3	1.83	2.4 ± 0.4	8.33

it has full penetration. However the penetration depths of weldments produced using 700 A and 12.3 mm/s and 15.3 mm/s are less than 8 mm as shown in Figure 4.18. Thus, the ultrasonic test results are consistent with the results obtained from geometry measurements for penetration depth. According to the acceptance criteria listed in section 4.2, the combinations of SAW parameters listed in Tables 4.3 and 4.4 do not meet the criteria because no LOP is permitted in the butt weld.

4.3 Melting Efficiency

The deposition and total fusion areas were measured using the IMAQ Vision Builder 5.0 software. The EME, PME and WPME were calculated using equations 2.5, 2.6 and 2.7. Since the fusion zone of the first pass overlaps that of the second pass, reasonably accurate values of deposition area and total fusion area can be obtained from the second pass of the weldments. Welding parameters and their corresponding EME, PME and WPME values for SA516 and A709 weldments are given in Tables 4.5 and 4.6,

Table 4.5. Effect of SAW parameters on the melting efficiency of SA516 weldments.

Weld No.	Current (A)	Speed (mm/s)	Heat Input (kJ/mm)	EME (%)	PME (%)	WPME (%)
PV1	700	5.9	4.15	18.81 ± 0.41	42.47 ± 3.42	61.29 ± 3.51
PV5	800	5.9	4.75	23.05 ± 0.74	49.1 ± 2.03	72.15 ± 1.29
PV6	800	9.3	3.01	27.85 ± 1.07	47.56 ± 0.56	75.41 ± 1.4
PV7	800	12.3	2.28	33.26 ± 2.19	47.05± 2.73	80.31 ± 4.56
PV8	800	15.3	1.83	26.71 ± 7.26	46.1 ± 3.08	72.81 ± 7.4
PV9	850	5.9	5.04	28.5 ± 1.76	47.53 ± 2.89	76.03 ± 1.21
PV10	850	9.3	3.20	28.84 ± 2.28	47.42 ± 0.25	76.27 ± 2.17
PV11	850	12.3	2.42	32.12 ± 4.02	44.73 ± 3.56	76.84 ± 6.94
PV12	850	15.3	1.94	32.67 ± 2.71	45.74 ± 0.55	78.41 ± 2.28

respectively. These data were used to establish the relationships between process variables and EME, PME and WPME. From the results shown in Tables 4.5 and 4.6, the following are deduced: (i) the electrode melting efficiency of SAW for both steels varies between 18% and 41%; (ii) the plate melting efficiency varies between 32% and 54%; and (iii) the whole process melting efficiency varies between 62% and 88%, depending on the combination of the SAW process variables. The EME and PME obtained in the present investigation are a little higher than those reported by Chandel [57]. The reason for this behaviour is because the welding parameters used in this study focused on welding current and travel speed, while the welding parameters used in Chandel's study are focused on arc voltage, electrode extension, electrode diameter and electrode polarity.

Table 4.6. Effect of SAW parameters on the melting efficiency of A709 weldments.

Weld No.	Current (A)	Speed (mm/s)	Heat Input (kJ/mm)	EME (%)	PME (%)	WPME (%)
WT1	700	5.9	4.15	21.72 ± 0.3	47.64 ± 2.37	69.36 ± 2.55
WT2	700	9.3	2.63	27.9 ± 1.56	45.87 ± 1.63	73.77± 0.17
WT3	700	12.3	1.99	31.11 ± 1.2	45.52 ± 3.14	76.63 ± 4.28
WT4	700	15.3	1.60	22.12 ± 0.57	53.39 ± 3.92	75.51 ± 3.41
WT5	800	5.9	4.75	31.99 ± 3.88	47.15 ± 3.18	79.14 ± 1.06
WT6	800	9.3	3.01	41.12 ± 7.32	47.51 ± 6.15	88.63 ± 9.63
WT7	800	12.3	2.28	28.34 ± 1.17	44.97 ± 2.47	73.32 ± 3.01
WT8	800	15.3	1.83	34.02 ± 1.92	45.19 ± 0.64	79.20 ± 1.31
WT9	850	5.9	5.04	31.53 ± 0.44	48.29 ± 2.42	79.82 ± 2.0
WT10	850	9.3	3.20	30.74 ± 2.14	36.33 ± 3.93	67.07 ± 3.17
WT11	850	12.3	2.42	32.87 ± 2.75	40.86 ± 2.75	73.73 ± 3.89
WT12	850	15.3	1.94	33.44 ± 1.29	47.72 ± 1.73	81.16 ± 2.75

4.3.1 Effect of Welding Current on Melting Efficiency

Figure 4.32 shows the effect of welding current on EME, PME and WPME of SA516 weldments produced using a travel speed of 5.9 mm/s. Similar results for A709 produced using 5.9 mm/s and 15.3 mm/s are shown in Figures 4.33 and 4.34, respectively. Figure 4.32 shows that there is an increase in EME, PME and WPME of SA516 weldments as welding current increased. For the given welding parameters, the EME is lower than PME. The WPME is the highest because it is equal to the sum of EME and PME, i.e., WPME = EME + PME. Figures 4.33 and 4.34 show similar results as in Figure 4.32

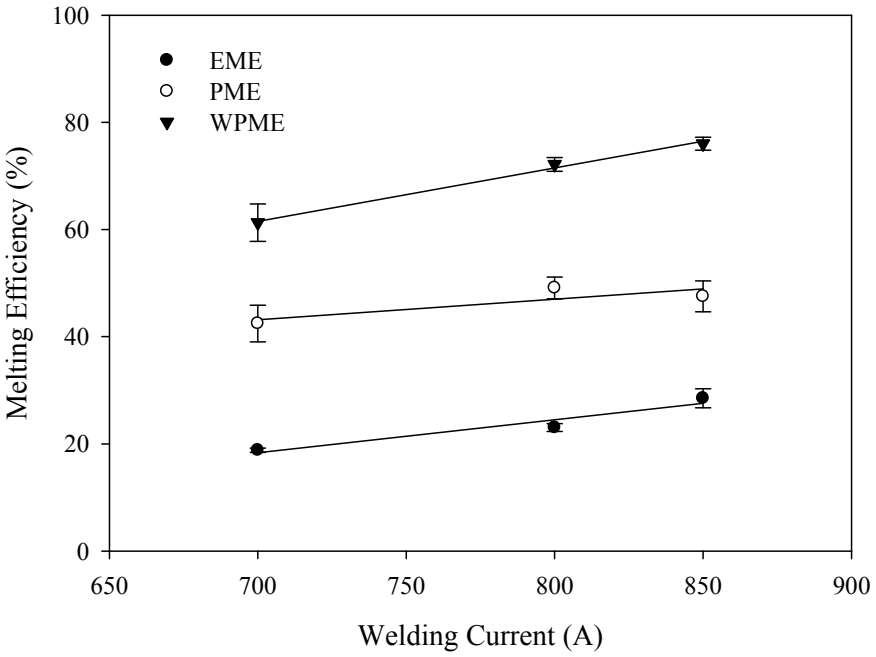

Figure 4.32. Effect of welding current on the melting efficiency of SA516 weldment produced using 5.9 mm/s.

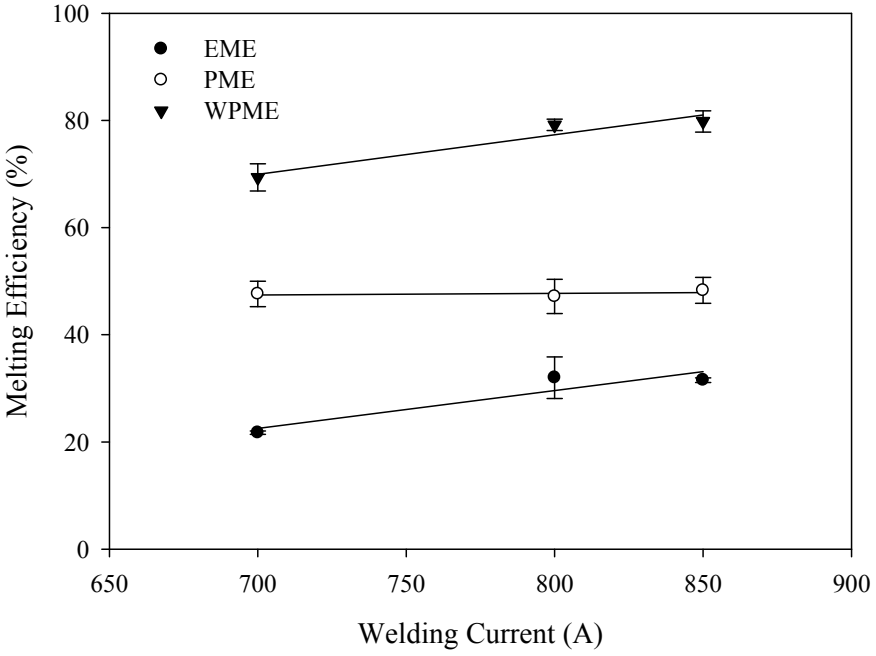

Figure 4.33. Effect of welding current on the melting efficiency of A709 weldment produced using 5.9 mm/s.

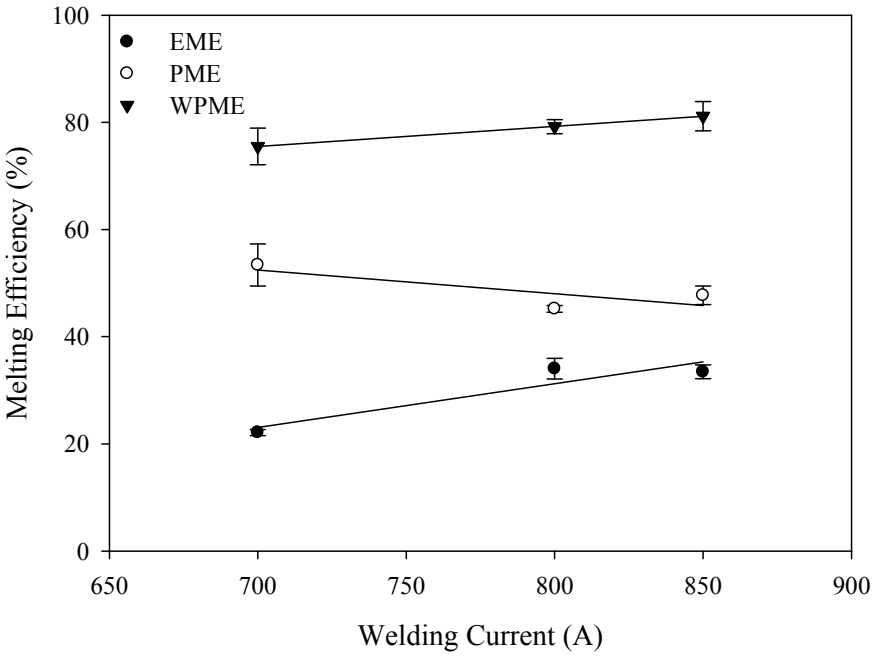

Figure 4.34. Effect of welding current on the melting efficiency of A709 at 15.3 mm/s.

except that PME decreases with increasing welding current for a travel speed of 15.3 mm/s. Since heat input increases with increasing welding current according to the equation (2.2), the deposition rate of the electrode increases with increasing heat input.

The deposition area of the weldment for a given electrode material, electrode diameter and voltage will increase with increasing welding current. The welding plasma could have a high temperature columnar shape and some of its heat will be transferred to the parent metal. The higher the heat generated in the arc column, the greater the plate melting. The molten metal droplets from the electrode are superheated as they pass through the arc column. This superheat will be added to the parent metal when the droplets come in contact with it. The results obtained in this work are consistent with the results reported by Chandel [57] who reported that the EME increased with increasing welding current. Figure 4.34 shows PME decreases with increasing welding current. As mentioned in section 4.2.1, several undercuts were found in the weldments produced using 15.3 mm/s. Therefore, the bead width of these weldments is very small because it

decreases with increasing undercut. Thus, the deposition area and plate fusion area will be affected by the undercuts.

4.3.2 Effect of Travel Speed on Melting Efficiency

Figures 4.35 and 4.36 show the effect of travel speed on EME, PME and WPME of SA516 weldments for welding currents of 800 A and 850 A, respectively. The relationship between melting efficiency and travel speed for A709 weldments is shown in Figures 4.37 to 4.39. Figures 4.35 and 4.36 show that EME and WPME increase slightly with increasing travel speed, while travel speed has little effect on PME. Similar results were obtained in Figures 4.37 and 4.38 for A709 weldments. Figure 4.39 shows EME and WPME decrease slightly with travel speed for A709 using weld current 800 A. In the present investigation, the heat input was changed by changing the travel speed and welding current. For a given welding current, the low heat input was obtained by increasing travel speed. The low heat input in SAW process means that a small molten pool remained liquid for a short time [37]. Therefore, the thermal gradient between the weld interface and fusion zone was steep in high travel speed. At the same time, most of the heat to melt flux comes from the deposited area during SAW process. As thermal gradient steepens with increasing travel speed, the volume of the melting the flux during the SAW process will decrease appreciably. Therefore, the heat released from flux will decrease and thus the total energy loss for the whole SAW process will decrease with increase in travel speed. As a result, the overall welding process melting efficiency will increase with increasing travel speed.

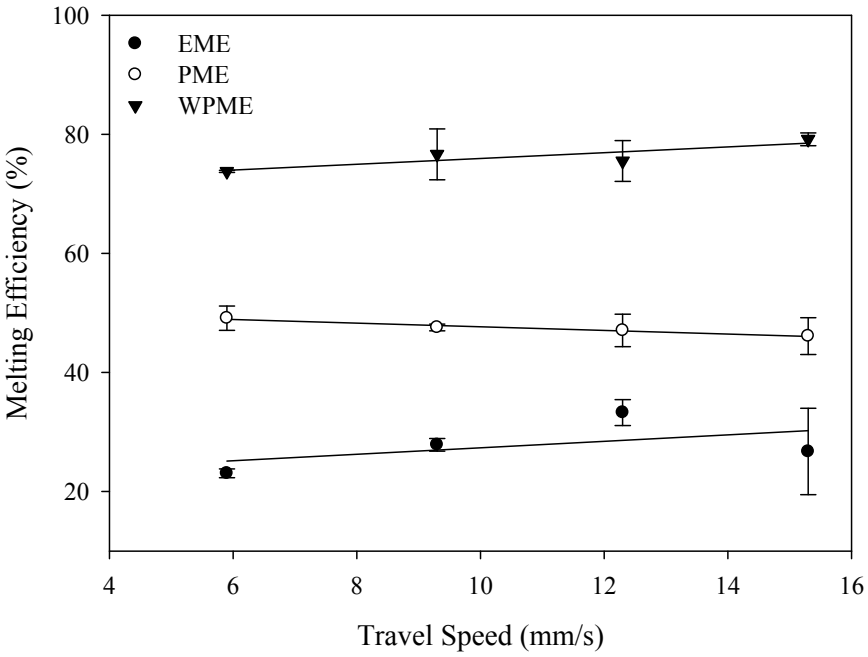

Figure 4.35. Effect of travel speed on the melting efficiency of SA516 weldments produced using 800 A.

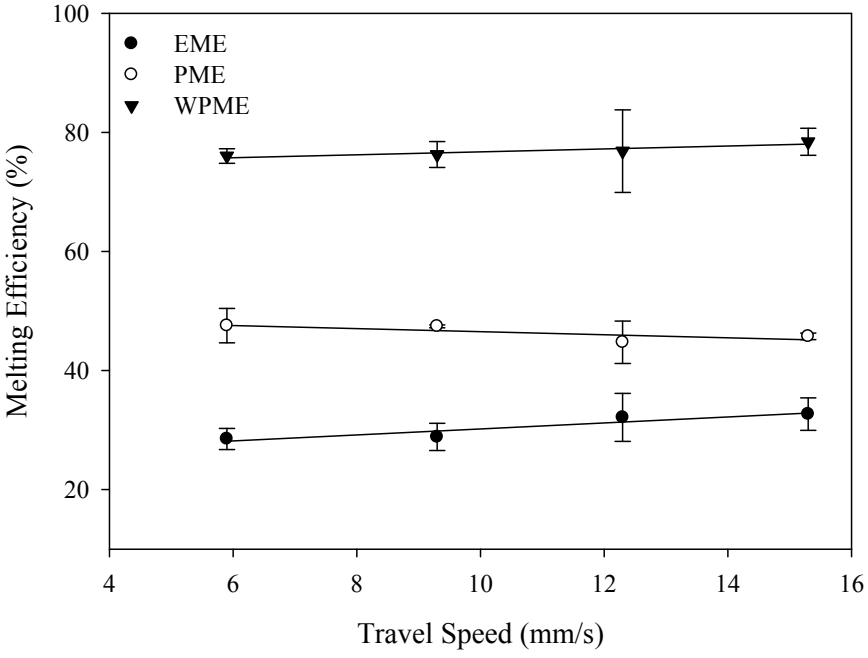

Figure 4.36. Effect of travel speed on the melting efficiency of SA516 weldments produced using 850 A.

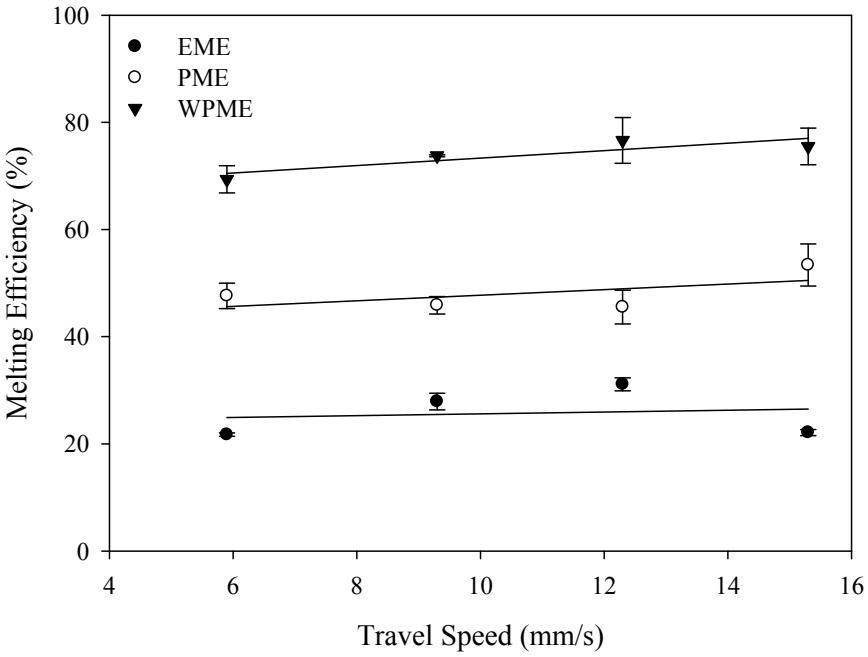

Figure 4.37. Effect of travel speed on the melting efficiency of A709 weldments produced using 700 A.

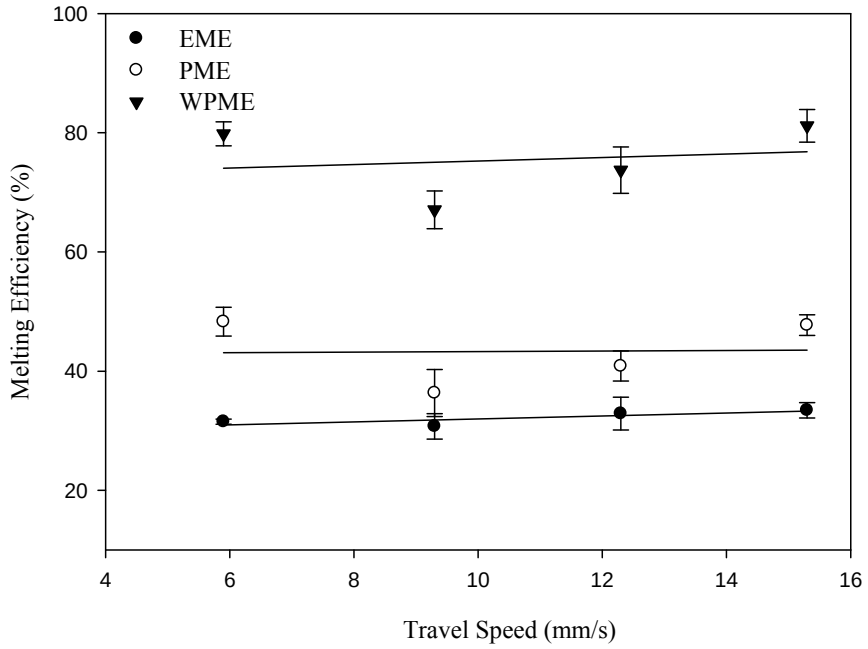

Figure 4.38. Effect of travel speed on the melting efficiency of A709 weldments produced using 850 A.

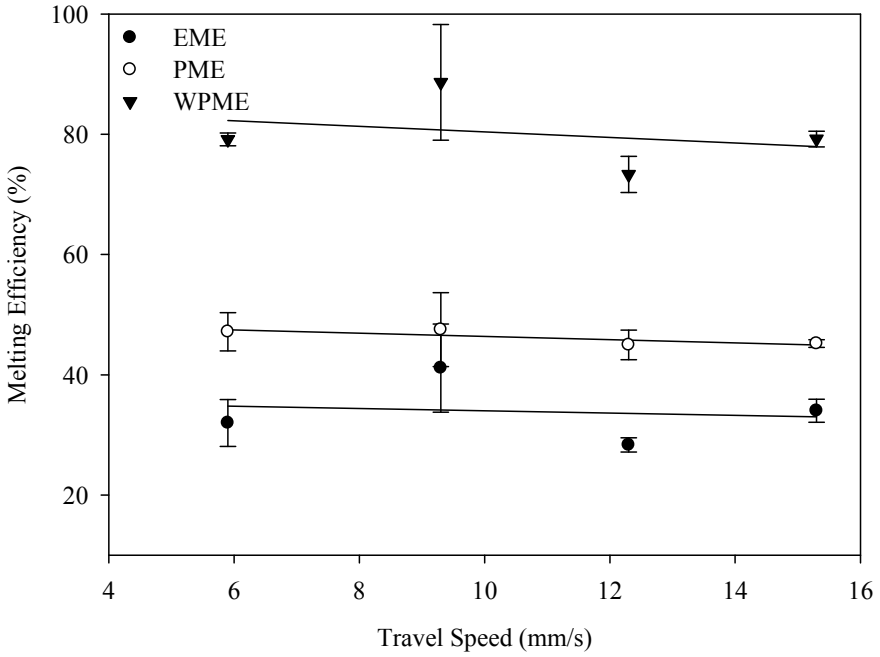

Figure 4.39. Effect of travel speed on the melting efficiency of A709 weldments produced using 800 A.

4.4 Mechanical Properties of SA516 and A709 Materials

In this section, the results obtained from tensile testing, microhardness measurements, Charpy impact testing, metallograhic examination and Scanning Electron Microscopy (SEM) are presented for SA516 and A709 weldments. The correlations between microstructure, hardness, strength and Charpy impact toughness of both materials are established and discussed with respect to the SAW process variables.

4.4.1 Hardness of SA516 Weldments

The variation of microhardness with distance from the weld center of SA516 weldments for various welding current-travel speed combinations are shown in Figures 4.40-4.42. The errors bars shown in the figures are standard deviations of the measurements. From these figures it can be seen that the parent metal has the lowest hardness among all weldment regions, while the hardness of the weld interface or coarse grained HAZ (CGHAZ) is the highest. The average hardness of the WM is higher than the hardness in FGHAZ. Therefore, the hardness relationship in SA516 weldments regions can be expressed as follows: $VHN_{WI} > VHN_{CGHAZ} > VHN_{WM} > VHN_{FGHAZ} > VHN_{PM}$.

Generally, the bulk hardness of a metal is determined by the hardness of different phases in it. Therefore, it is very important to investigate the relationship between the hardness and microstructures of different weld zones of SA516. Figures 4.43-4.47 show typical microstructures of the the parent metal (PM), weld interface (WI), coarse grained HAZ (CGHAZ), fine grained HAZ (FGHAZ) and weld metal of SA516, respectively. These figures show the microstructures formed in the different weld zones. The microstructure of parent metal of SA516 shown in Figure 4.43 is characterized by proeutectoid ferrite (F) and pearlite (P). Figure 4.44 shows the weld interface which separates the weld metal and the CGHAZ. Figure 4.45 shows that the main microstructures of the CGHAZ consisted of interlocking lath of ferrite, network of prior austenite grain boundary and

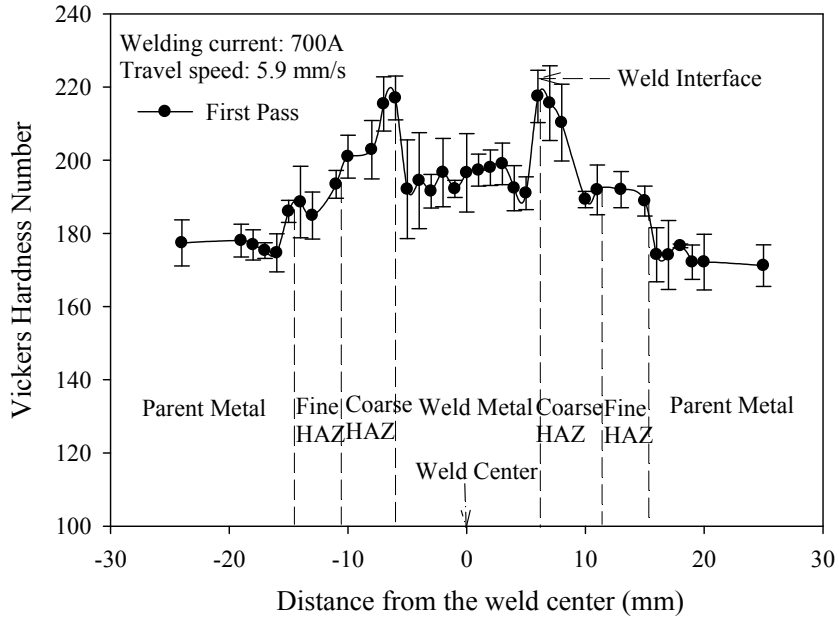

Figure 4.40. Variation of hardness with distance from the weld center of a SA516 steel weldment produced using 700 A and 5.9 mm/s.

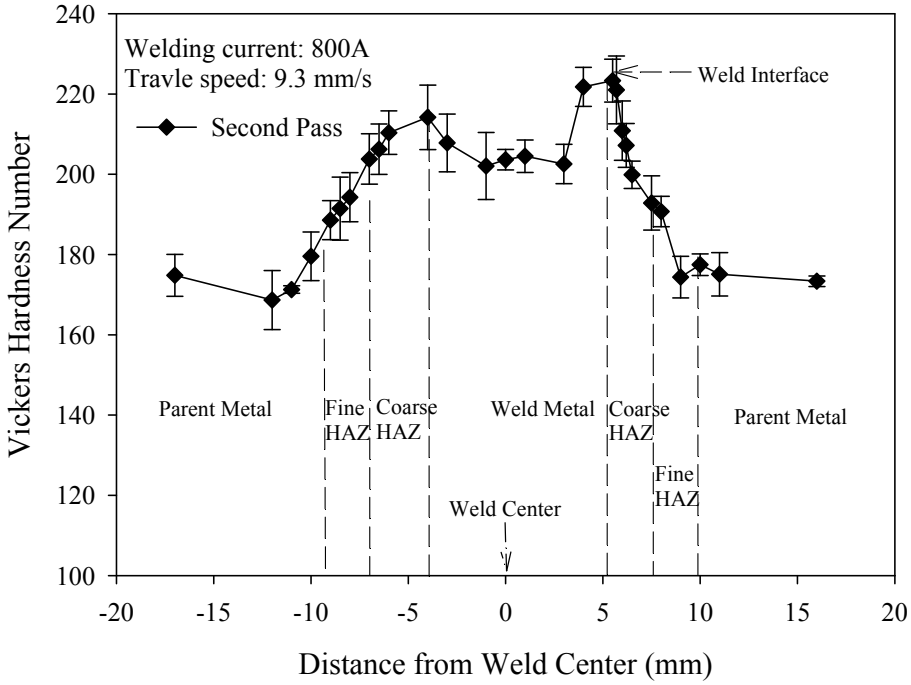

Figure 4.41. Variation of hardness with distance from the weld center of a SA516 steel weldment produced using 800 A and 9.3 mm/s.

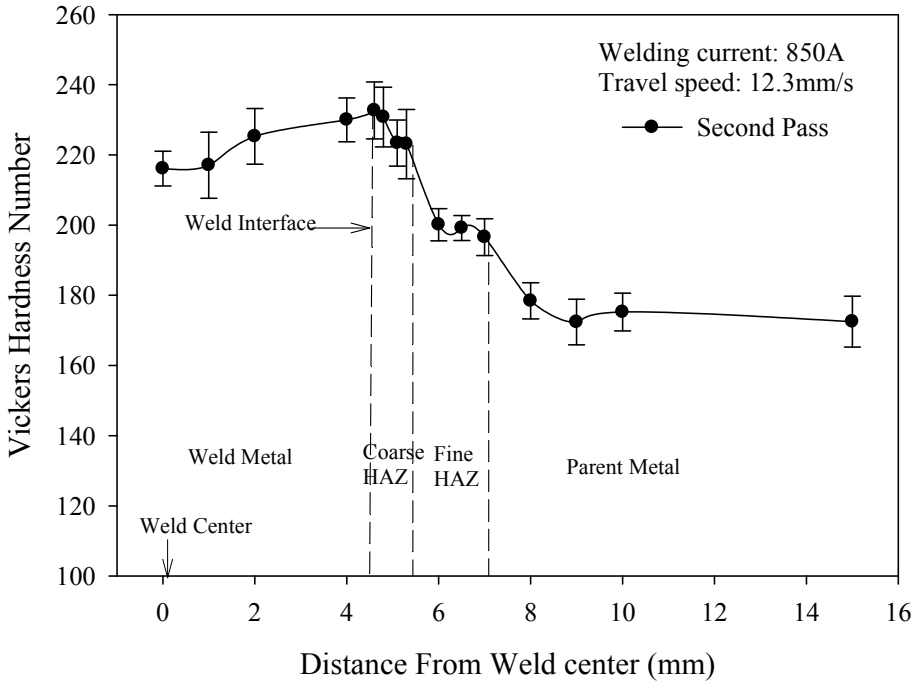

Figure 4.42. Variation of hardness with distance from the weld center of a SA516 steel produced using 850 A and 12.3 mm/s.

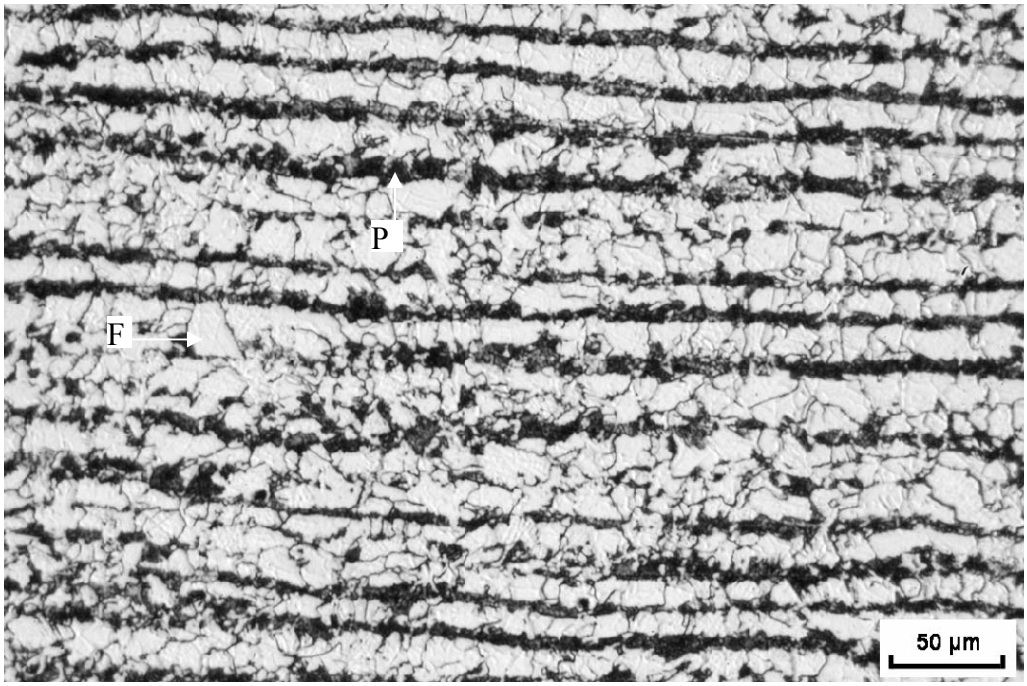

Figure 4.43. Optical micrograph of SA516 parent metal. F = Ferrite; P = Pearlite.

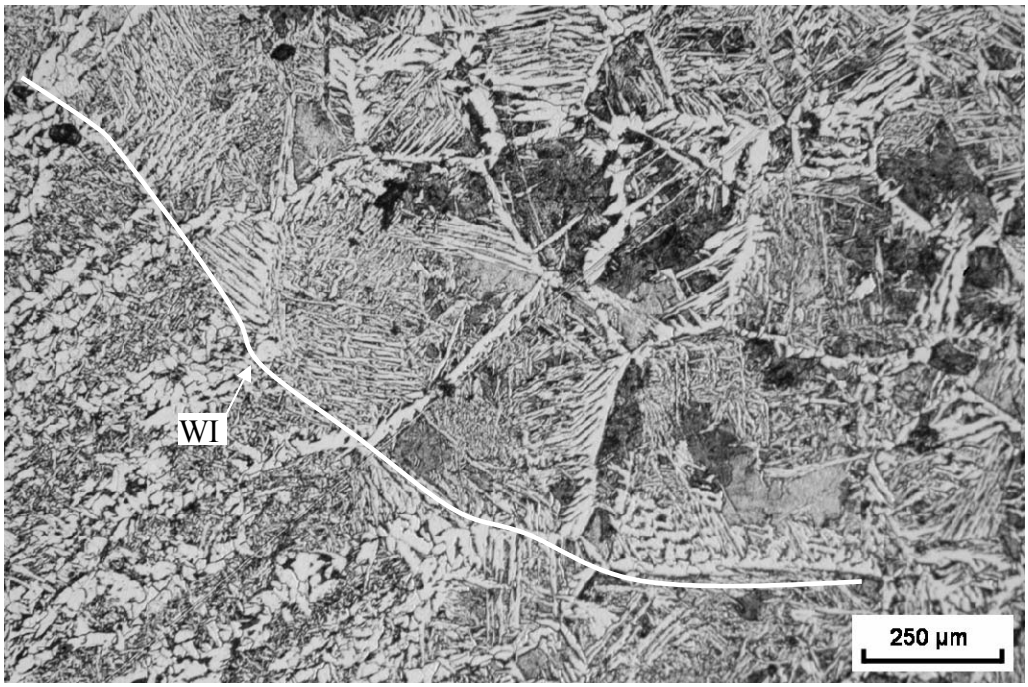

Figure 4.44. Optical micrograph of the weld interface of SA516 weldment produced using 700 A and 5.9 mm/s.

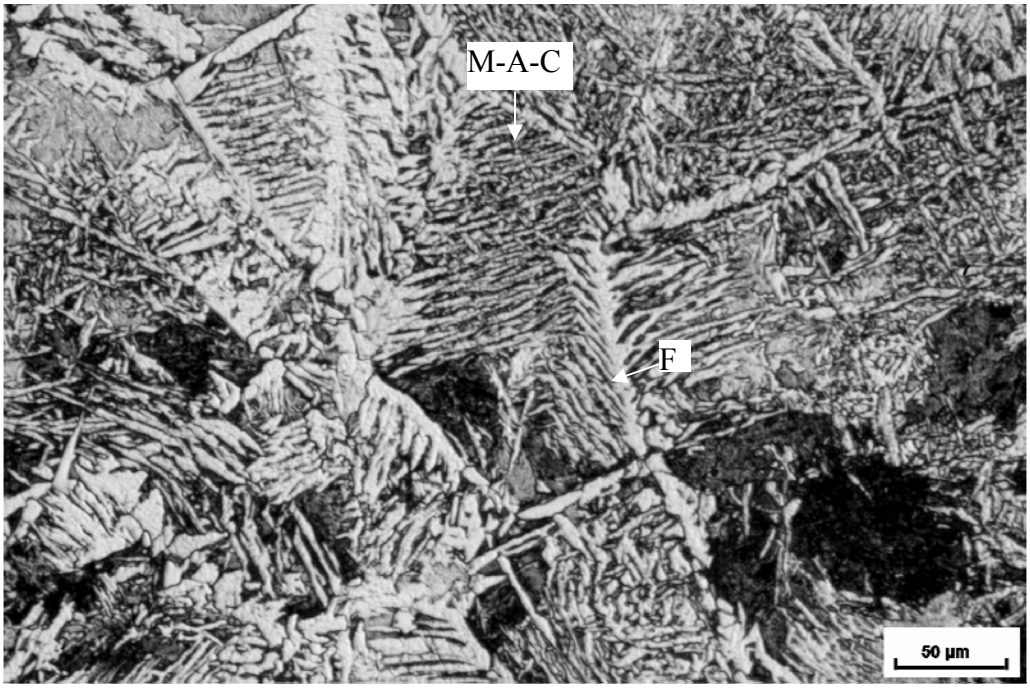

Figure 4.45. Optical micrograph of the CGHAZ of SA516 weldment produced using 800 A and 5.9 mm/s. F = Ferrite; M-A-C = Martensite, Austenite, Carbide.

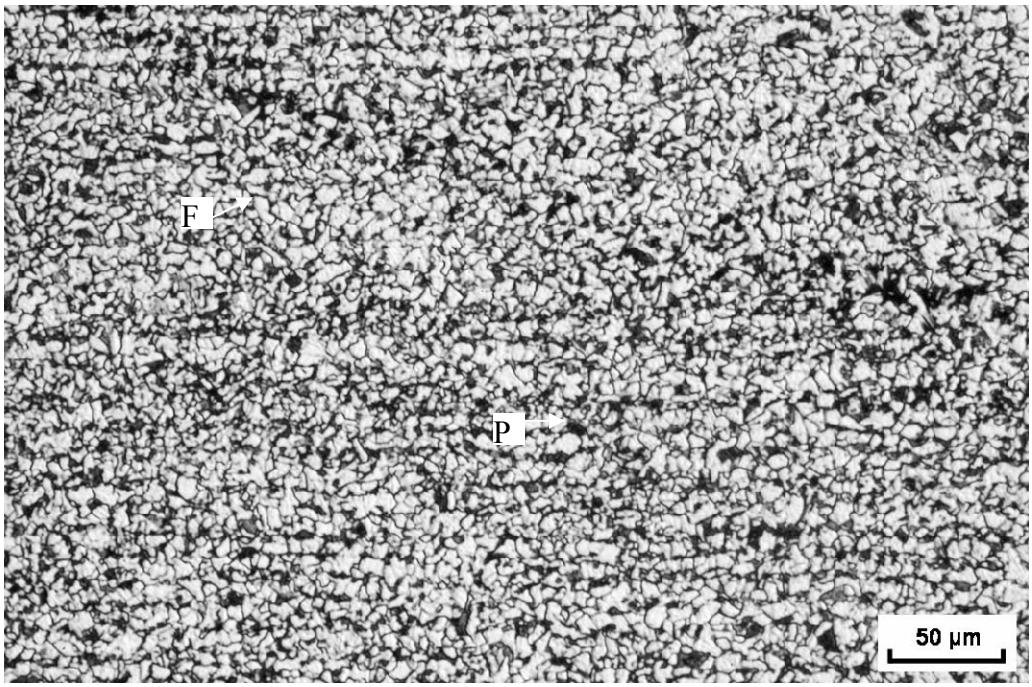

Figure 4.46. Optical micrograph of the FGHAZ of SA516 weldment produced using 800 A and 5.9 mm/s. F = Ferrite; P = Pearlite.

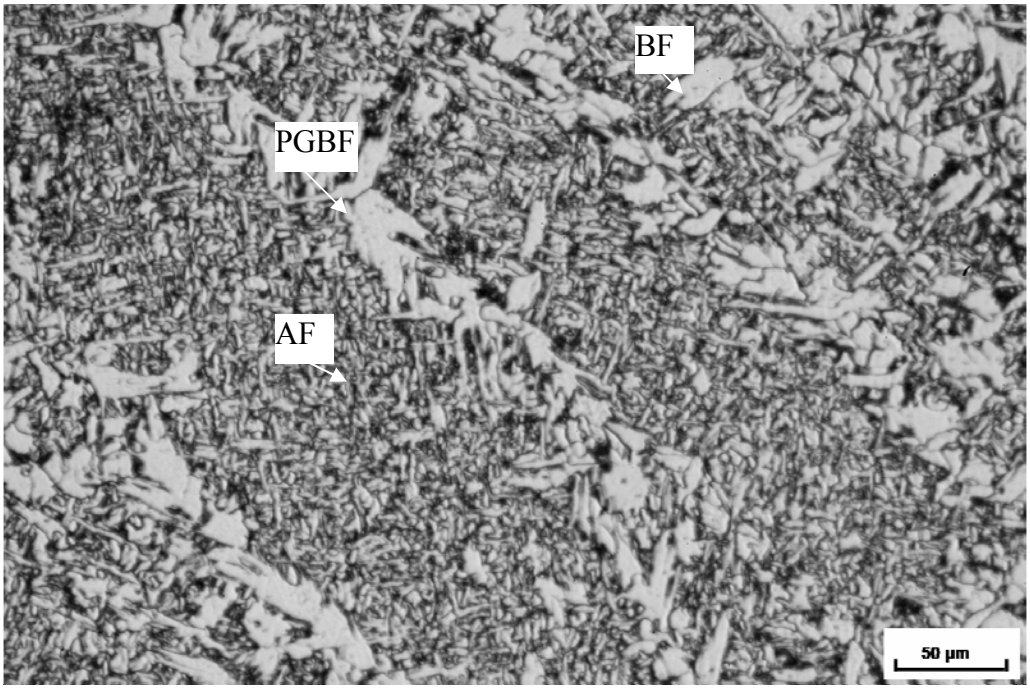

Figure 4.47. Optical micrograph of weld metal of SA516 weldment produced using 800 A and 5.9 mm/s. PGBF = Polygonal Grain Boundary Ferrite; BF = Block Ferrite; AF = Acicular Ferrite.

carbide or martensite, which is named M-A-C (martensite, austenite, carbide). The microstructure of the FGHAZ, which is characterized by fine-grained polygonal ferrite and pearlite, is shown in Figure 4.46. The weld metal (see Figure 4.47) has a large volume fraction of acicular ferrite (AF) in addition to polygonal grain boundary ferrite (PGBF) and block ferrite (BF).

The high hardness in the weld interface or CGHAZ can be explained using the transformation of the weldment microstructures during the SAW process. The microstructures of CGHAZ can be related to two transformation steps, namely: (i) The δ-Fe to γ-Fe transformation in the CGHAZ close to WI at high temperatures. The newly formed austenite has a sufficient time to grow resulting in a large grain size. (ii) As the cooling rate in the GCHAZ region is fast and the carbon content of the parent metal is 0.22 wt.%, therefore the second transformation is from γ-Fe to pearlite, bainite or martensite. The closer to the weld interface and the faster the cooling rate, the greater is the fraction of martensite or bainite formed in the CGHAZ. Since the hardness of martensite or bainite is very high, the highest hardness was found in weld interface or CGHAZ.

The high hardness in the weld metal is due to the presence of acicular ferrite. Although the term acicular means the object is shaped and pointed like a needle, it is generally recognized that acicular ferrite has the morphology of thin, lenticular plates in three–dimensions [26]. The plates of acicular ferrite nucleate intragranularly on non-metallic inclusions within large austenite grains, and then radiate in many different orientations from those inclusions whilst maintaining an orientation relationship with the austenite [26]. The resulting microstructure is less organized when compared to ordinary bainite or Widmanstatten ferrite, where there is a tendency to form packets of parallel plates which are identically oriented [26]. Therefore, the acicular ferrite microstructure has the potential of combining high strength and high toughness. Thus, the hardness of the weld metal is also very high.

Compared to the parent metal (SA516), the phases in FGHAZ are the same as those phases in the parent metal, except that the grain size of the phases in the FGHAZ is smaller than those of the parent metal. The quantitative relationship between yield strength and grain size in metals is described by the Hall-Petch equation [65].

$$\sigma_y = \sigma_i + k_y d^{-1/2} \qquad 4.2$$

where σ_y is the lower yield strength, σ_i is the friction stress, k_y is the strengthening coefficient and d is the grain size.

From equation 4.2, it can be seen that yield strength increases with decreasing grain size. In general, the grain size of the the FGHAZ is smaller than that of the parent metal. Therefore, the yield strength of the FGHAZ is greater than that of the parent metal. Thus, the hardness of the FGHAZ is greater than that of the parent metal.

Figure 4.48 shows the effect of heat input on the hardness of SA516 weldments. It indicates that the hardness of the WM, WI, and CGHAZ decrease appreciably with increasing heat input, while it has little effect on the hardness of the PM and FGHAZ. Both thermal gradient and cooling rate decrease with increasing heat input in the weldments. From the Continuous Cooling Transformation (CCT) diagram shown in figure 4.49, fast cooling rate will result in increased fraction of hard phases, such as martensite and bannite. The normal way to calculate the strength of a multiphase alloy is to use the rule of mixtures, i.e., to estimate a mean value from the weighted average of each component [26]:

$$\sigma = V_\alpha \sigma_\alpha + V_\beta \sigma_\beta \qquad 4.3$$

where σ is the strength of a multiphase alloy, V_α is the volume fraction of α phase in the alloy, σ_α is the strength of α phase, V_β is the volume fraction of β phase in the alloy, σ_β is the strength of β phase.

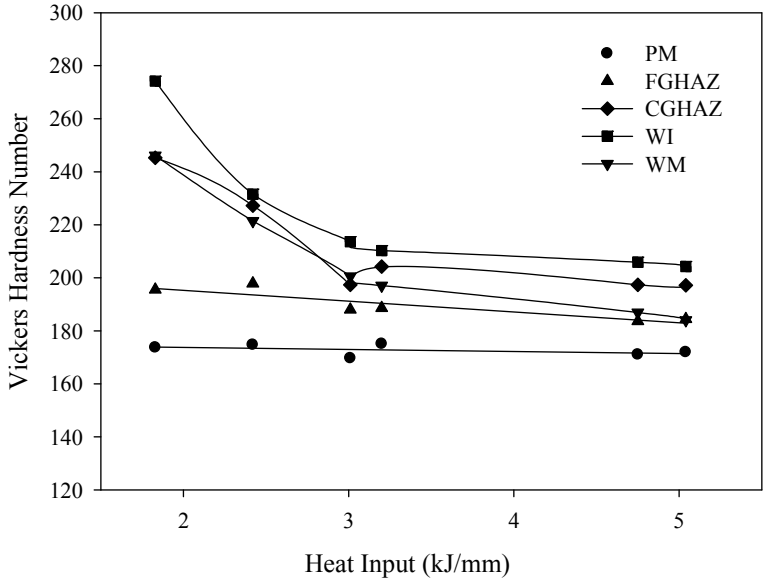

Figure 4.48. Effect of heat input on the hardness of SA516 weldments (first pass).

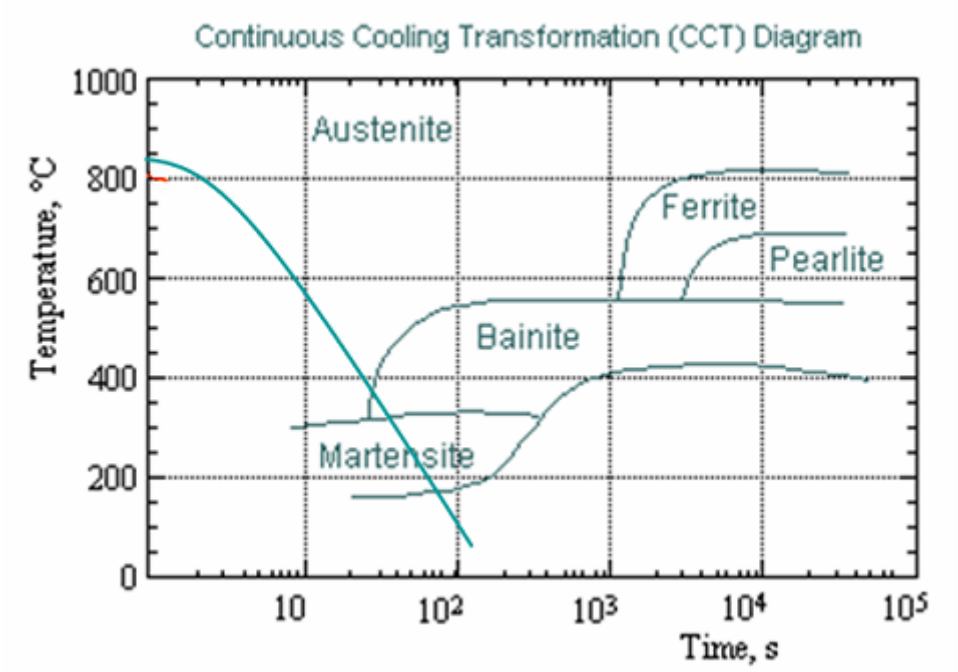

Figure 4.49. Fast cooling rate on a CCT diagram for 0.4 wt.% C, 1.5 wt.% Mn, 0.5 wt.% Mo carbon steel [66].

When heat input decreases during the welding process, the deposition rate will decrease too. So, the weldment will cool down fast. Therefore, the fraction of martensite will increase in the CGHAZ. Thus, the fraction of other phases such as boundary ferrite will decrease. According to equation 4.3, the strength of the CGHAZ will increase because martensite is stronger than other phases. The same reason can be used to explain the behaviour of the weld metal. As for the weld interface, its behaviour is the same as that of the weld metal and CGHAZ because the microstructure of the weld interface is a mixture of weld metal and CGHAZ.

Figure 4.48 shows that the hardness of the parent metal and FGHAZ did not change much with heat input because the phases in these zones are ferrite and pearlite. The fractions of ferrite and pearlite in these zones do not change because these fractions were decided by the composition of the parent metal, especially the carbon content. Since the composition did not change in these zones, the strength of the parent metal and FGHAZ remained practically unchanged during the SAW process.

4.4.2 Hardness of A709 Weldments

Figures 4.50 to 4.52 show the variation of hardness with distance from the weld center for A709 weldments produced using various combinations of welding current and travel speed. From these figures, it can be seen that the hardness of A709 weldments decreases with distance from the weld center. That means the weld metal has the highest hardness, while the parent metal has the lowest hardness. Therefore, the hardness relationship among A709 weld zones can be expressed as follows: $VHN_{WM} > VHN_{WI} > VHN_{CGHAZ} > VHN_{FGHAZ} > VHN_{PM}$.

Figures 4.53 to 4.57 show typical microstructures of the parent metal, weld interface, CGHAZ, FGHAZ and weld metal of A709 steel, respectively. It can be seen that various types of microstructures are formed in the different weld zones during the SAW process. The microstructure of the normalized A709 parent metal shown in Figure 4.53 is

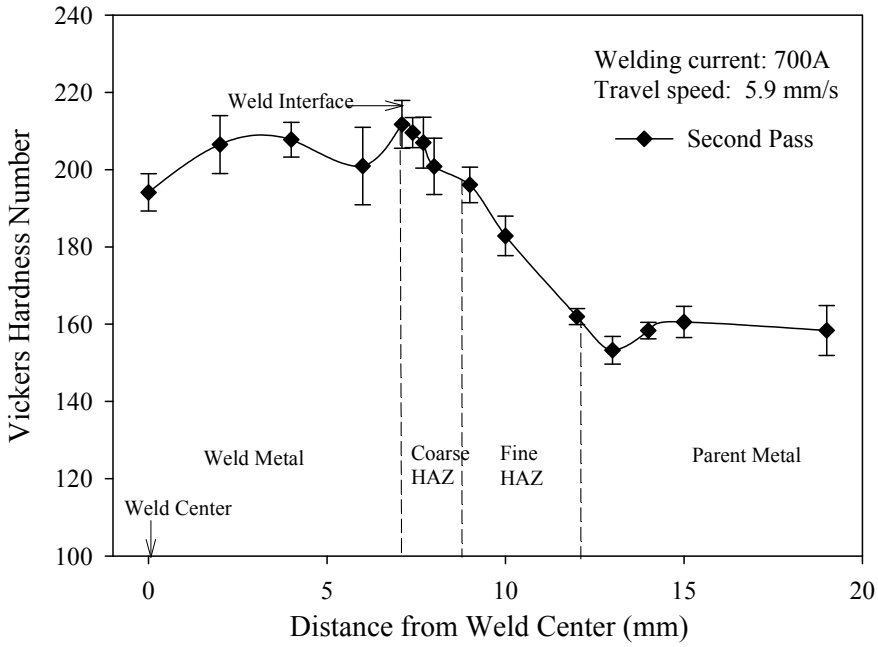

Figure 4.50. Variation of hardness with distance from the weld center of an A709 steel weldment produced using 700 A and 9.3 mm/s.

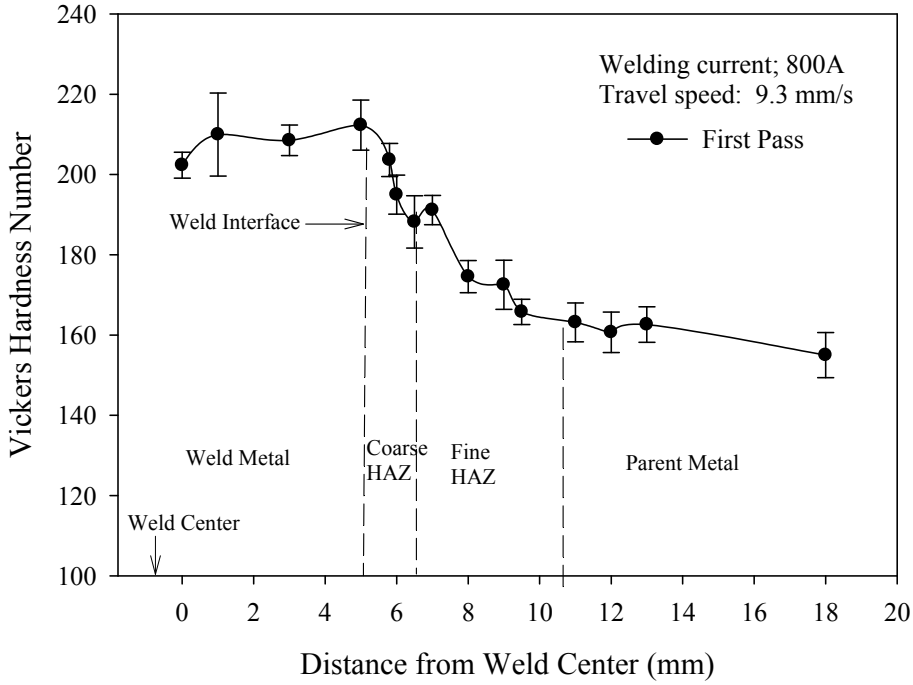

Figure 4.51. Variation of hardness with distance from the weld center of an A709 steel weldment produced using 800 A and 9.3 mm/s.

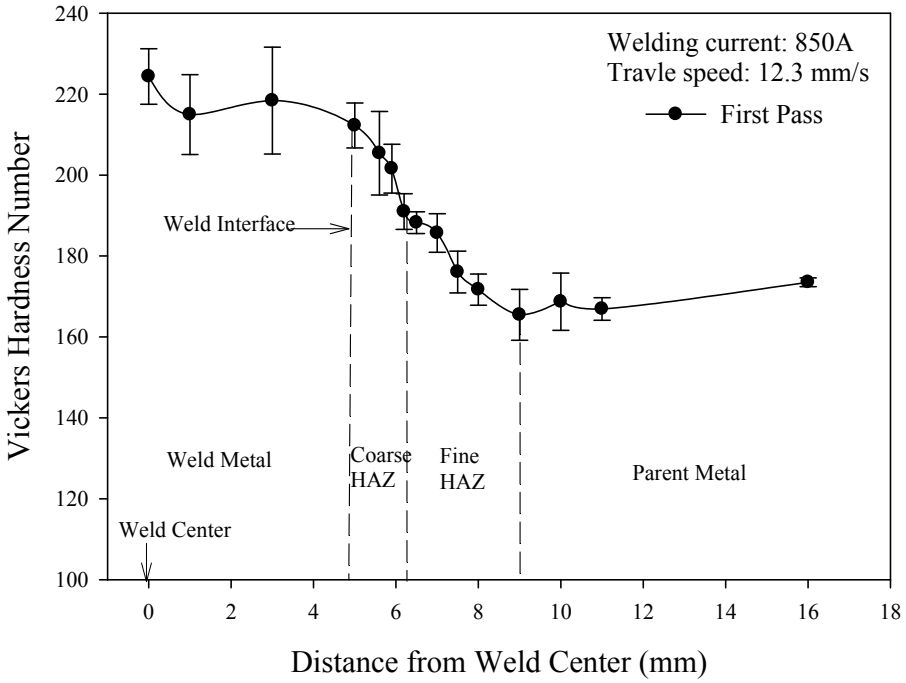

Figure 4.52. Variation of hardness with distance from the weld center of an A709 steel weldment produced using 850 A and 12.3 mm/s.

characterized by proeutectoid ferrite (white) and pearlite (black). The fraction of pearlite is very small since the carbon content of A709 steel is low (0.04 wt.% C). Figure 4.54 shows the weld interface which separates the weld metal and the CGHAZ. Figure 4.55 shows the microstructures of the CGHAZ consisted mainly of polygonal ferrite and acicular ferrite. The microstructure of the FGHAZ, which is characterized by fine-grained polygonal ferrite (white) and pearlite (black), is shown in Figure 4.56. The microstructure of the weld metal is shown in Figure 4.57 and is characterized by large columnar structures with a large volume fraction of acicular ferrite and grain boundary ferrite.

As mention in section 2.2.2, the acicular ferrite existing in the weld metal resulted in its high hardness because of its needle-shape morphology. Both materials used the same type of electrode with carbon content of 0.1 wt.% because the same weld procedure was used in SA516 and A709 steels. The carbon content of the weld metal of A709 weldments is lower than that of SA516 weldments because the carbon contents of the parent metals of SA516 and A709 are 0.22 wt.% and 0.04 wt.%, respectively. Therefore,

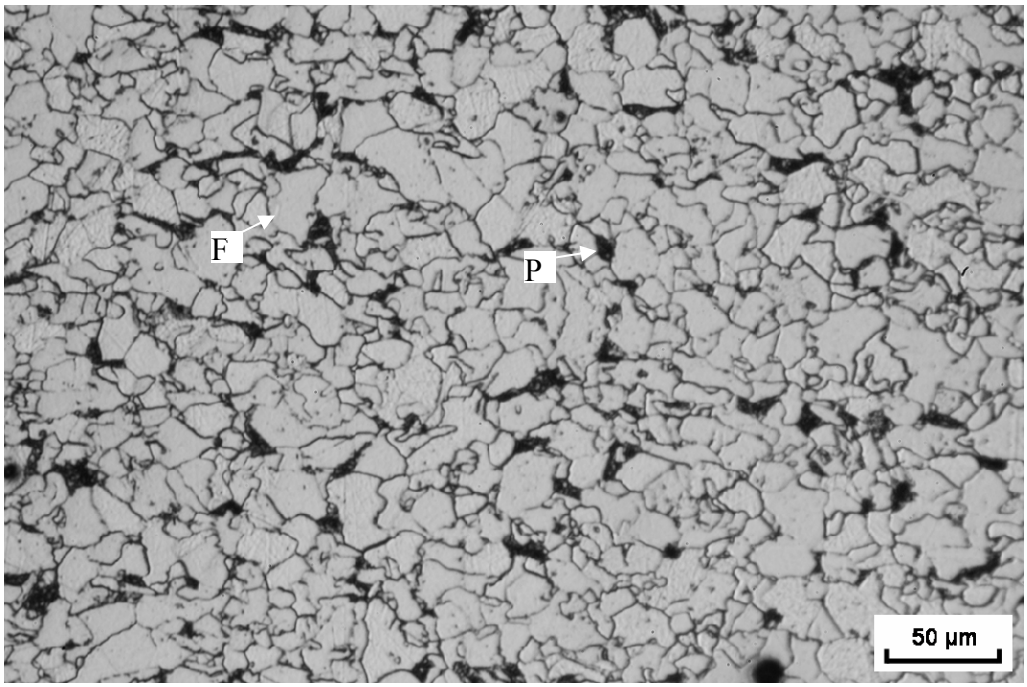

Figure 4.53. Optical micrograph of the parent meal of A709. F = Ferrite; P = Pearlite.

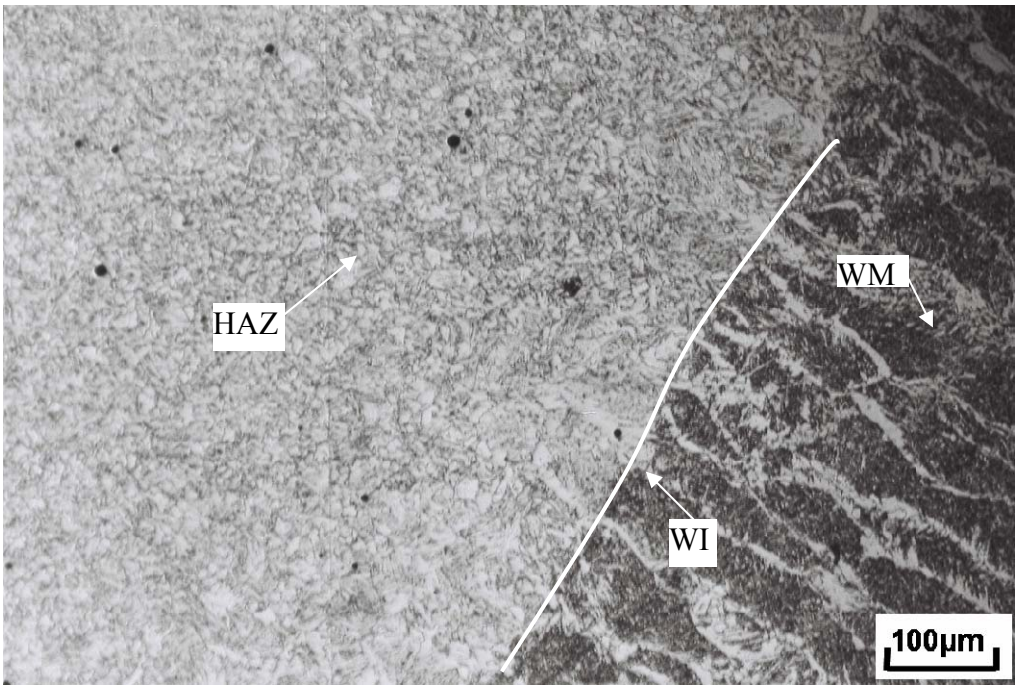

Figure 4.54. Optical micrograph of the weld interface of an A709 steel weldment produced using 700 A and 9.3 mm/s.

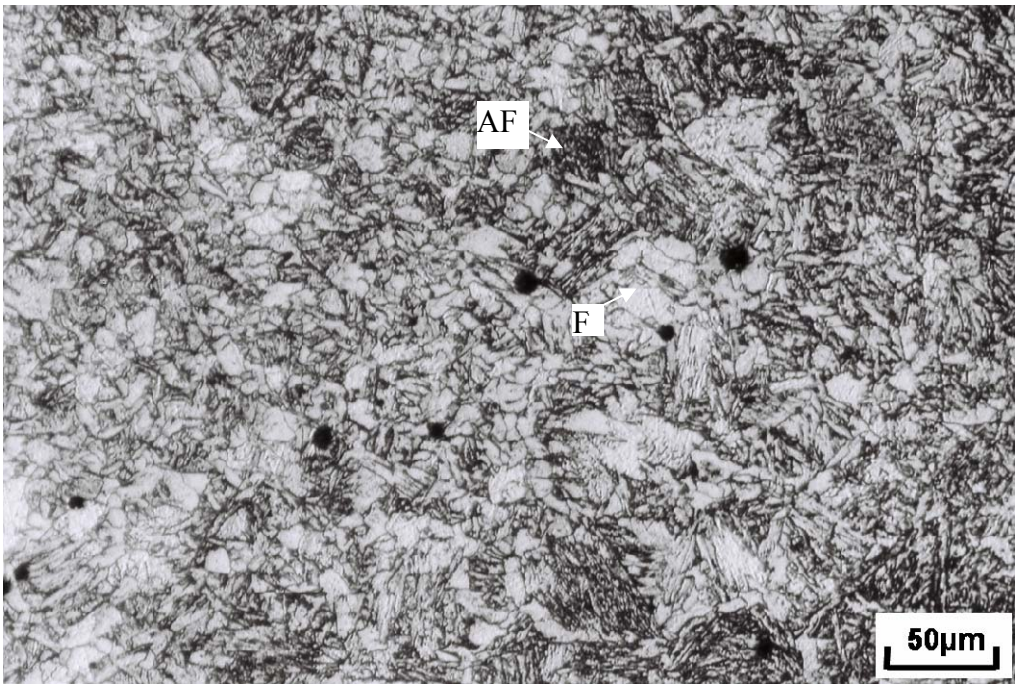

Figure 4.55. Optical micrograph of the CGHAZ of an A709 steel weldment produced using 700 A and 5.9 mm/s. AF = Acicular ferrite; F = Ferrite.

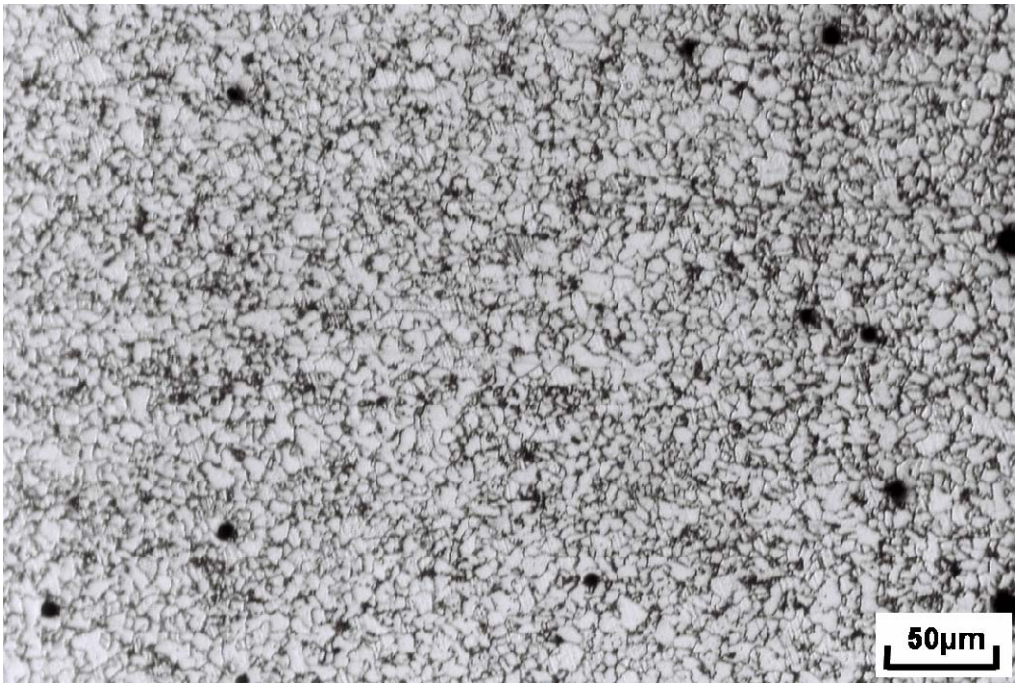

Figure 4.56. Optical micrograph of the FGHAZ of an A709 steel weldment produced using 700 A and 5.9 mm/s.

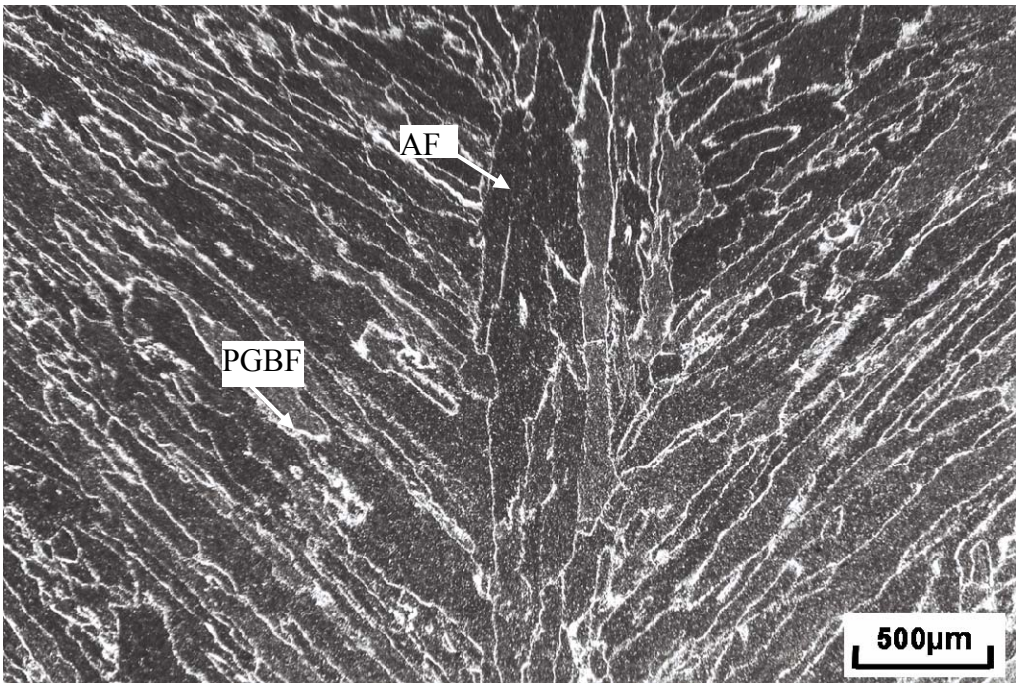

Figure 4.57. A typical optical micrograph of the weld metal of an A709 steel weldments produced using 700 A and 12.3 mm/s. AF = Acicular ferrite; PGBF = Polygonal Grain Boundary Ferrite;

the carbon content of the weld metal of A709 should be less than 0.1 wt.% because of the carbon content dilution from the electrode and the parent metal. For the same reason, the carbon content of the weld metal of SA516 could be more than 0.1 wt.%. In general, high carbon content will result in martensite formation at high cooling rates. Therefore, for the same SAW variables, the highest hardness obtained for SA516 weldments would be higher than that obtained for A709 weldments.

No martensite was formed in the CGHAZ of A709 weldments studied and this might be due to the very low carbon content of the steel. As a result of large grain size and fast cooling rate in this region, acicular ferrite or bainite will form in the CGHAZ. The hardness of this region (HV195 – HV210) is higher than that of the FGHAZ (HV170 – HV190) and the parent metal (HV155 –HV 170). The hardness of the weld metal (HV200 – HV220) is higher than that of the CGHAZ because of high fraction of acicular ferrite in the weld metal. Although the phases in the parent metal and the FGHAZ of

A709 steel are the same, the hardness of FGHAZ is higher than that of parent metal due to its small grain size.

Figure 4.56 shows the effect of heat input on the hardness of A709 weldments. It can be seen that the hardness of WM, WI and CGHAZ decrease slightly with increasing heat input, while heat input has little effect on the hardness of PM and FGHAZ. The Vickers hardness values for the WM, WI and CGHAZ varied from 202 to 220, 200 to 212, and 191 to 208, respectively. Although SAW parameters changed, the hardness just changed slightly in these weld zones. The reason for this behaviour is the combination of the alloying elements of the parent metal and the electrode. The carbon contents of the parent metal and the electrode are 0.04 wt.% and 0.1 wt.%, respectively. Although a decrease in heat input will cause the cooling rate to rise, the martensite phase cannot form because of the low carbon content in the parent metal. Therefore, the hardness cannot change very much when heat input decreases. However, high cooling rate does change the grain size in WM and CGHAZ. According to the equation 4.3, strength will increase when grain size decreases if the phases are the same in the metal. Therefore, the hardness of WM, WI and CGHAZ decreases slightly with increasing heat input as shown in Figure 4.58. The cooling rate of the FGHAZ remained virtually constant and no metallurgical change in the parent metal occurred although the SAW parameters changed. Therefore, the hardness of the FGHAZ and PM remained practically constant with increasing heat input.

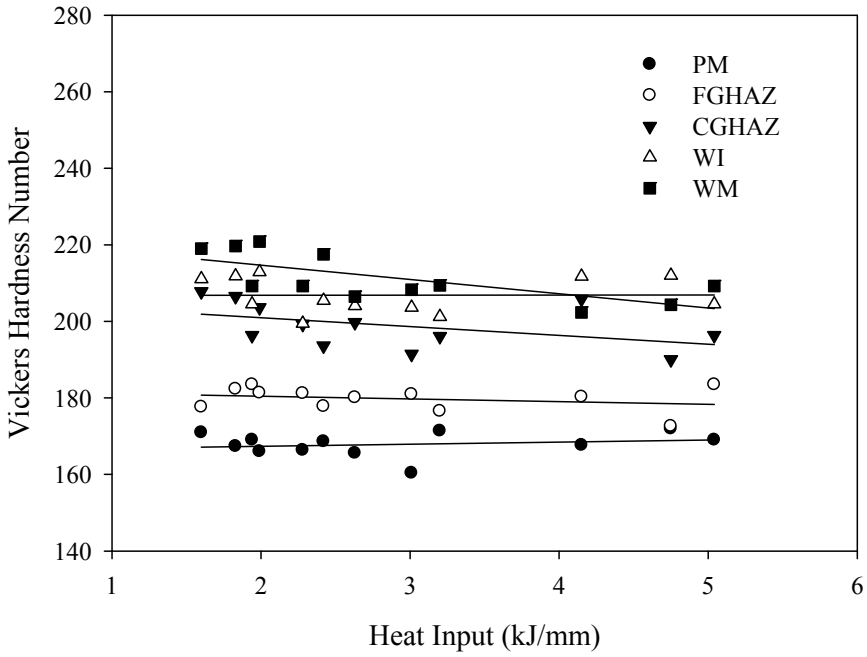

Figure 4.58. Effect of heat input on the hardness of A709 weldments (first pass).

4.4.3 Tensile Properties

Tensile testing was carried out to evaluate the effect of SAW variables on the yield strength (σ_y), tensile strength (σ_{ts}) and ductility (% Elongation) of the parent metals of SA516 and A709 and transverse weld samples of both materials. Typical fracture locations on the tensile specimens are shown in Figure 4.59, which shows the weld center, weld elongation, and percentage elongation. Here, weld elongation refers to the elongation which includes the whole weld zone within the gauge length (50.8 mm). Percentage elongation refers to the elongation which includes the whole fracture part within the gauge length (50.8 mm). It is observed that the fracture locations on the test specimens of SA516 and A709 occurred in the parent metal.

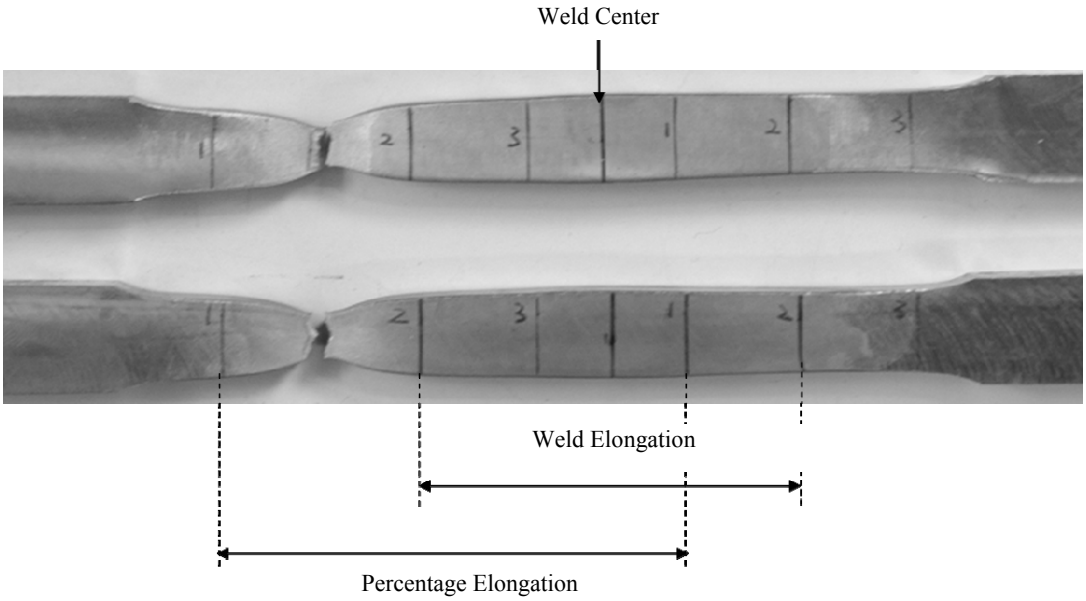

Figure 4.59. Fractured tensile specimens showing the weld center, weld elongation and percentage elongation within 50.8 mm gauge length.

Table 4.7 shows the average fracture strains for the parent metal and weldments of SA516, while similar results for A709 steel are shown in Table 4.8. As expected, the parent metals of both materials have the highest ductility. The fracture stains of SA516 and A709 are 56.7% and 51.4%, respectively. However, the fracture strains of SA516 weldments range from 29.5% to 35.6%. The fracture stains of A709 range from 27.6% to 37.5%. Therefore, the parent metals of both materials have better ductility than the weldments. Figure 4.60 shows typical stress-strain curves for the PM and weldments of SA516, while Figure 4.61 shows similar results for the PM and weldments of A709.

It can be seen from both figures that the yield strength (YS) and tensile strength (TS) of the test specimens remained practically unchanged although their fracture strains differed. Although some weldments had internal defects, their YS and TS were still in the same range as others. The YS and TS for SA516 weldments and PM varied from 323 MPa to 352 MPa and from 537 MPa to 550 MPa, respectively as shown in Figure 4.62. For weldments and PM of A709, they changed from 380 MPa to 407 MPa and 464 MPa to 471 MPa, respectively as shown in Figure 4.63.

Table 4.7 Average fracture strains of the PM and weldments of SA516.

Weld No.	PV1	PV5	PV6	PV7	PV8	PV8*
Strain (%)	30.9 ± 5.4	29.6 ± 1.9	31.8 ± 1.0	29.2 ± 1.1	33.4 ± 0.4	35.6 ± 1.1
Weld No.	PV9	PV10	PV11	PM		
Strain (%)	34.7 ± 2.4	32.7 ± 2.8	31.1 ± 0.2	56.7 ± 2.0		

Table 4.8 Average fracture strains of the PM and weldments of A709.

Weld No.	WT1	WT2	WT3	WT3*	WT4*	WT5
Strain (%)	27.6 ± 1.7	32.1 ± 2.2	33.7 ± 1.5	32.4 ± 2.3	31.7 ± 0.4	37.5 ± 1.0
Weld No.	WT6	WT7	WT8	WT8*	WT9	WT10
Strain (%)	33.5 ± 3.1	37.2 ± 0.8	38.5 ± 1.2	35.2 ± 2.4	36.5 ± 0.6	35.2 ± 3.7
Weld No.	WT11	WT12	PM			
Strain (%)	31.9 ± 2.3	35.5 ± 1.4	51.4 ± 4.5			

*Note: The test specimens have internal defects.

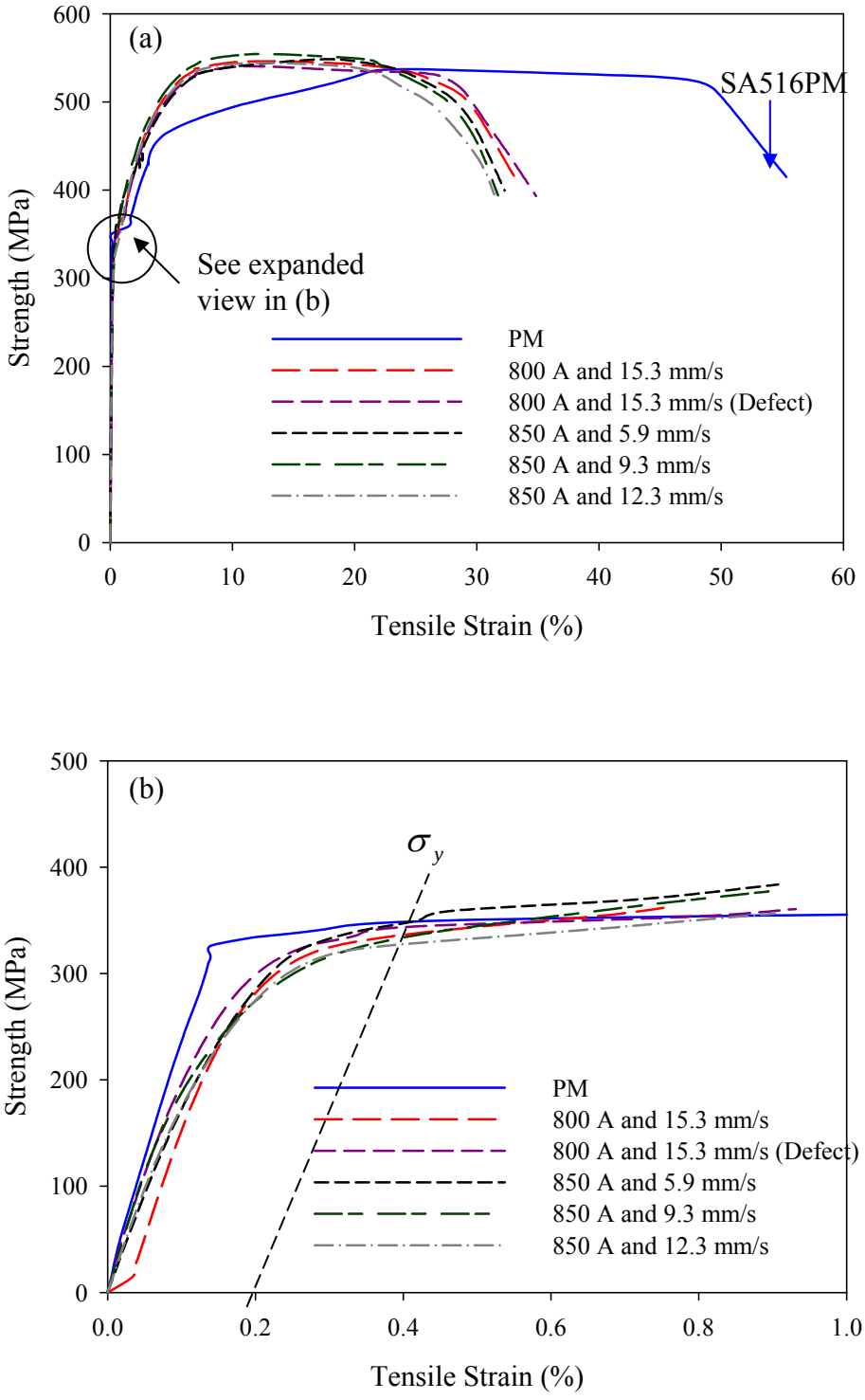

Figure 4.60. Typical stress–strain curves of the PM and weldments of SA516.

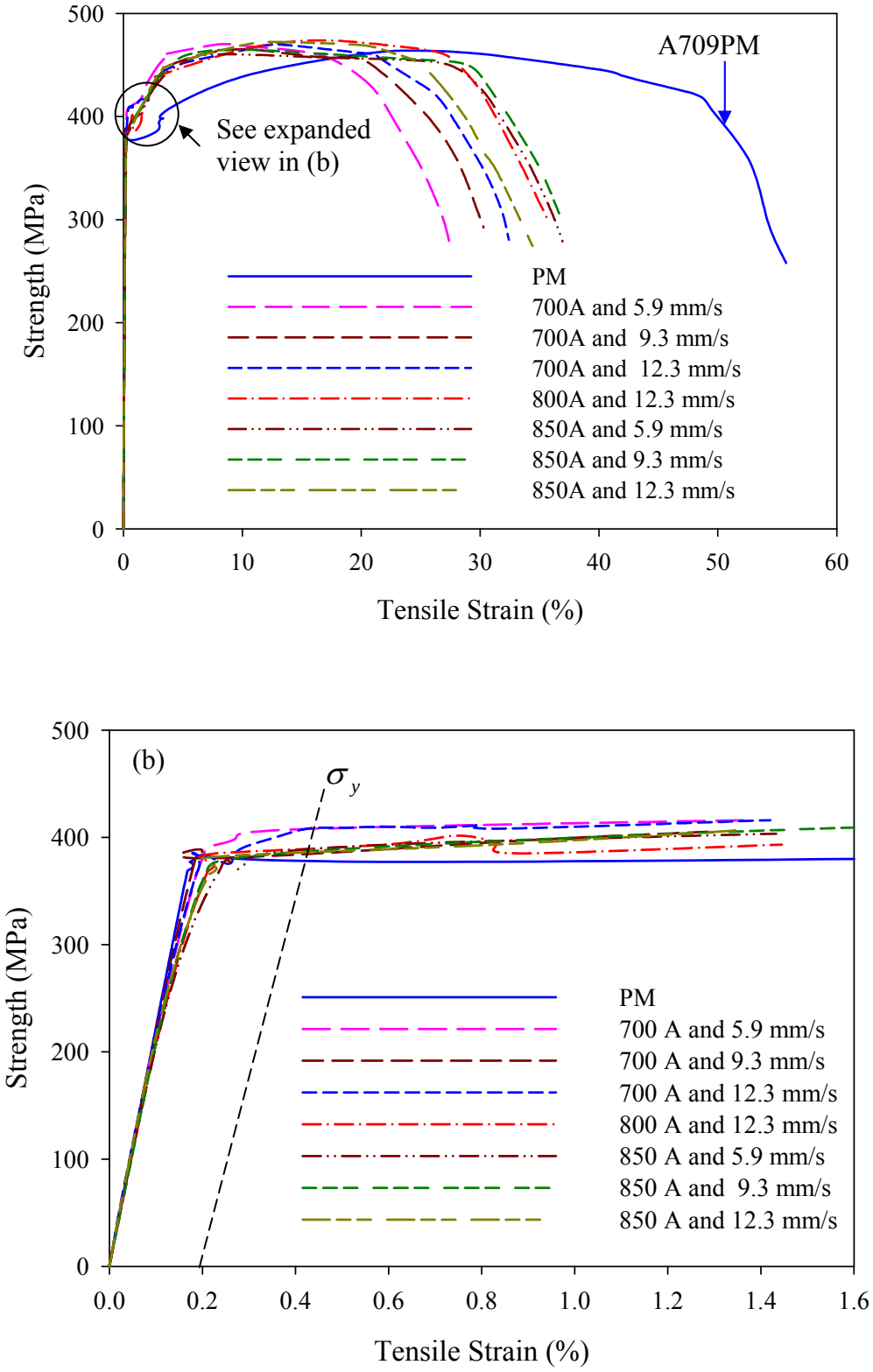

Figure 4.61. Typical stress–strain curves of the PM and weldments of A709.

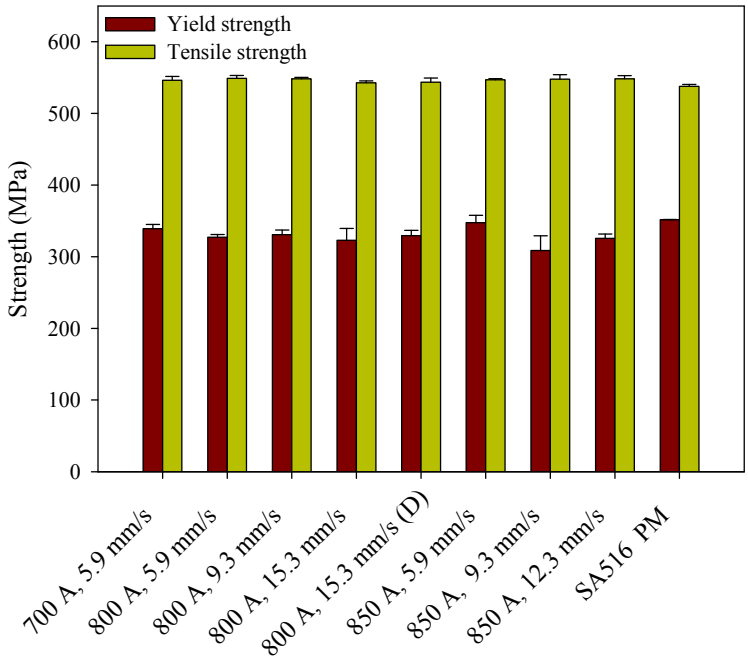

Figure 4.62. Yield and tensile strengths of the PM and weldments of SA516.

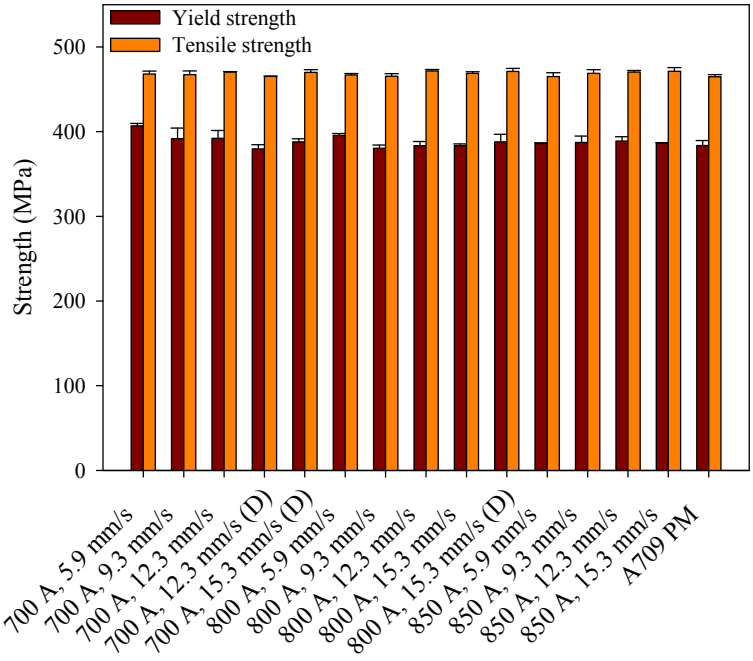

Figure 4.63. Yield and tensile strengths of the PM and weldments of A709.

Although the YS and TS are different for each of the test specimens, actually the differences in YS and TS are less than 20 MPa and 10 MPa, respectively. Since all the specimens broke in the PM, the YS and the TS values obtained from the weldments are almost the same as those of their parent metals. These results are consistent with the hardness test as mentioned in section 4.4.1 and 4.4.2. Although some weldments suffered lack of penetration, their tensile specimens did not break at the weld metal zone. The reason is that the width of the tensile specimens is 12.7 mm, while the largest weld defect in the weld metal of both materials is approximately 3.6 mm, thus the effective width of the weld metal is at least 9.1 mm. Since the width of each test specimen is practically the same, then the effective area in the location where lack of penetration occurred is proportional to the effective thickness of the test specimen. Therefore, the effective area in this location is more than 70% area of the parent metal. The average hardness of the weld metal is at least 1.4 times the hardness of the parent metal from the hardness testing. Thus, the strength of the weld metal with lack of penetration is at least the same as the parent metal.

Figures 4.64 and 4.65 show that the weld elongation increases with increasing travel speed. This behaviour can be explained as follows. The total elongation of the weldment is a combination of the elongation of the weld joint and that of the parent metal. For different SAW parameters the length of the parent metal, weld bead size and HAZ size within the gauge length (50.8 mm) are different because the weld bead width and HAZ size varied with different SAW variables. Both decrease with increasing travel speed. That means the length of the parent metal within the gauge length was larger for high travel speeds than for low travel speeds. As mentioned above, the parent metal has better ductility than the weldments. Thus, the ductility of parent metal will be the major factor affecting the percentage elongation of the weldments.

Another factor that affects the percentage elongation is the weld joint elongation. The hardness results shown in Figure 4.48 indicate that the hardness of the WM and HAZ increase with increasing travel speed. Generally, high hardness means low ductility and elongation. Therefore, the weld joint elongation decreases with increasing travel speed. If

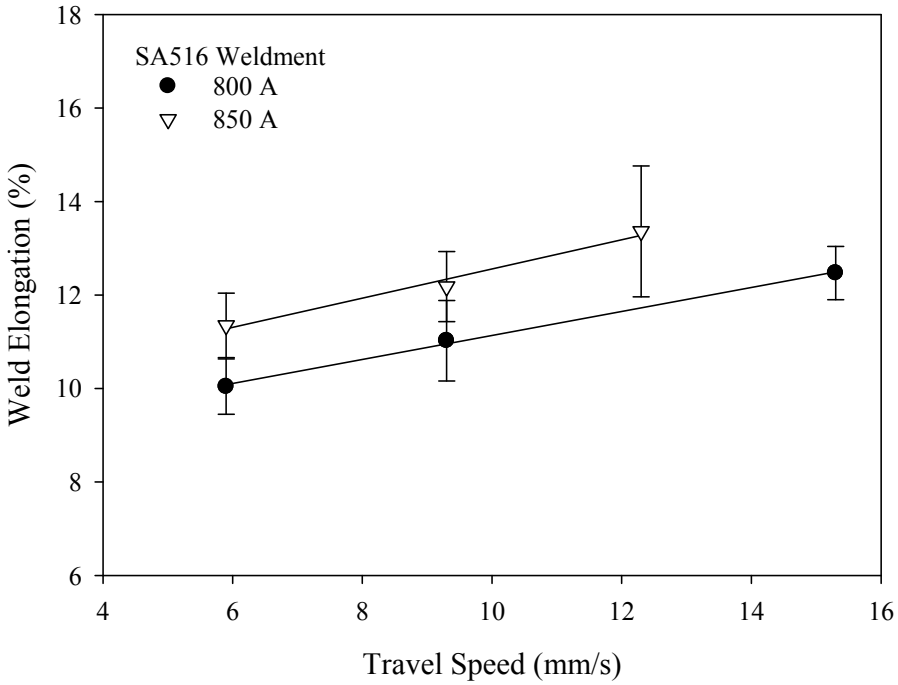

Figure 4.64. Effect of travel speed on the weld elongation of SA516 weldments.

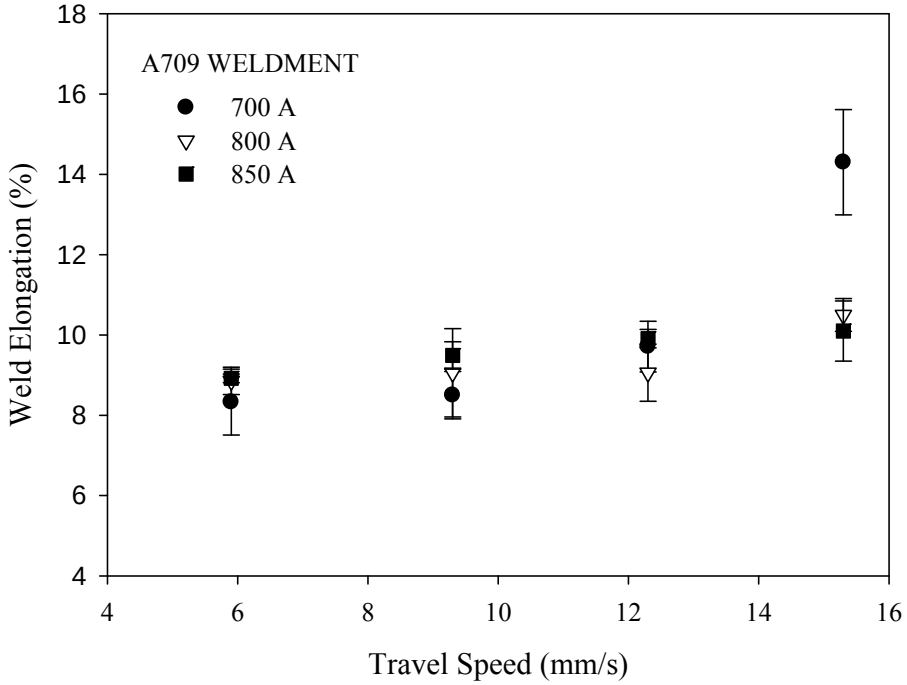

Figure 4.65. Effect of travel speed on the weld elongation of A709 weldments.

the weld bead width and HAZ size remain unchanged when SAW parameters are varied, the percentage elongation will decrease with increasing travel speed. However, the weld bead width and HAZ size at low travel speeds are greater than those at high travel speeds. Thus, the elongation of the WM and HAZ regions is less than that of the parent meal.

From the weld bead geometry measurement, the bead width for the lowest travel speed is 25 mm, while the bead width for the highest travel speed is 12 mm. Since the gauge length is the same for all the test specimens, the length of the parent metal for lowest travel speed specimen is 25.8 mm, while the length of the parent metal for the highest travel speed is 38.8 mm. Therefore, the difference in length of parent metal within the gauge length is 13 mm between both specimens. Although the ductility of the weld metal for the highest speed specimen is lower than that of the weld metal of the lowest speed specimen, 13 mm of the parent metal can contribute more elongation than 13 mm of the weld metal for the lowest travel speed specimen. Therefore, the elongation for the highest travel speed is higher than that for the lowest travel speed. As for percentage elongation, the gauge length of some test specimens included the whole weld joint, while some of them included part of the weld joint.

Figure 4.66 shows the effect of weld defects on percentage of elongation of the weldments of SA516 and A709. No lack of penetration was found in the weldments using welding current 850 A. Therefore no data from weldments using weld current 850 A was shown in Figure 4.66. It indicates that the percentage elongation of weldments with defects is greater than that of weldments without defects. Weld defects such as lack of penetration will decrease the effective area supporting the applied force. Thus, the stress of the weld metal at weld defects locations will be greater than at other places since the applied force is the same for the whole weldment during tensile testing. From the stress-strain curves, it can be seen that a higher stress will cause greater strain, which means higher plastic deformation or elongation if the strength is beyond the yield strength of the weld metal. Therefore, the weld elongation of weldments with defect is greater than that of weldments without defects.

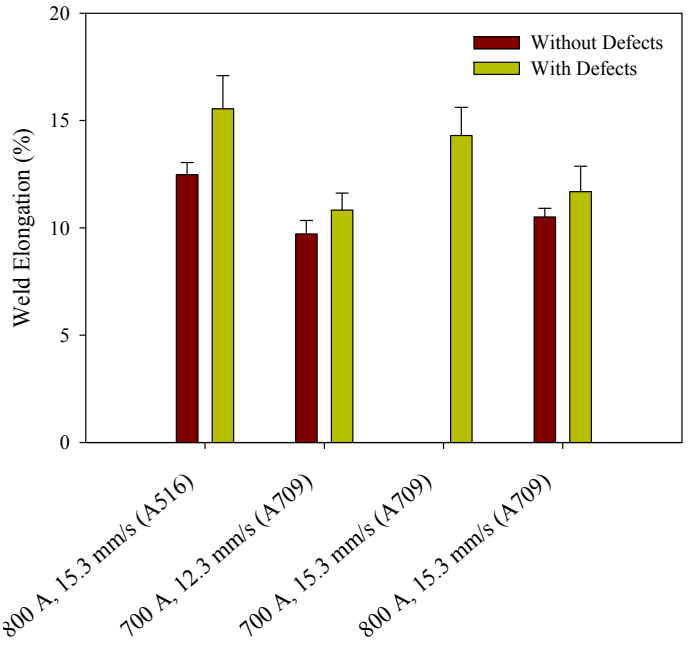

Figure 4.66. Effect of weld defects on weld elongation of weldments.

4.4.4 Charpy Impact Toughness

Charpy V-notch impact testing was carried out to investigate the effect of SAW parameters on the impact toughness of the parent metals, weld metals, and heat affected zones of SA516 and A709 steels. The following sub-sections are divided into the toughness results of SA516 and A709 weldments.

4.4.4.1 Toughness of SA516 Weldments

Figures 4.67 and 4.68 show the transition temperature curves obtained for PM, WM and HAZ of SA516 using different SAW variables. Figure 4.6 shows that the toughness of the WM produced using 700 A and 5.9 mm/s is the lowest, while that of HAZ is the highest. It can also be seen in Figure 4.68 that all the weld metals produced using 800 A have lower toughness than the PM. This behaviour is due to the different microstructures

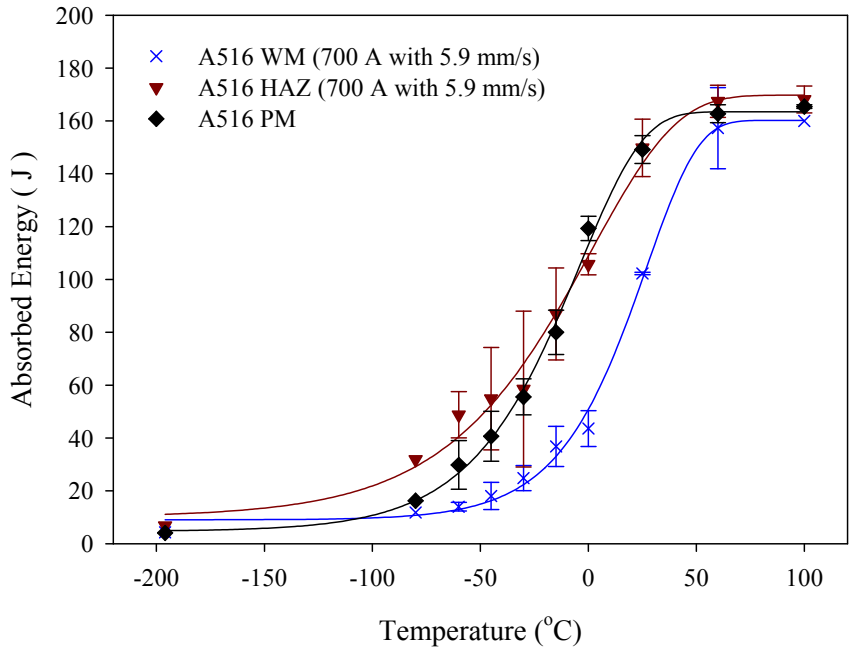

Figure 4.65. Comparison of transition temperature curves for the PM, WM and HAZ of SA516 produced using 700 A and 5.9 mm/s.

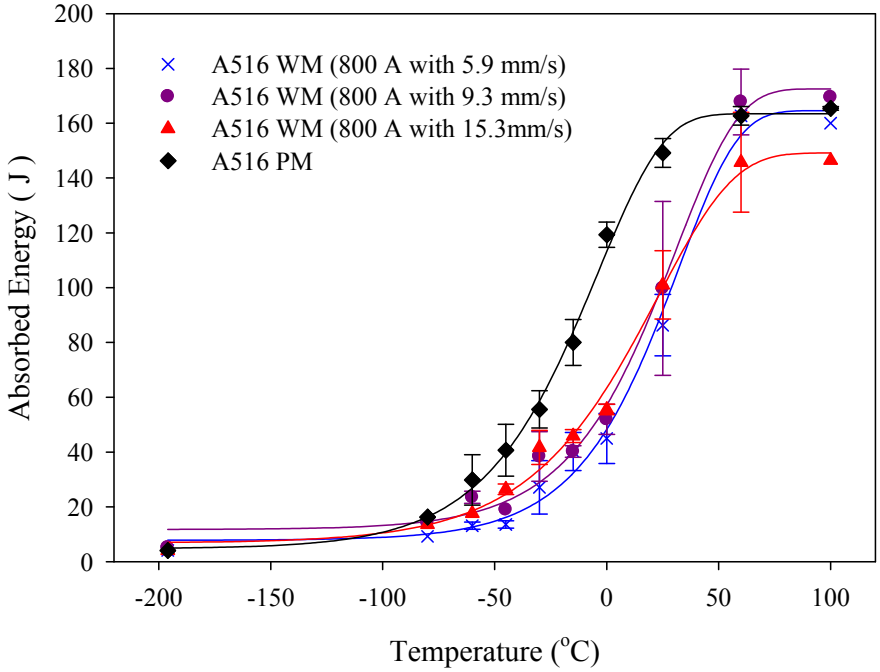

Figure 4.66. Comparison of transition temperature curves of the PM and WM of SA516 produced using 800 A.

that developed in the weld metal and parent metal. As mentioned in section 4.4.1, the microstructures of the parent metal consists of ferrite and pealite (see Figure 4.46). The weld metal has coarse columnar grain microstructure (see Figure 4.47) which consists of acicular ferrite and polygonal grain boundary ferrite (PGBF). From these figures it can be seen the grain size of the weld metal is far greater than that of the parent metal. Thus, crack direction cannot be effectively changed when a crack propagates in the weld metal during Charpy impact testing. In the contrary, crack propagation in the parent metal is not easy because so many grain boundaries contained therein can effectively inhibit crack propagation. In order to break the Charpy test specimen, more energy needs to be consumed when crack propagates in the parent metal. Therefore, the toughness of the parent metal is higher than that of the weld metal. At the same time, the results from Vickers hardness measurements show that the weld metal has higher hardness than the parent metal. Generally, high hardness means low toughness except when the high hardness comes from small grain size. On this basis, it can be said that the results from Charpy impact testing are consistent with those of the hardness measurements.

Figure 4.69 shows the lateral expansion curves for the WM of SA516 produced using 800 A and PM of SA516. Comparing Figures 4.68 and 4.69, it can be seen that both plots show practically the same trend. For a given material, the more plastic deformation produced, the higher the absorbed energy consumed. Lateral expansion is an indication of the plastic deformation undergone by the test sample. Thus, the higher the absorbed energy consumed by Charpy impact specimens, the higher the lateral expansion obtained. Thus, lateral expansion can also used as an indication of toughness. Therefore, the ductile-brittle transition temperatures can also be obtained from lateral expansion curves.

Figure 4.68 also shows that the toughness of the WM increases with increasing travel speed for a given welding current. Although the weld metals consist mainly of acicular ferrite and PGBF, their grain sizes are quite different due to the different cooling rates undergone by each sample. Figures 4.68-4.70 show the microstructures of the weld metals of SA516 produced using 5.9 mm/s, 9.3 mm/s and 15.3 mm/s, respectively. Comparing these figures, it can be seen that large grains (seen in Figure 4.70) were

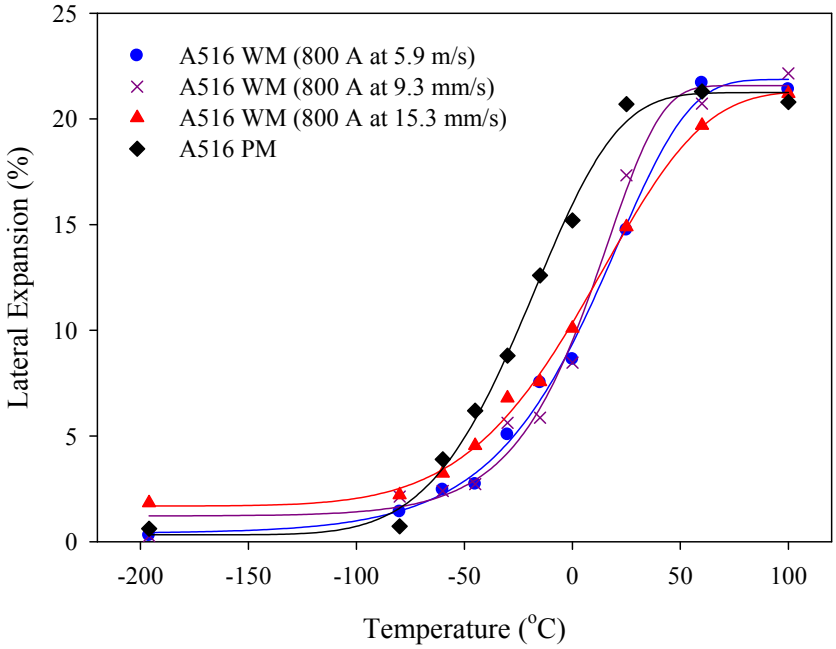

Figure 4.69. Comparison of lateral expansion curves at different temperatures for the PM and WM of SA516 produced using 800 A.

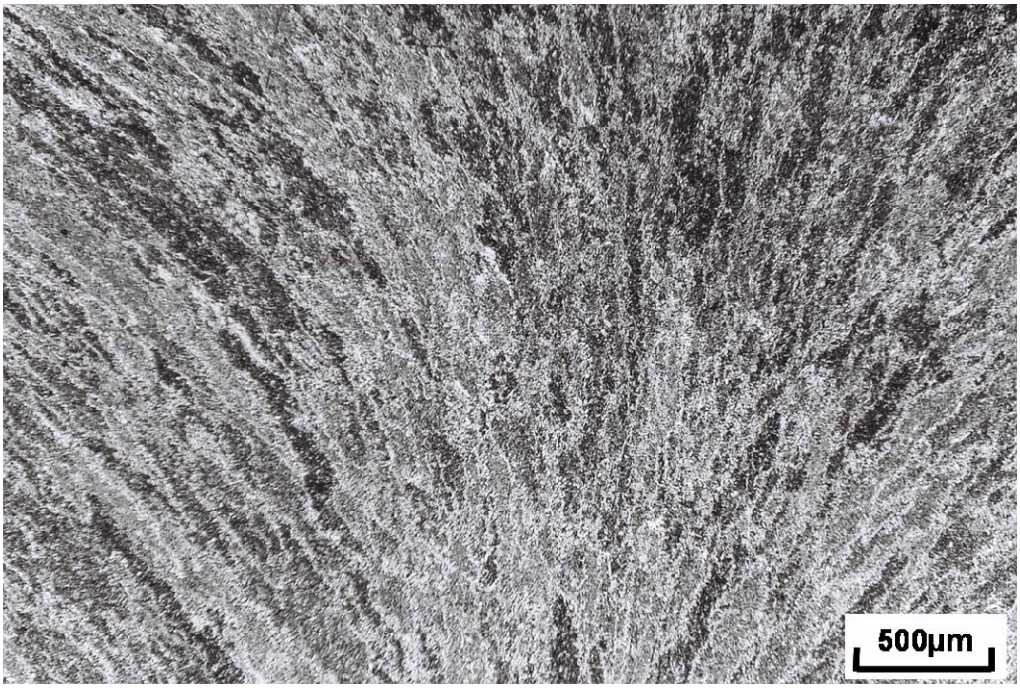

Figure 4.70. A typical optical micrograph of the weld metal of SA516 weldments produced using 800 A and 5.9 mm/s.

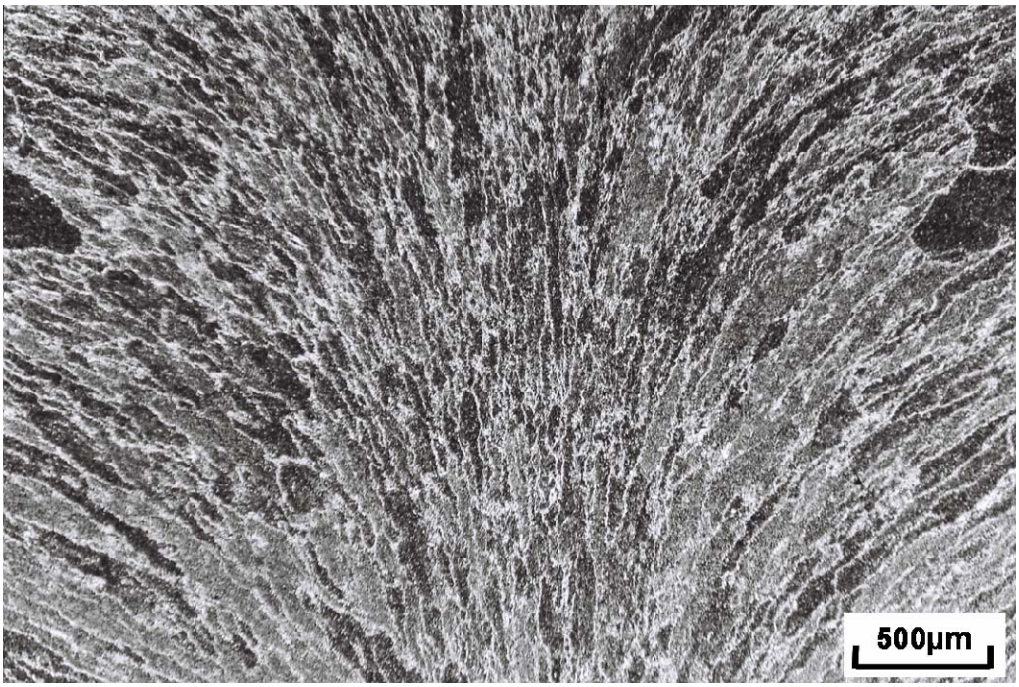

Figure 4.71. A typical optical micrograph of the weld metal of SA516 weldments produced using 800 A and 9.3 mm/s.

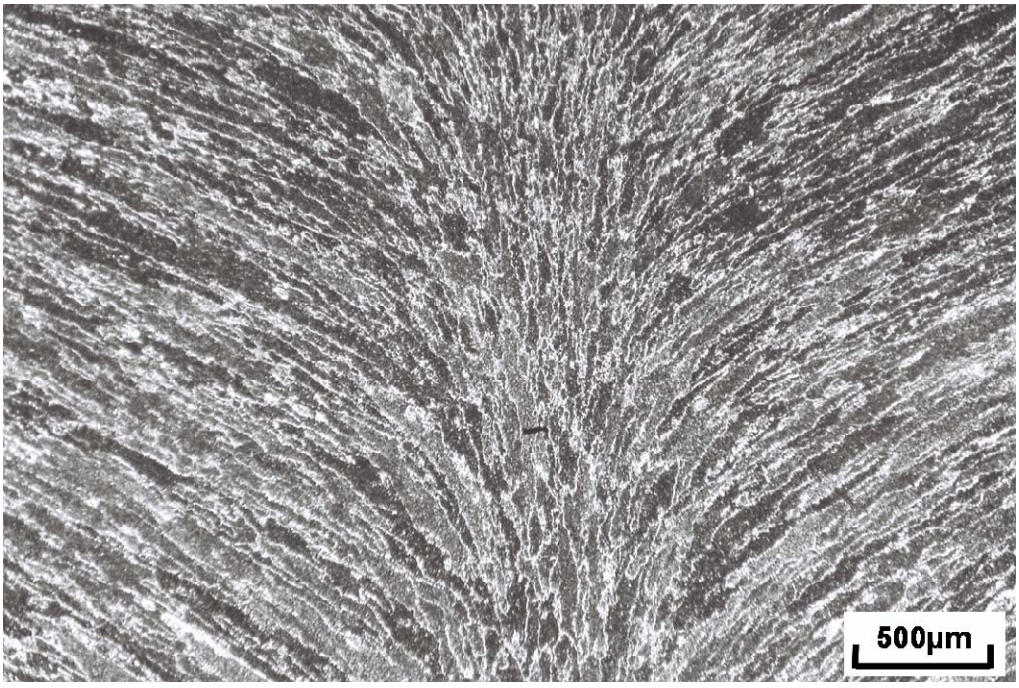

Figure 4.72. A typical optical micrograph of the weld metal of SA516 weldments produced using 800 A and 15.3 mm/s.

obtained in the weld metal that was produced using the lowest travel speed, while small grains were obtained in the weld metal produced using the highest travel speed. The small grain size results in good toughness. Therefore, the toughness of the WM increased with increasing travel speed.

Figure 4.73 shows the transition temperature curves of the PM and HAZ of SA516 produced using 850 A. It can be seen that the toughness of the HAZ is greater than that of the PM. The standard deviation of the absorbed energy in the HAZ is greater than that of the PM too. This behaviour may be related to the location of the notch of the Charpy impact specimens. As shown in Figure 4.74, the notch of the HAZ specimens was cut in such a manner as to include as much HAZ as possible. Due to the shape of the HAZ, the HAZ notch crosses the CGHAZ and FGHAZ. If the size of the HAZ is very small, there is a great possibility that the HAZ notch will cross the PM region too. The fraction of each zone depends on the size of the HAZ. Therefore, the toughness of the HAZ is a combination of the toughness of CGHAZ, FGHAZ and PM.

As shown in section 4.4.1, the hardness of the weld interface or CGHAZ is the highest in all the weld zones studied, while the parent metal has the lowest hardness. Hardness can give an indication of strength and toughness. As shown in Figure 4.74, the notched part of the CGHAZ is very small compared with the FGHAZ because it is located close to weld interface. The fraction of the CGHAZ in the notch decreases with increasing travel speed since the HAZ size also decreases appreciably with increasing travel speed. Compared to the parent metal, the FGHAZ has a better toughness because the fine grain microstructures effectively resist propagation of crack and change the direction of crack travel resulting in large absorbed energy consumption during fracture. As the fraction of the FGHAZ is large, the toughness of the HAZ is greater than that of the PM.

Another way to determine Charpy impact toughness is to measure the transition temperature when the average absorbed energy of three Charpy-V notch specimens is 27 J (T_{27J}) [63]. The lower the 27 J transition temperature, the greater is the toughness of specimen at low temperature. Figure 4.75 shows the Charpy V-notch 27 J transition

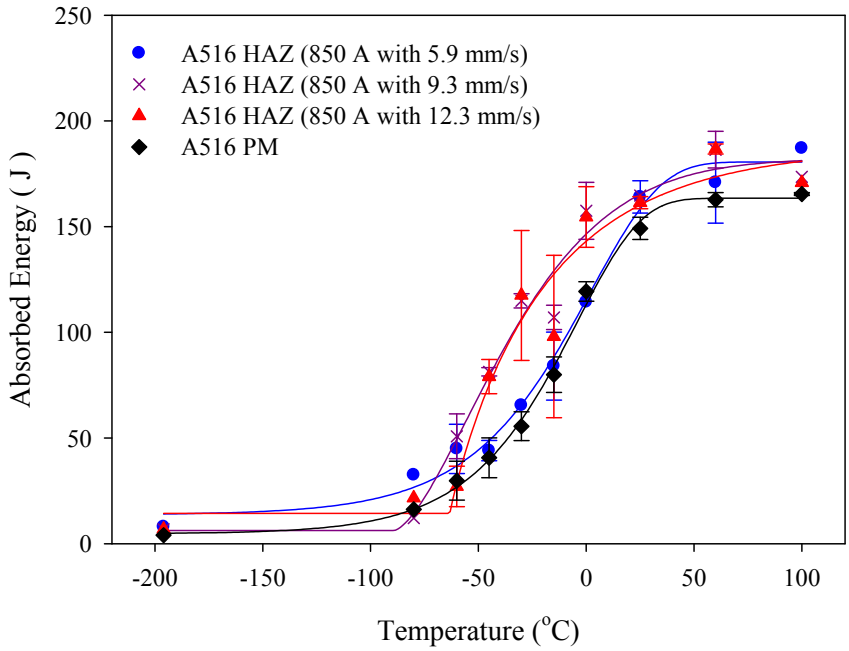

Figure 4.73. Comparison of transition temperature curves for the PM and HAZ of SA516 produced using 850 A.

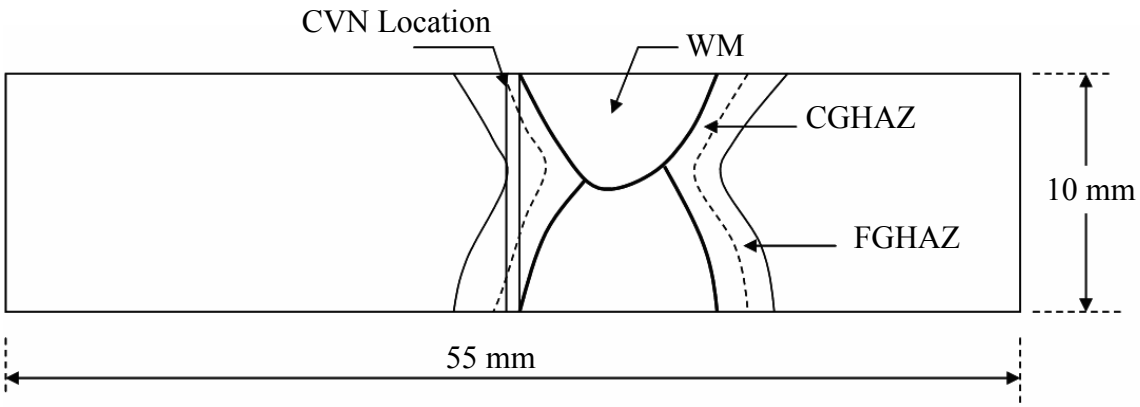

Figure 4.74. HAZ notch location in Charpy V-notch (CVN) impact specimen.

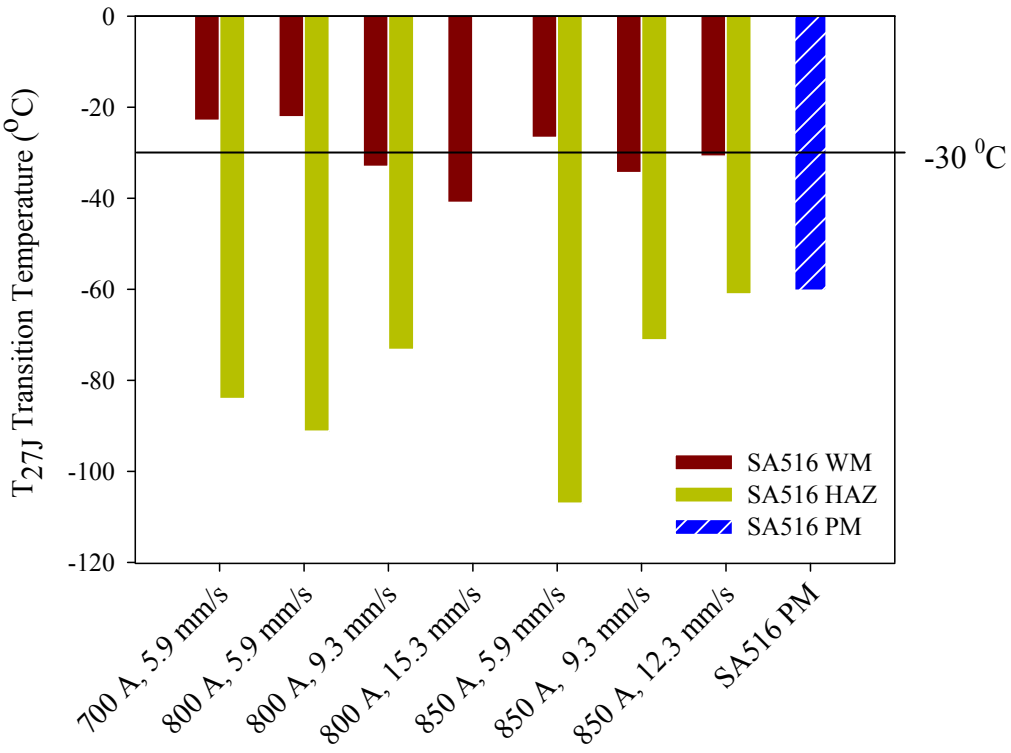

Figure 4.75. Charpy impact transition temperature T_{27J} for WM, HAZ and PM of SA516.

temperature for WM, HAZ and PM of SA516. From this figure, it can be seen that the HAZ has the lowest 27 J transition temperature, while the weld metal has the highest 27 J transition temperature. The transition temperatures of the WM produced using 5.9 mm/s are -22.8 ^{o}C for 700 A, -22.1 ^{o}C for 800 A and -26.7 ^{o}C for 850 A. According to the ASME Boiler and Pressure Vessel Code [63], average of three Charpy specimens impact absorbed energy shall be no less than 27 J at -30 ^{o}C. Since the weldments produced using 5.9 mm/s have higher 27 J transition temperature than -30 ^{o}C, therefore, they are not suitable for use in fabricating a pressure vessel.

The 50% Ductile to Brittle Transition Temperature (DBTT) of all WM, HAZ and PM of SA516 are shown in Figure 4.76. It can be seen that the transition temperatures of weld metal are greater than 0 ^{o}C. This can be attributed to the columnar microstructures that resulted in low toughness properties. The HAZ and PM have DBTTs which are below 0 ^{o}C due to their high toughness.

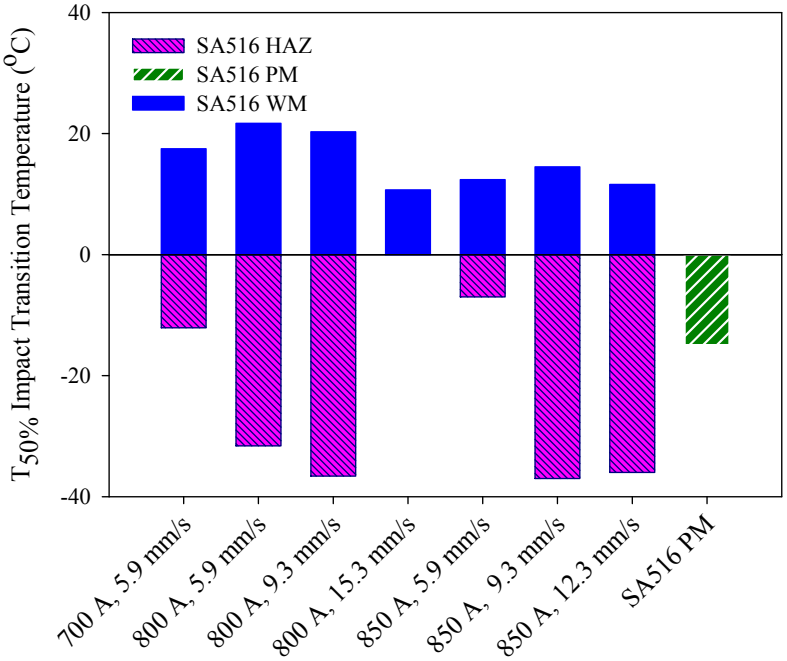

Figure 4.76. Charpy impact transition temperature, $T_{50\%}$, for the WM, HAZ and PM of SA516.

Figure 4.77 shows that the absorbed energy of the WM of SA516 decreased with increasing the HAZ size. The reason for this behaviour is the HAZ size increased with heat input. The grain size of the WM increases with increasing input. Therefore, high heat input reduces the toughness of the weld metal.

Figure 4.78 shows typical SEM fractographs of Charpy impact fracture surfaces of the PM, WM and HAZ regions of SA516 for different welding parameters at -196 ^{o}C. All these images show typical brittle fracture surfaces with cleavage features. It is clear that all samples are brittle at -196 ^{o}C. Figure 4.78(c) shows that the HAZ has more barrier to crack propagation because of the fine microstructures in the FGHAZ. Figures 4.78(b) and 4.78(d) show that it is easy for the crack to propagate in the weld metals because of the coarse columnar grain structures in the weld metal. Therefore, the toughness of the weld metal is lower than that of the PM and HAZ at very low temperatures.

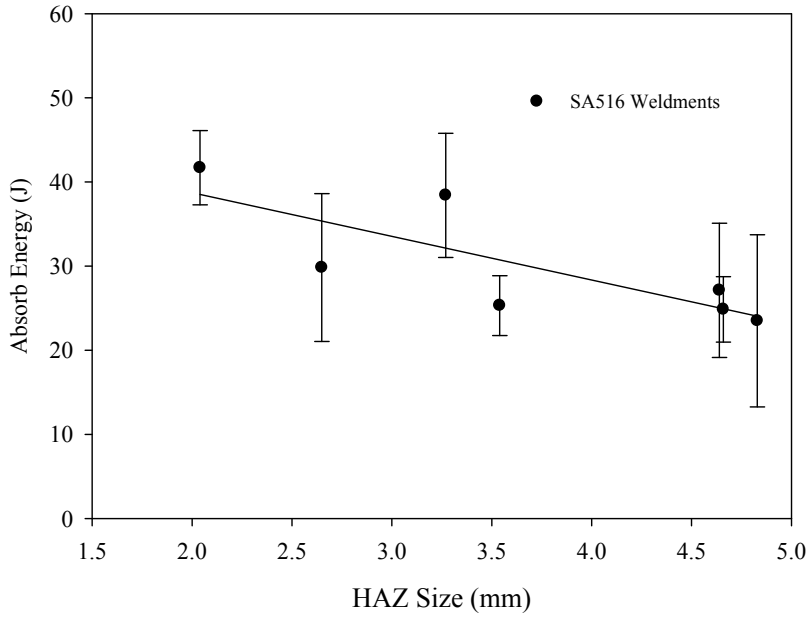

Figure 4.77. Variation of absorbed energy with HAZ size for SA516 WM at -30 ^{o}C.

Figure 4.79 shows typical SEM fractographs of Charpy impact fracture surfaces of PM, WM and HAZ for SA516 at different test temperatures. Ductile (dimples) and brittle (cleavage) features can be seen in these pictures. Figures 4.79(b) and 4.79(d) show that roughly 50% area of the picture has ductile features with dimples and 50% area has brittle features.

Figure 4.80 shows typical SEM fractographs of Charpy impact fracture surfaces of PM, WM and HAZ for SA516 at 60 ^{o}C and 100 ^{o}C. All these fractographs show 100% ductile features with dimples in all images. From these images it can be seen that the size of the dimples in the HAZ is greater than in other zones. The ductile fracture, in the form of void coalescence, initiate at fine second phase particles. The mechanism involves the nucleation, growth and linking of voids in the plastic zone ahead of the crack tip, thus propagating the fracture. In contrast to the PM and HAZ, the ductile failure by void coalescence in the WM is initiated at inclusions that provide nucleating sites for the voids (see Figure 4.81).

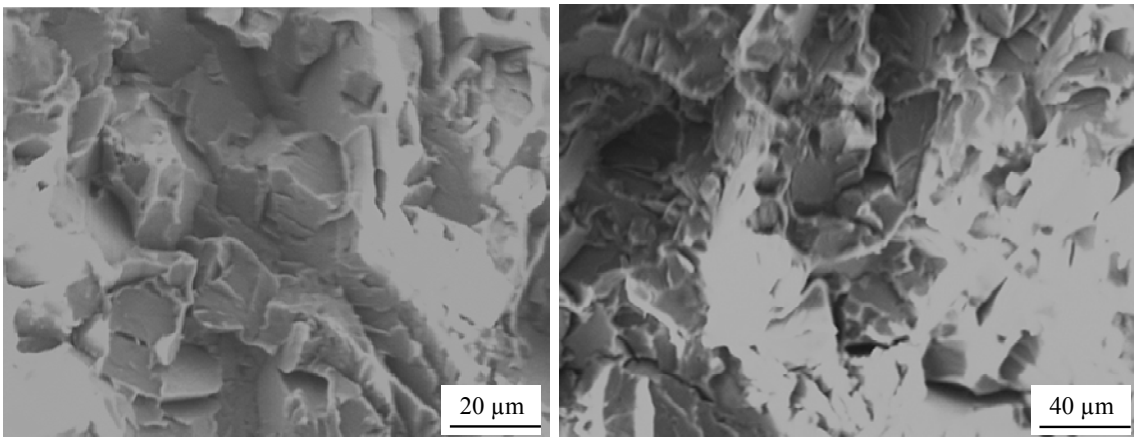

(a) (b)

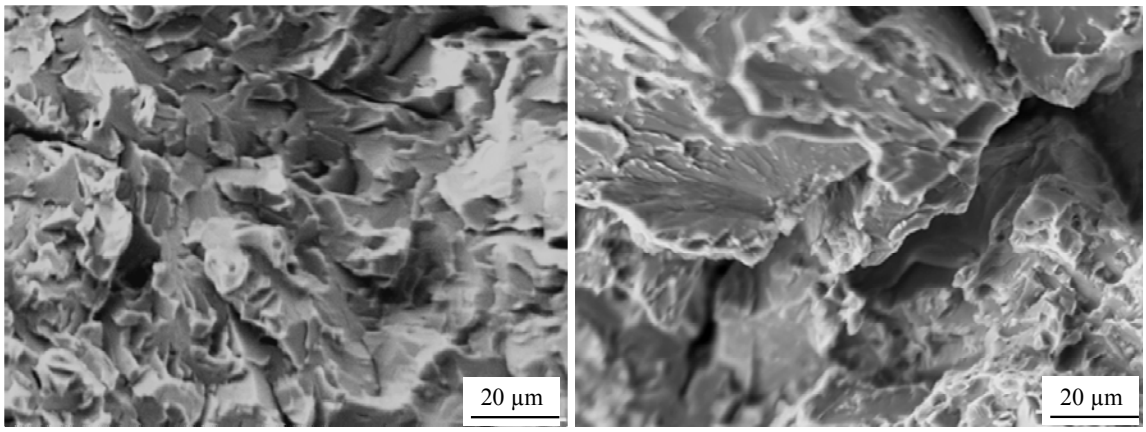

(c) (d)

Figure 4.78. Typical SEM micrographs of Charpy impact fracture surfaces for WM, HAZ and PM of SA516 (-196 ^{o}C). (a) PM, (b) WM produced using 800 A and 5.9 mm/s, (c) HAZ produced using 800 A and 5.9 mm/s, and (d) WM produced using 850 A and 9.3 mm/s.

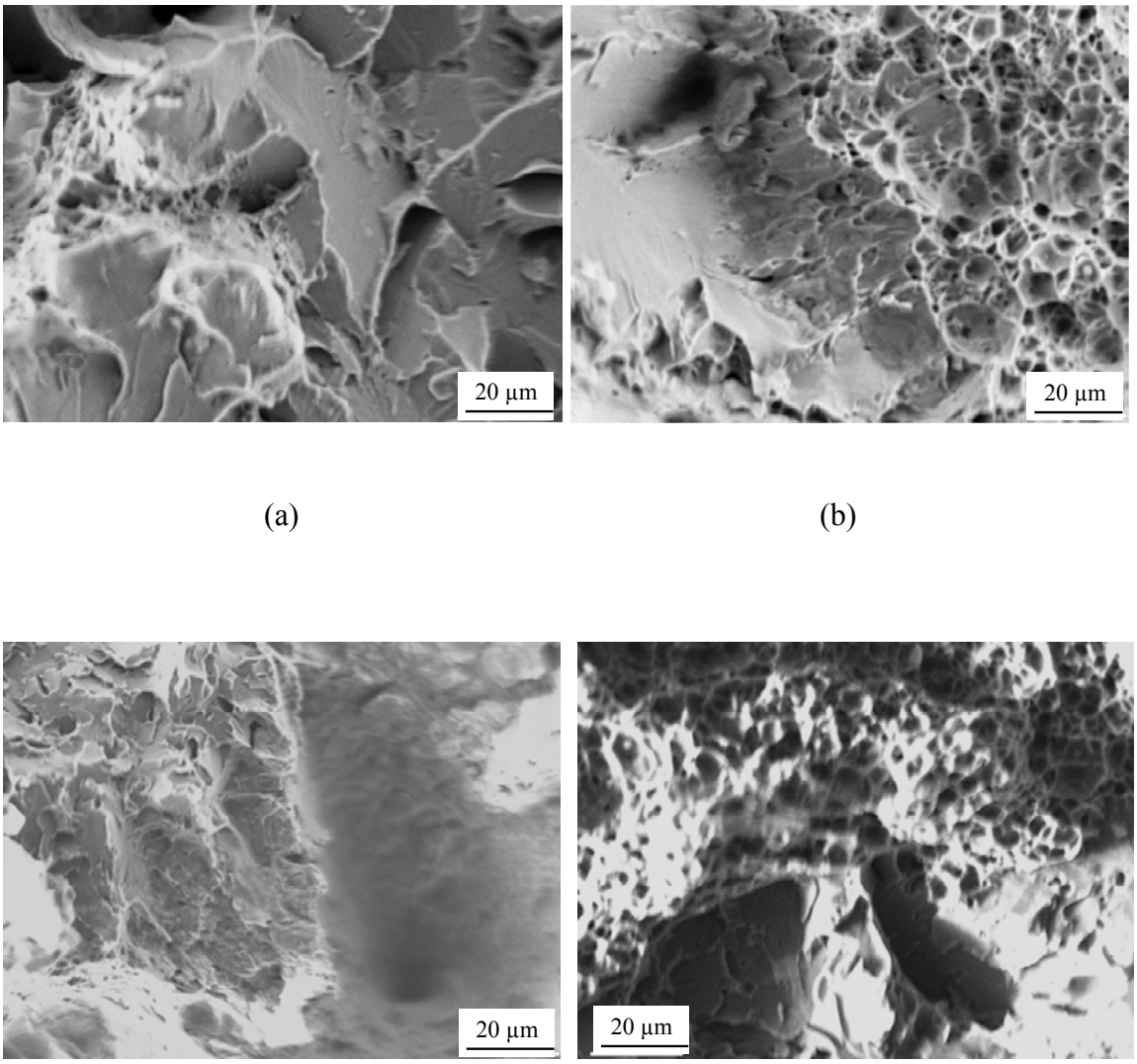

Figure 4.79. Typical SEM micrographs of Charpy impact fracture surface for WM, HAZ and PM of SA516 at different transition tempertures. (a) PM (-15 ^{o}C), (b) WM produced using 800 A and 5.9 mm/s (25 ^{o}C), (c) HAZ produced using 800 A and 5.9 mm/s (-30 ^{o}C), and (d) WM produced using 850 A and 9.3 mm/s (0 ^{o}C).

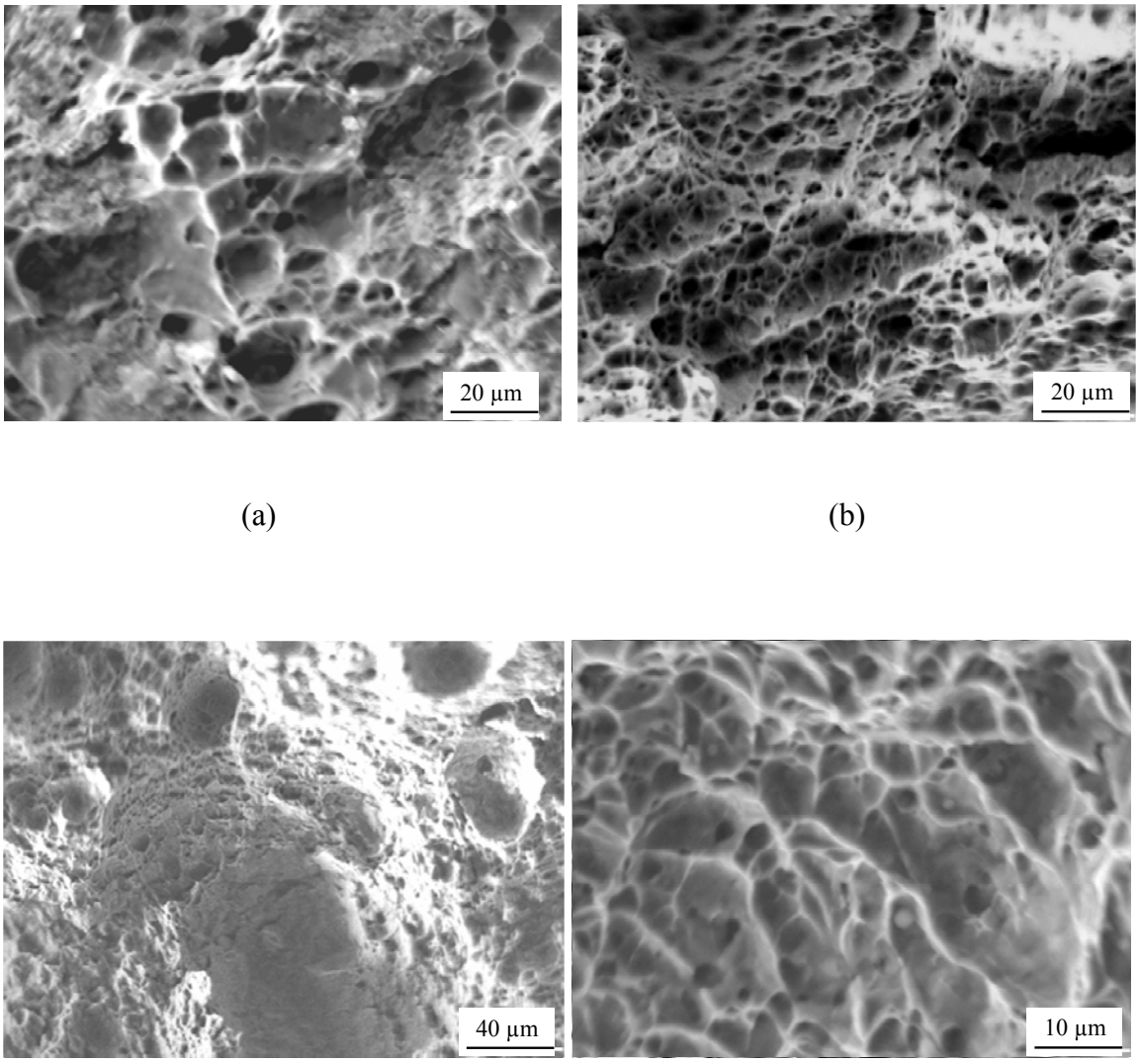

Figure 4.80. Typical Charpy impact ductile fracture surface images for WM, HAZ and PM of SA516. (a) PM (100 ^{o}C), (b) WM produced using 800 A and 5.9 mm/s (100 ^{o}C), (c) HAZ produced using 850 A and 9.3 mm/s (60 ^{o}C), and (d) WM produced using 850 A and 9.3 mm/s (60 ^{o}C).

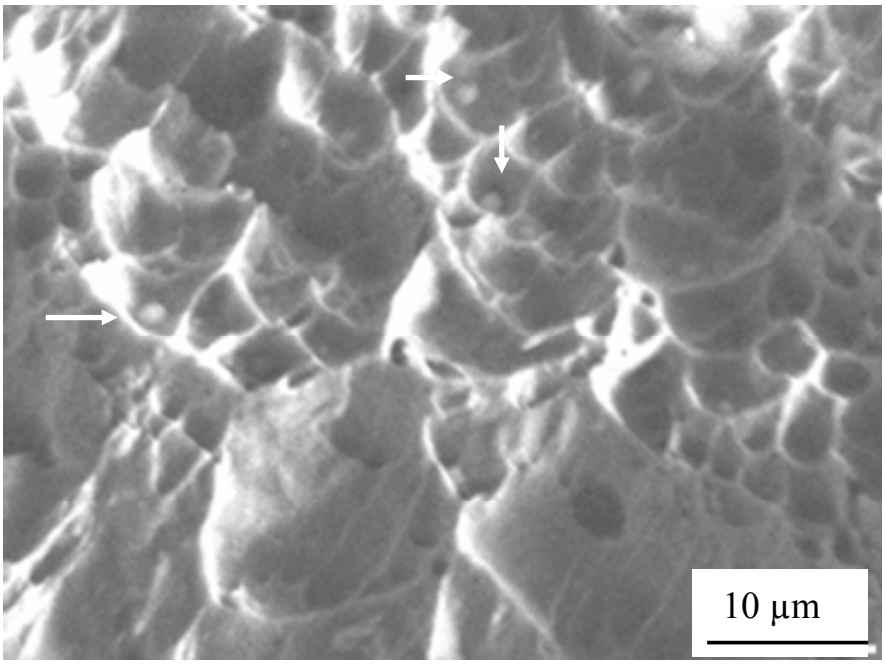

(a)

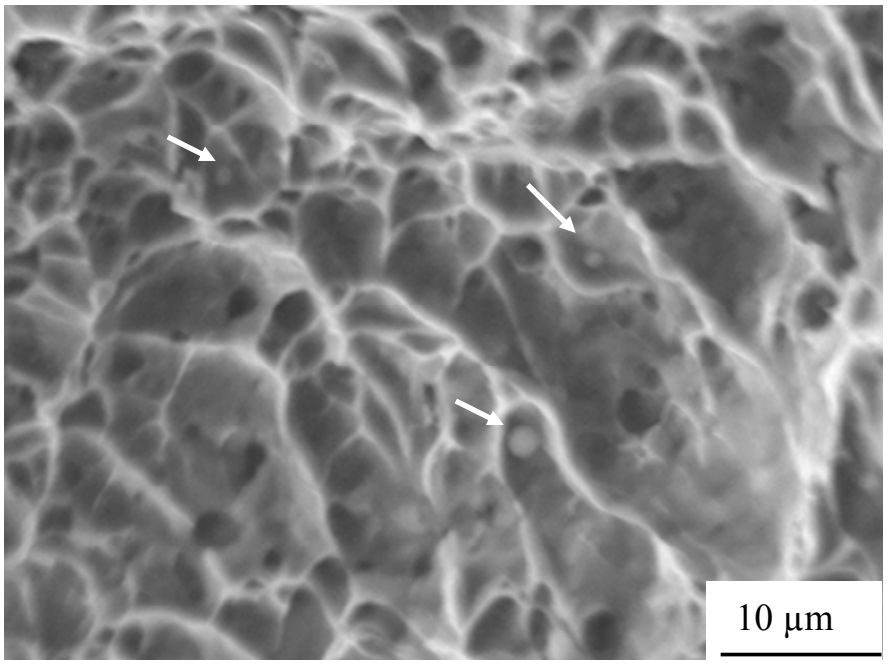

(b)

Figure 4.81. Typical SEM micrographs showing particles in the WM of SA516. (a) WM produced using 800 A and 5.9 mm/s (100 ^{o}C) and (b) WM produced using 850 A and 9.3 mm/s (60 ^{o}C).

4.4.4.2 Toughness of A709 Weldments

Figure 4.82 shows the impact toughness of the WM of A709 produced using a welding current of 850 A and different travel speeds. It can be seen that the toughness of the weld metal produced using 5.9 mm/s is less than that of the other speeds. I can be also seen that the toughness of the WM increases with increasing travel speed. High travel speed results in fine microstructures in the weld metal because of rapid cooling rate. The fine grain size contributes to the good toughness of the weld metal. Figures 4.83-4.86 show the microstructures of weld metals produced using 850 A and different travel speeds. These figures show that the grain size of ferrite decreases substantially with increasing travel speed.

Figure 4.87 shows the Charpy V-notch 27 J transition temperature (T_{27J}) for the WM and PM of A709. The 27 J transition temperatures of the WM produced using 5.9 mm/s are -27.2 ^{o}C for 700 A, -24.8 ^{o}C for 800 A and -26.5 ^{o}C for 850 A. The PM and other weld metals have lower transition temperature than -30 ^{o}C. Figures 4.83, 4.88 and 4.89 show the microstructures of the WM produced using 5.9 mm/s and different welding currents. It can be seen that coarse columnar grains are the main feature of the microstructures in weld metals. As mentioned in section 4.4.4.1, it is only if the 27 J transition temperature of the weld metal is lower than -30 ^{o}C that it can meet the requirements for the acceptance criteria. Thus, all the weld metals produced using a travel speed of 5.9 mm/s did not meet the requirements. Therefore, welds produced this speed are not suitable for fabricating wind turbine towers.

The 50% brittle and 50% ductile transition temperature ($T_{50\%}$) for the PM and WM of A709 are shown in Figure 4.90. It can be seen that the $T_{50\%}$ of weld metals produced using 5.9 mm/s are above 0 ^{o}C, while others are below 0 ^{o}C. This again shows that a travel speed of 5.9 mm/s resulted in the lowest toughness of the weld metal for all welding currents.

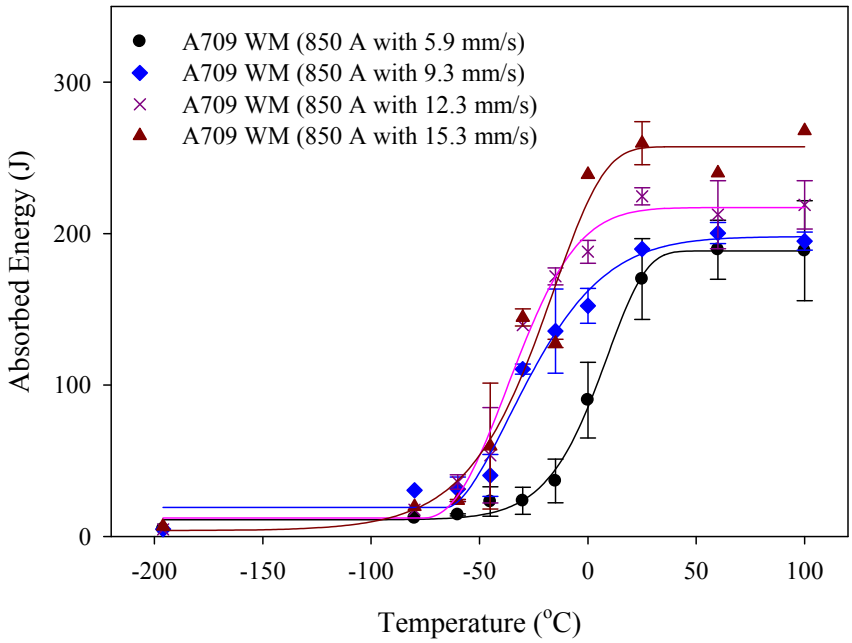

Figure 4.82. Comparison of impact toughness of the weld metal of A709 steel produced using 850 A.

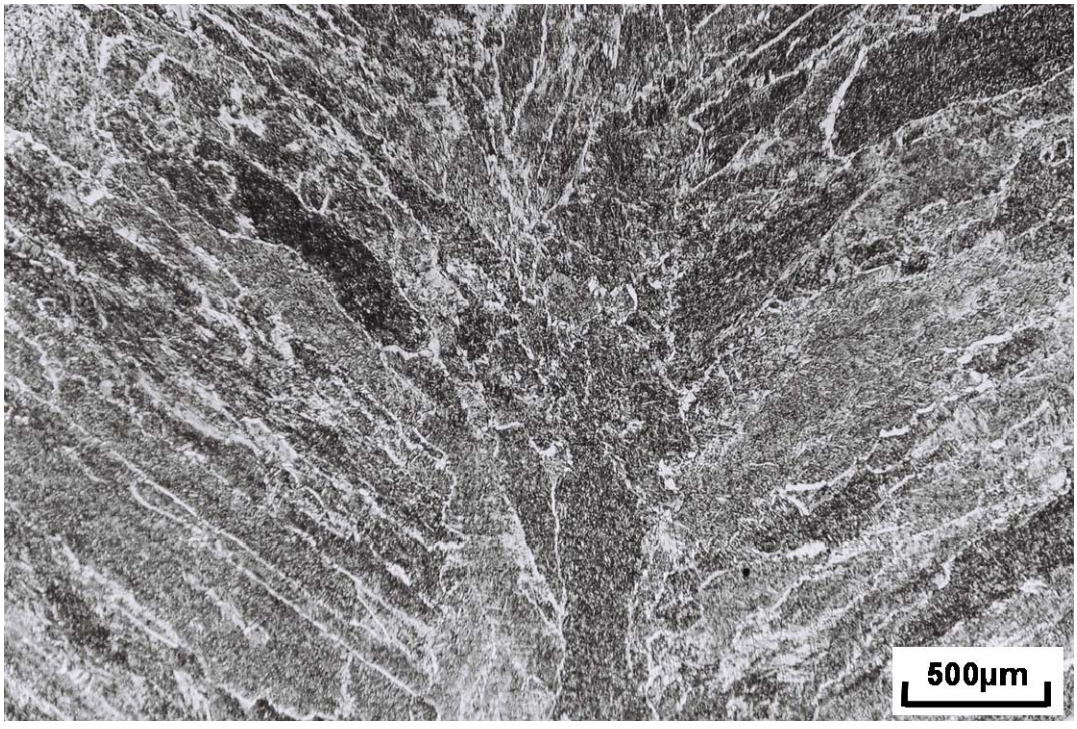

Figure 4.83. A typical optical micrograph of the weld metal of A709 steel produced using 850 A and 5.9 mm/s.

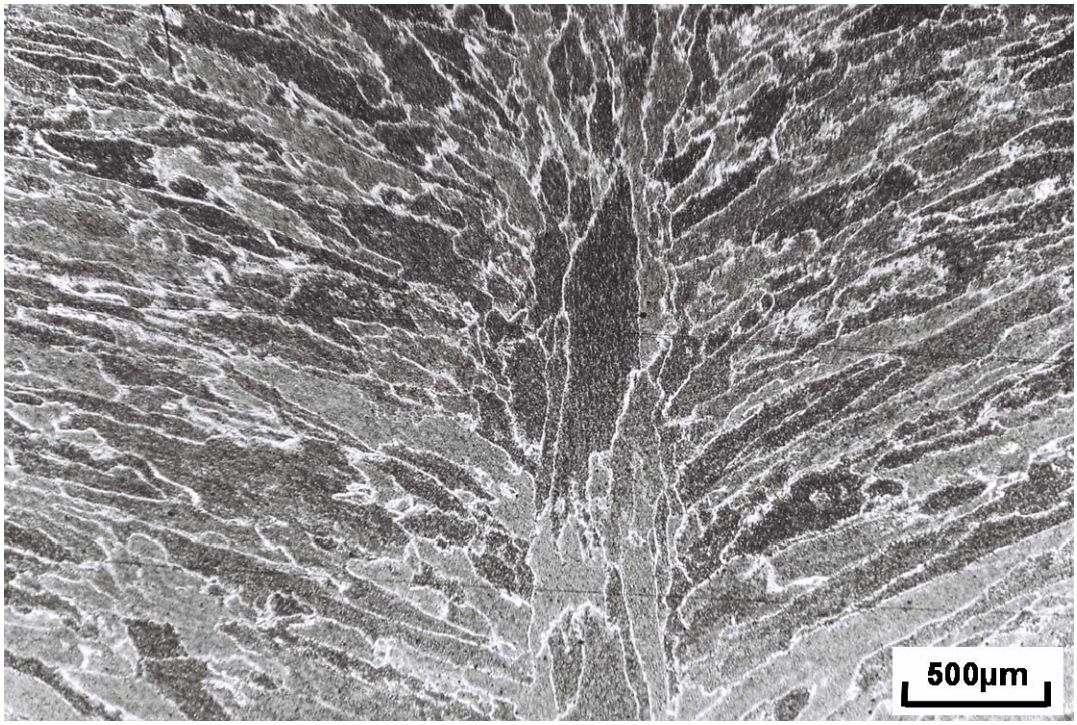

Figure 4.84. A typical optical micrograph of the weld metal of A709 steel produced using 850 A and 9.3 mm/s.

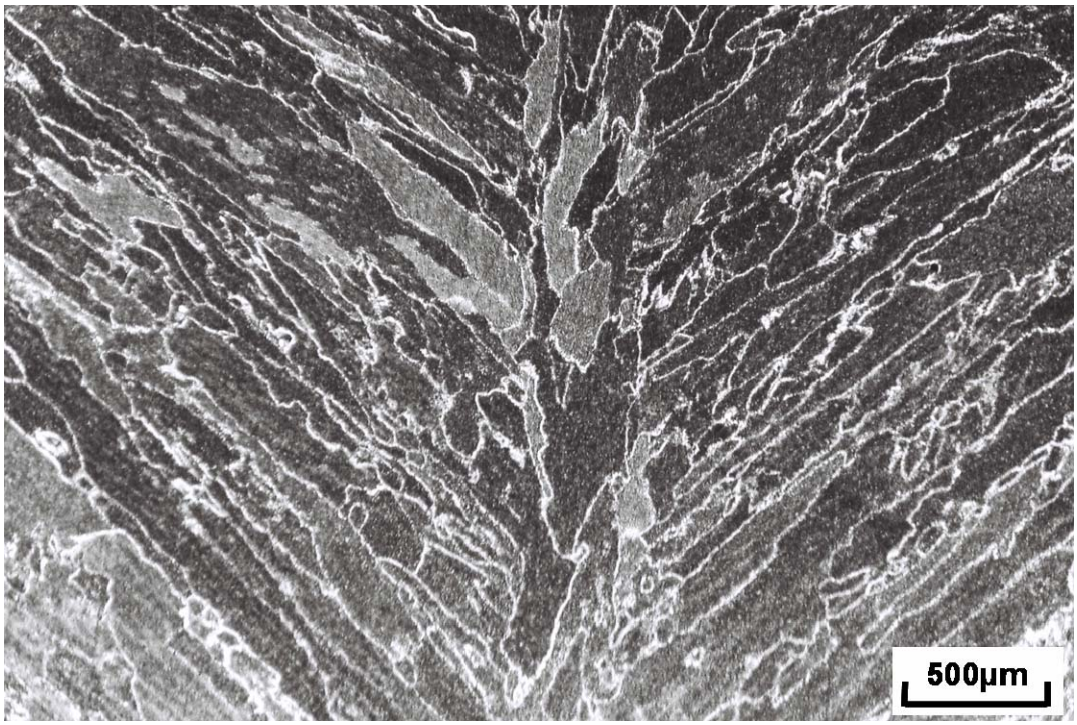

Figure 4.85. A typical optical micrograph of the weld metal of A709 steel produced using 850 A and 12.3 mm/s.

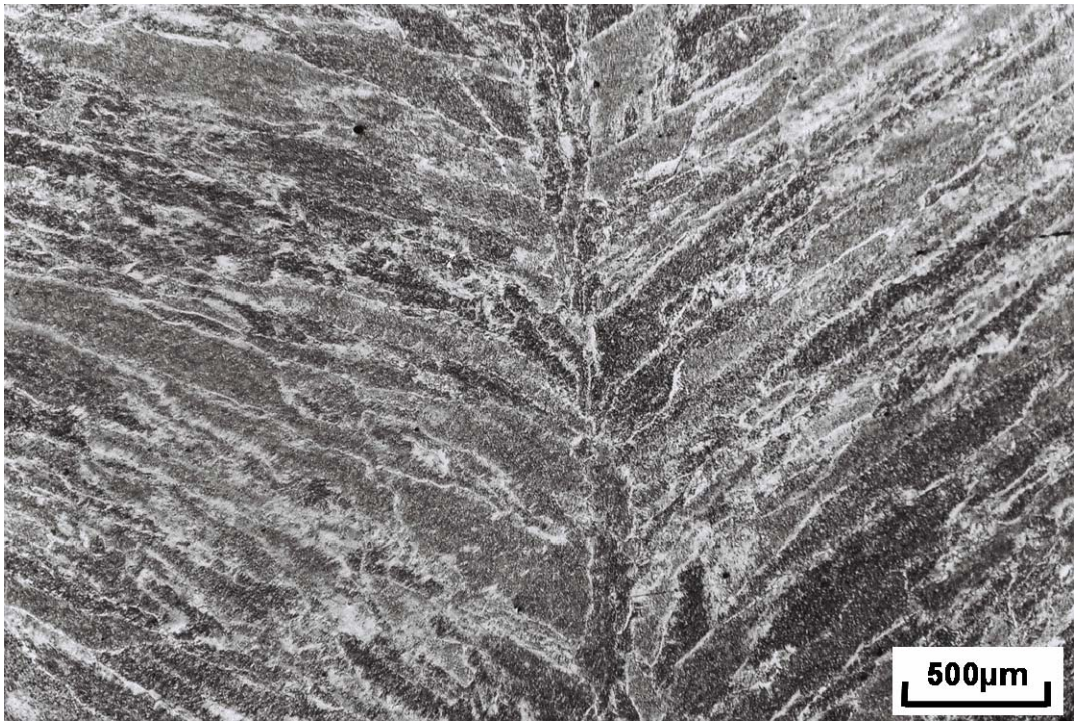

Figure 4.86. A typical optical micrograph of the weld metal of A709 steel produced using 850 A and 15.3 mm/s.

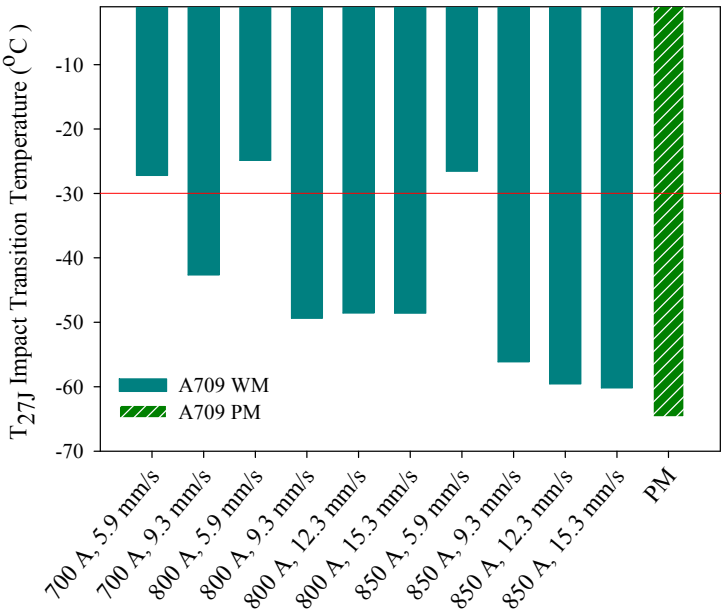

Figure 4.87. Charpy impact transition temperature $T_{27\ J}$ for WM and PM of A709 as a function of welding parameters.

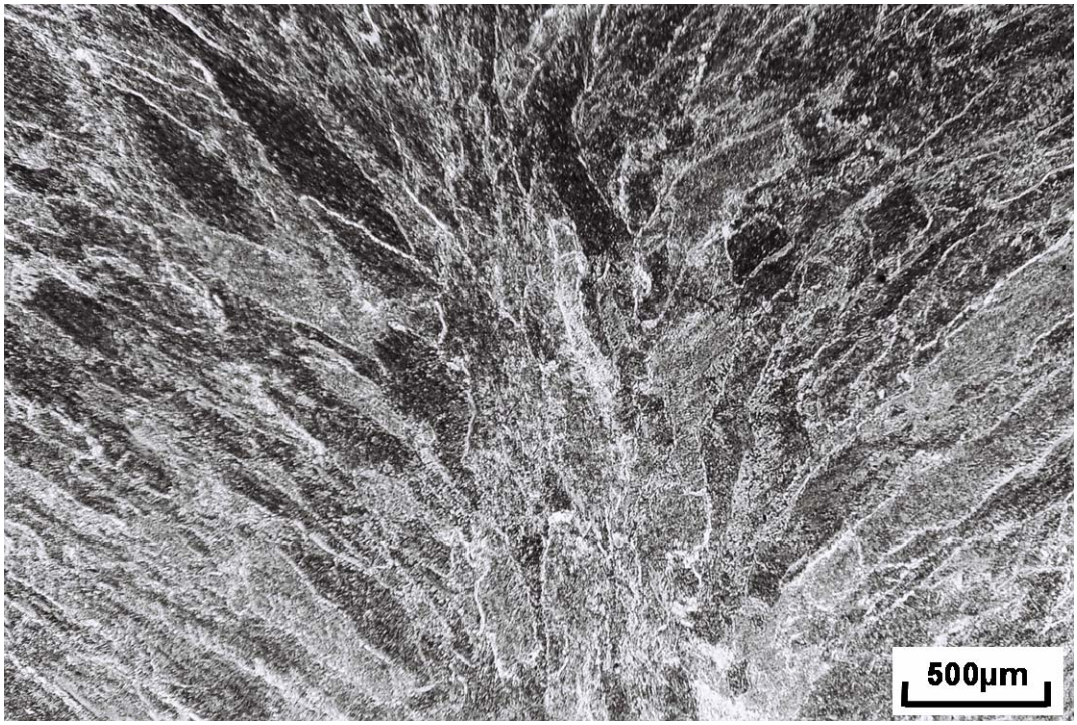

Figure 4.88. A typical optical micrograph of the weld metal of A709 steel produced using 700 A and 5.9 mm/s.

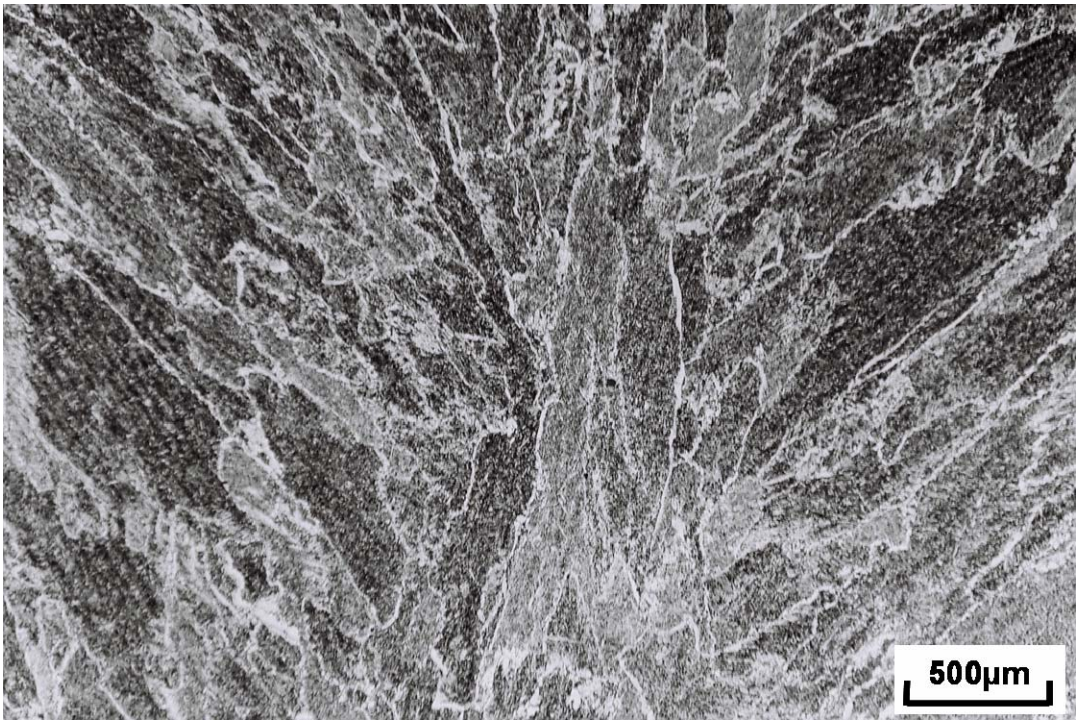

Figure 4.89. A typical optical micrograph of the weld metal of A709 steel produced using 800 A and 5.9 mm.

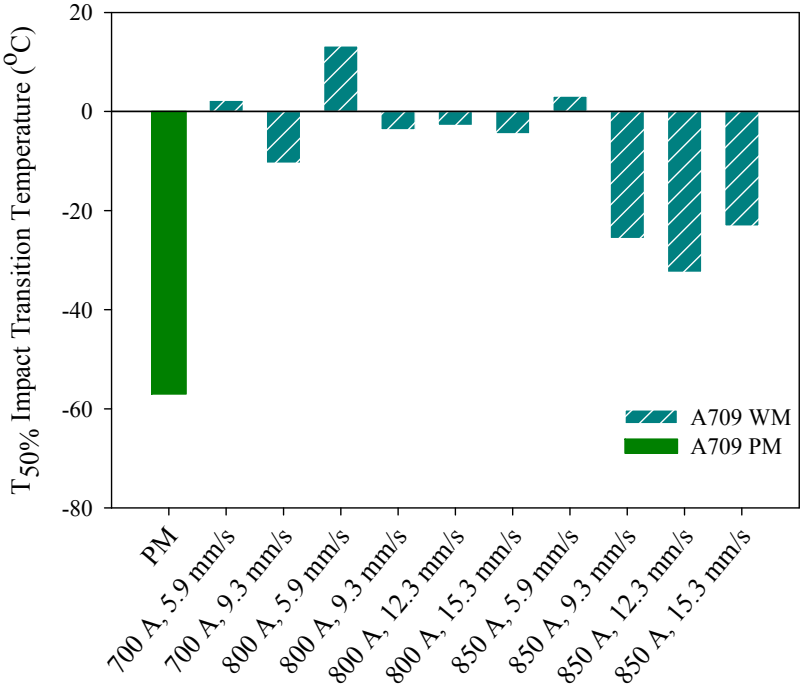

Figure 4.90. Variation of impact transition temperature $T_{50\%}$ of the WM and PM of A709 steel with .

The relationship between the absorbed energy and HAZ size of A709 weldments is shown in Figure 4.91. The result is the similar to that of the WM of SA516 (See Figure 4.77). The toughness of the weld metal decreased with increasing HAZ size. The more the heat input used in the SAW process, the greater the HAZ size generated in the weldments. Although productivity can be increased with increasing heat input, the toughness of the weldment will decrease with it.

The Charpy impact test results show that the HAZ and PM of A709 have high toughness. Although the Charpy impact test machine (Roell Amsler PSW 750) at IPSCO Inc. has a capacity of 750 J, the impact test specimens of the HAZ and PM of A709 could not totally shear off for temperatures higher than -30 ^{o}C. Therefore, the total transition temperature curves could not be plotted because only a few effective data were obtained from the experiment. Figure 4.92 shows photographs of fractured test specimens of the

PM and HAZ of A709. The high toughness of the PM results from the very low carbon content and minor alloying elements such as Nb, V and Ti, which can significantly improve the low-temperature toughness of the alloy. The very fine microstructure in the FGHAZ (see Figure 4.56) of A709 causes the toughness of HAZ to be even better than that of the PM.

Table 4.9 shows the Charpy impact test results for the HAZ and PM of A709. It can be seen from the table that high average absorbed energy is obtained even at -60 ^{o}C. For example, the impact energy of the HAZ produced using 800A and 5.9mm/s is as high as 403 J at -60 ^{o}C.

Figure 4.91 shows typical SEM fractographs of Charpy impact fracture surfaces of the PM and WM for A709 at -196 ^{o}C. All these images show similar features of brittle fracture surface with cleavage features, which is similar to those of SA516 (see figures 4.78). Figure 4.94 shows the SEM fractographs of the WM of A709 at different transition temperatures. Ductile and brittle features can be observed in these images. Inclusions were also found in the weld metals of A709 as shown in Figure 4.95.

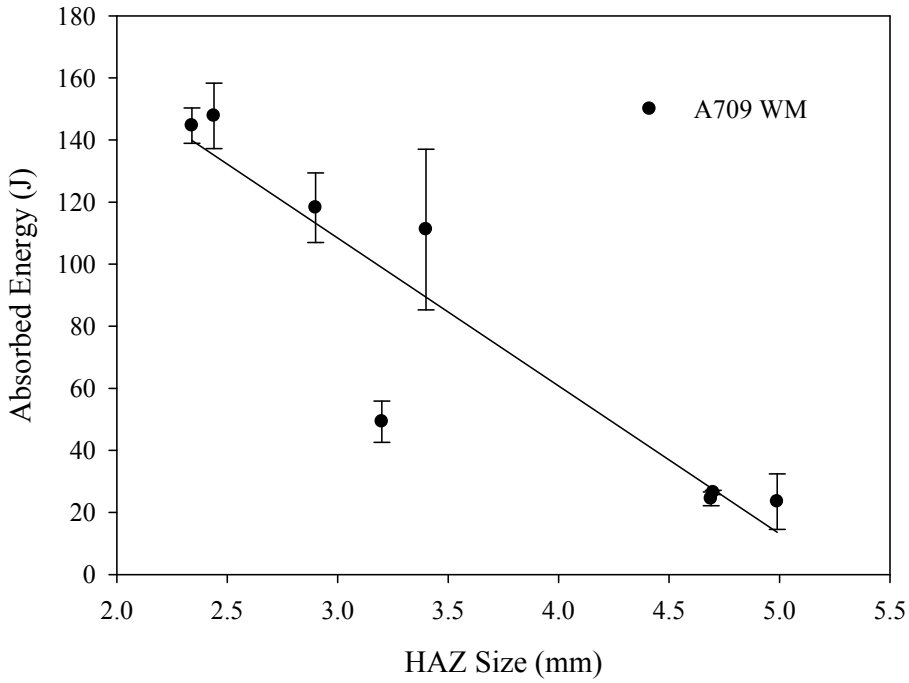

Figure 4.91. Variation of absorbed energy with HAZ size for A709 WM at -30 ^{o}C.

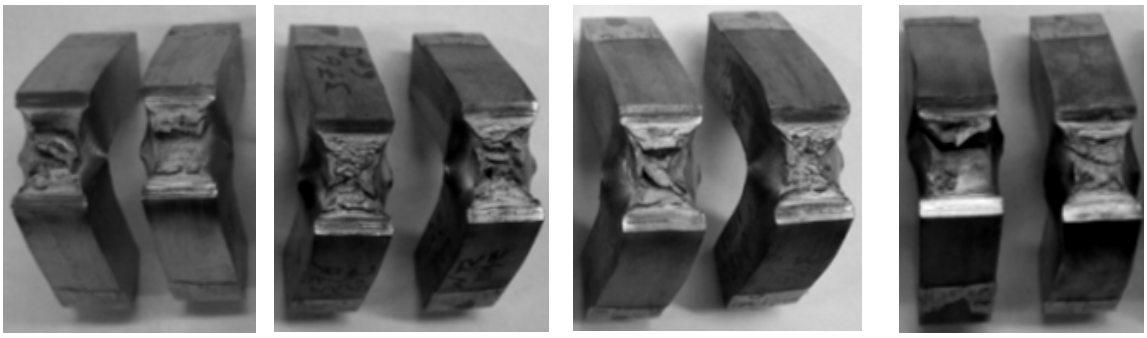

PM WT2 HAZ WT7 HAZ WT10 HAZ

Figure 4.92. Fracture morphology of Charpy impact test specimens for PM and HAZ of A709 at -30 ^{o}C.

Table 4.9. Average absorbed Charpy impact energy for A709 weldments and PM.

Weld No.	Current (A)	Speed (mm/s)	Temperature (^{o}C)		
			-60	-45	-30
			Average Absorbed Energy (J)		
WT1-HAZ	700	5.9	264 ± 77.4	287.67 ± 90.1	349.67 ± 22.7
WT2-HAZ	700	9.3	190.67 ± 69	264.67 ± 51.8	287 ± 79.9
WT5-HAZ	800	5.9	403 ± 195.6	404.5 ± 5.5	413.5 ± 2.5
WT6-HAZ	800	9.3	132 ± 80.1	289.67 ± 95.5	318 ± 9.6
WT7-HAZ	800	12.3	116 ± 77.7	134.33 ± 61.1	153 ± 28.9
WT8-HAZ	800	15.3	269.67 ± 75.3	208.67 ± 42.8	237 ± 117
WT9-HAZ	850	5.9	34.33 ± 13.7	254 ± 70.8	417.33 ± 4.8
WT10-HAZ	850	9.3	136 ± 84.7	199.3 ± 124.5	337 ± 75.2
WT11-HAZ	850	12.3	61.33 ± 15.9	283.7 ± 78.7	267.7 ± 111.8
WT12-HAZ	850	15.3	194.7 ± 109.1	241 ± 14.8	190.33 ± 38.9
PM	-	-	96.67 ± 38.58	370 ± 7.8	331 ± 62.23

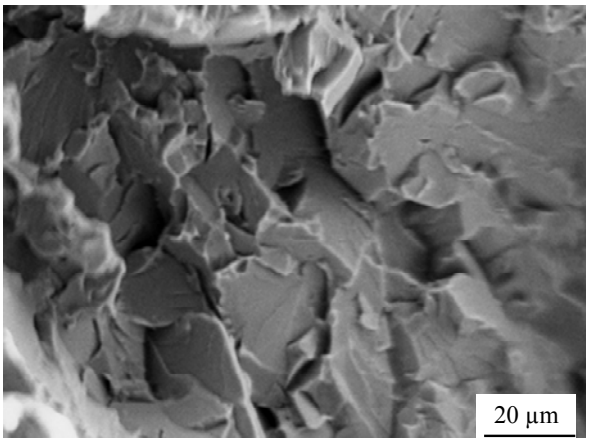

(a)

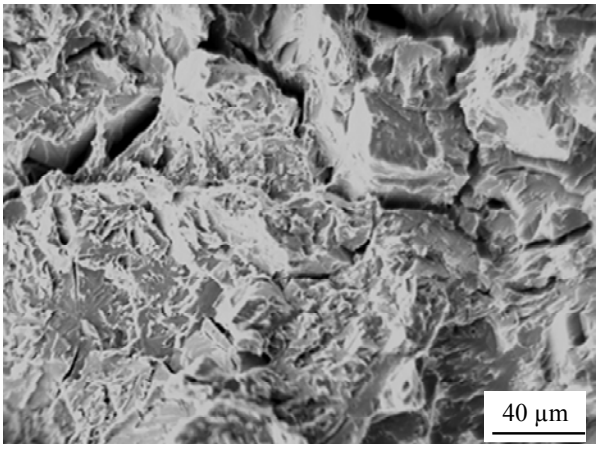

(b)

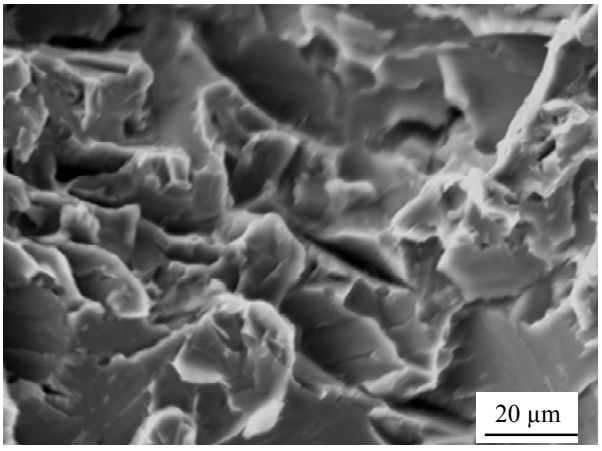

(c)

Figure 4.93. Typical SEM micrographs of Charpy impact fracture surface of the WM and PM of A709 tested at -196 ^{o}C. (a) PM, (b) WM produced using 800 A and 12.3 mm/s, and (c) WM produced using 850 A and 12.3 mm/s.

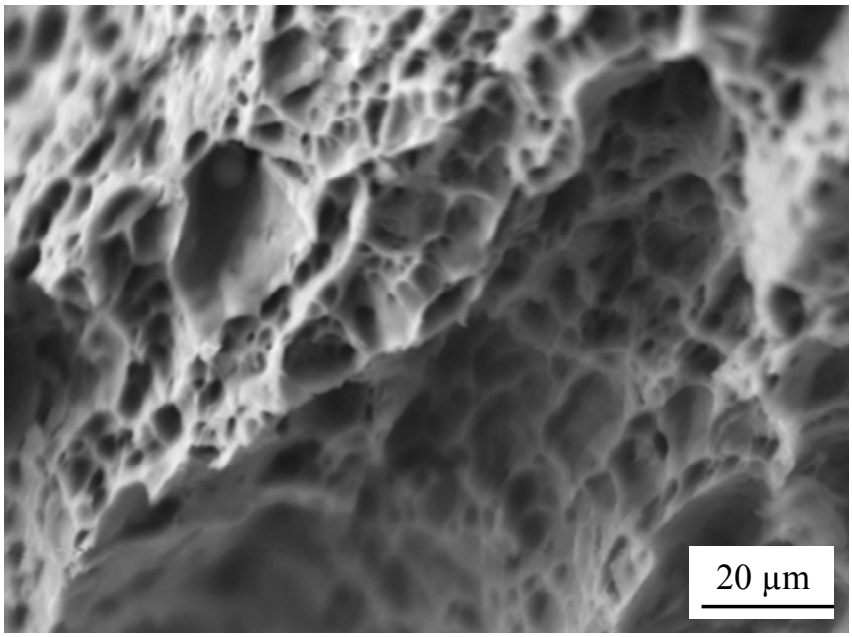

(a)

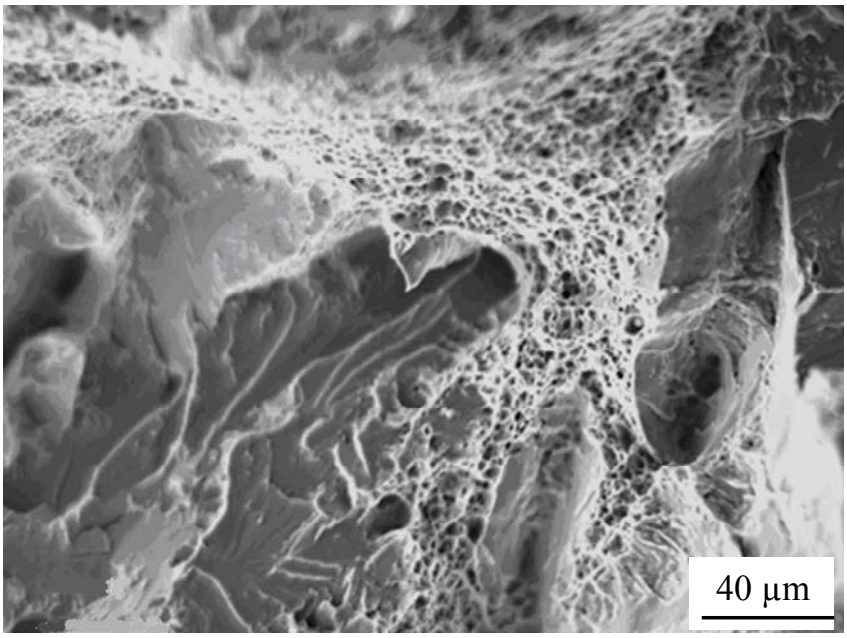

(b)

Figure 4.94 Typical SEM micrographs of Charpy impact fracture surfaces of the WM of A709 at different transition tempertures. (a) WM produced using 800 A and 12.3 mm/s (0 ^{o}C), and (b) WM produced using 850 A and 12.3 mm/s (-15 ^{o}C).

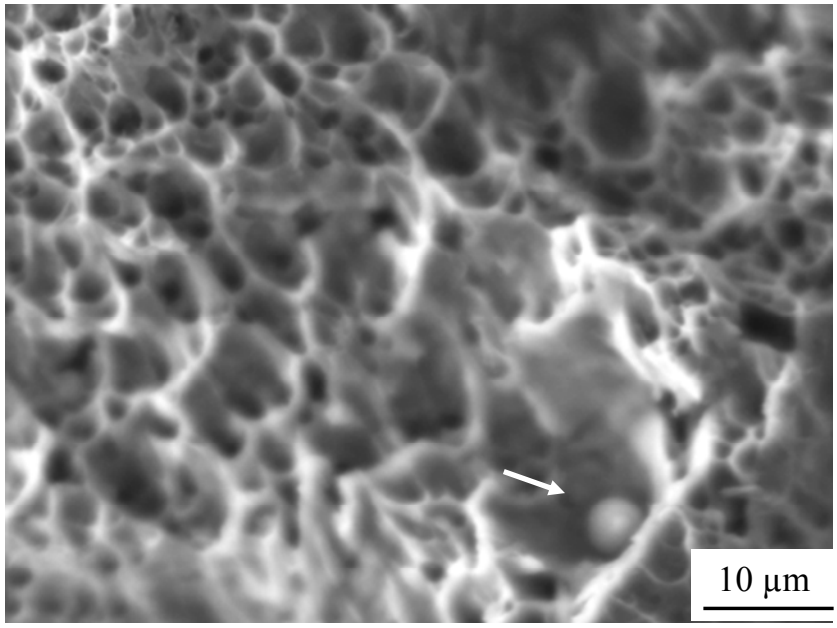

(a)

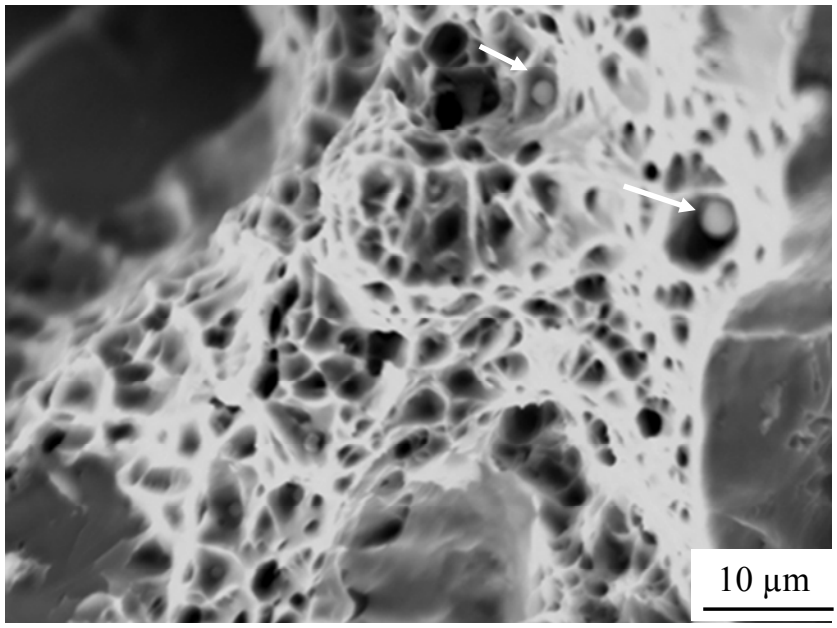

(b)

Figure 4.95. Typical SEM micrographs showing inclusions in the WM of A709. (a) WM produced using 800 A and 12.3 mm/s (100 ^{o}C) and (b) WM produced using 850 A and 12.3 mm/s (-15 ^{o}C).

5 CONCLUSIONS AND RECOMMENDATIONS

In this chapter, the conclusions obtained from the results presented in chapter 4 are summarized. Also, recommendations for future work are presented.

5.1 Conclusions

1. Welding current and travel speed significantly affected weld geometry parameters. The reinforcement, penetration depth and HAZ size of SA516 and A709 weldments increased with increasing welding current, but decreased with travel speed. The contact angle of SA516 and A709 weldments decreased with increasing welding current and travel speed. The bead width of SA516 and A709 weldments decreased with travel speed, but it had little effect on welding current.

2. The EME and WPME increased with increasing welding current and travel speed. The PME increased with increasing welding current, while travel speed had little effect on it. With a combination of SAW parameters, the WPME can be as high as 80%.

3. Severe undercuts were found in the weldments produced using 800A and 15.3 mm/s, 850 A and 12.3 mm/s, and 850 A and 15.3 mm/s. Both the undercut depth and the undercut ratio increased with increasing welding current and travel speed.

4. Lack of penetration was the major problem in weldments produced using 700 A and 12.3 mm/s, 700 A and 15.3 mm/s, and 800 A and 15.3 mm/s.

5. The CGHAZ of SA516 steel has the highest hardness, while the parent metal has the lowest hardness in all weldments. The hardness of the CGHAZ, WI and WM increased with decreasing heat input for both materials.

6. The results of Charpy impact testing showed that the WM of both steels has the lowest toughness, while the HAZ had the highest toughness for a given weldment. The toughness of the WM increased with increasing travel speed, while travel speed had little effect on the toughness of the HAZ. Toughness decreased with increasing HAZ size in the weldments. All weldments produced using 5.9 mm/s had poor toughness and cannot meet the requirements of the ASME code.

7. Of all welding parameters studied, the weldments produced using 700 A and 9.3 mm/s, 800 A and 9.3 mm/s, 850 A and 9.3 mm/s and 800 A and 12.3 mm/s met the requirements of the ASME code. The 800 A and 12.3 mm/s combination is the most feasible set of parameters due to the combination of good weld quality, productivity, melting efficiency and mechanical properties it produced.

5.2 Recommendations

1. Although ultrasonic test was used in this study to inspect internal defects, it is better to use radiographic tests to get more detailed information for different defects. Radiographic films can permanently record the locations and dimensions of the defects. A combination of both test methods can effectively find almost all internal defects.

2. Since the parent metal has the lowest strength of all the weld zones, all the tensile test specimens broke in this zone. Therefore, the yield and tensile strengths of the weld metal cannot be obtained due to its high strength. In order to investigate the effect of SAW parameters on the strength and ductility of the weld metals, the tensile specimens should be made along the welding direction.

3. Although the Charpy impact test shows that the toughness of the HAZ and PM of A709 is very high, accurate impact energy data could not be obtained because all the specimens did not shear off completely. Subsize specimens should be used in place of the standard specimen in order to obtain more accurate results.

4. The SEM fractographs show that inclusions were found in the center of the dimples. It will be informative to know the composition of these inclusions. Therefore, EDS experiment should be performed to determine the compositions of these inclusions.

REFERENCES

1 T. Gladman, The Physical Metallurgy of Microalloyed Steels, The Institute of Materials, London, Great Britain, 1997, pp. 1-11.

2 http://www.materialsengineer.com/E-steels.htm, accessed on 12th August, 2008.

3 P. A. Tichauer, "The Submerged Arc Weld in HSLA Line Pipe – A State-of-the-Art Review", Welding Research Council Bulletin, 1974, No. 201, pp. 1-18.

4 C. B. Dallam, S. Liu and D. L. Olson, "Flux Composition Dependence of Microstructure and Toughness of Submerged Arc HSLA Weldments", Welding Journal, 1985, Vol. 64, pp. 140–151.

5 I. Madariaga, and I. Gutierrez, "Role of the Particle–Matrix Interface on the Nucleation of Acicular Ferrite in a Medium Carbon Microalloyed Steel", Acta Materialia, 1999, Vol. 47, pp. 951-960.

6 S. W. Thompson, D. J. Colvin and G. Krauss, "Austenite Decomposition During Continuous Cooling of an HSLA-80 Plate Steel", Metallurgical and Materials Transactions A, 1996, Vol. 27A, pp. 1557–1571.

7 J. M. Dowling, J. M. Corbett and H. W Kerr, "Inclusion Phases and Nucleation of Acicular Ferrite in Submerged Arc Welds in High Strength Low Alloy Steels", Metallurgical and Materials Transactions A, 1986, Vol17A, pp. 1611–1623.

8 J. T. McGrath, J. A. Gianetto, R. F. Orr and M. W. Letts, "Factors Affecting the Notch Toughness Properties of High Strength HY-80 Weldments", Canadian Metallugical Quarterly, 1986, Vol. 25, No. 4, pp. 349-356.

9 E. A. Metzbower, J. J.DeLoach, S. H. Lalam, and H. K. D. H. Bhadeshia, "Analysis of Toughness of Welding Alloys for High Strength Low Alloy Shipbuilding

Steels", Science and Technology of Welding and Jointing, 1999, Vol. 6, No. 6, pp. 368-374.

10 P. K.Ghosh, P. K.Singh, and N. B. Potluri, "Fracture Properties of Multipass Submerged Arc Weld of HSLA Steel Produced by Using Flux Cored Filler Wire", Journal of Engineering and Applied Science, 1998, Vol. 38, No. 12, pp. 1379-1386.

11 R. A. Ricks, P. R. Howell and G. S. Barritte, "Nature of Acicular Ferrite in HSLA Steel Weld Metals", Journal of Materials Science, 1982, Vol. 17, No. 3, pp. 732–740.

12 S. D. Bhole, J. B. Nemade, L. Collins and C. Liu, "Effect of Nickel and Molybdenum Additions on Weld Metal Toughness in a Submerged Arc Welding HSLA Line-pipe Steel", Journal of Materials Process Technology, 2006, Vol. 173, pp. 92-100.

13 J. R. Davis, "Alloying: Understanding the Basics", Materials Park, OH, ASM International, 2001, pp. 193-209.

14 A. G. Nasibov, Yu. I. Matrosov and A. V. Rudchenko, "Effect of Vanadium, Niobium, and Silicon on the Properties of Low-Pearlite Steel", Metal Science and Heat Treatment, 1973, Vol.15, pp. 290-294.

15 http://www.leonghuat.com/articles/carbon%20equivalent.htm, accessed on 15th August, 2008.

16 T. Hong, T. Debroy, S. S. Babu and S. A. David, "Modeling of Inclusion Growth and Dissolution in the Weld Pool", Metallurgical and Materials Transactions B, 2000, Vol. 31, No. 1, pp. 161-167.

17 "Welding for Design Engineers", Canadian Welding Bureau, ON, Mississauga, 2005, p. 183.

18 http://www.twi.co.uk/j32k/protected/band_3/jk5.html, accessed on 12th August, 2008.

19 "Welding Handbook", 8th Edition, American Welding Society, Miami, FL, 1987, p. 110.

20 K. Sindo, “Welding Metallurgy", John Wily & Sons, New York, 1987, p.12.

21 http://engrwww.usask.ca/classes/ME/328/, E3 – Power Point Presentation, accessed on 12th September, 2008.

22 K. Easterling, “Introduction to the Physical Metallurgy of Welding”, Butterworths, London, 1983.

23 V. B. da Trindade Filho, A. S. Guimaraes and J. da C. Payao Filho, “Normalizing Heat Treatment Effect on Low Alloy Steel Weld Metals”, Journal of the Brazilian Society of Mechanical Sciences and Engineering, 2004, Vol. 26, No.1, pp. 62-66.

24 J. Jang and J. E. Indacochea, “Inclusion Effects on Submerged-Arc Weld Microstructure”, Journal of Materials Science, 1987, Vol.22, No.2, pp. 689-700.

25 S. S. Ghasemi Banadkouki and D. P. Dunne, “Formation of Ferritic Products during Continuous Cooling of a Cu-bearing HSLA Steel”, ISIJ International, 2006, Vol. 46, No.5, pp. 759–768.

26 H. K. D. H. Bhadeshia and L. E. Svensson, “Modelling the Evolution of Microstructure in Steel Weld Metal”, Institute of Materials, London, 1993, pp. 109–182.

27 B. Kim, S. Uhm, C. Lee, J. Lee and Y. An, “Effects of Inclusions and Microstructures on Impact Energy of High Heat-Input Submerged-Arc-Weld Metals”, Journal of Engineering Materials and Technology, 2005, Vol. 127, Issue 2, pp. 204-213.

28 R. Laitinen, “Improvement of Weld HAZ Toughness at Low Heat Input by Controlling the Distribution of M-A constituents”, 2006, Academic Dissertation to be Presented with the Assent of the Faculty of Technology, University of Oulu. Linnanmaa, pp. 22-24.

29 I. Madariaga, I. Gutierrez and H. K. D. H. Bhadeshia, “Acicular Ferrite Morphologies in a Medium-Carbon Microalloyed Steel”, Metallurgical and Materials Transactions A, 2001, Vol. 32, p. 2187.

30 Http://www.twi.co.uk/j32k/protected/band_3/jk48.html, accessed on 12th July, 2008.

31 J. Nowacki and P. Rybicki, "The Influence of Welding Heat Input on Submerged Arc Welded Duplex Steel Joints Imperfections", Journal of Materials Processing Technology, 2005, Vol. 164-165, pp. 1082-1088.

32 N. H. Croft, J. M. Gray, and A. J. DeArdo, "Submerged Arc Weld Metal Toughness in Microalloyed Linepipe Steels – the Effects of Post Weld Heat Treatment", ASM, 1984, pp. 897-913.

33 R. S. Chandel and S. R. Bala, "Effect of Welding Parameters and Groove Angle on the Soundness of Beads Deposited by SAW Process", ASM International, New York, USA, 1986, pp. 379-385.

34 Submerged Arc Welding, Miller Electric MFG. CO, Appleton, WI, USA, 1982, pp. 8-20.

35 "The Procedure Handbook of Arc Welding", 14th edition, Cleveland, OH, 2000, Section 5.2 - 5.

36 V. Gunaraj and N, Murugan, "Application of Response Surface Methodology of Predicting Weld Bead Quality in Submerged Arc Welding in Pipes", Journal of Materials Technology, 1999, Vol. 88, No. 1, pp. 266-275.

37 C. S. Lee, R. S. Chandel, and H. P. Seow, "Effect of Welding Parameters on the Size of Heat Affected Zone of Submerged Arc Welding", Materials and Manufacturing Processes, 2000, Vol. 15, No. 5, pp. 649-666.

38 L. J. Yang, R. S. Chandel and M. J. Bibby, "The Effects of Process Variables on the Bead Width of Submerged Arc Weld Deposits", Journal of Materials Processing Technology, 1992, Vol. 29, pp. 133-134.

39 J. E. Indacochca, M. Blander and S. Shah, "Submerged Arc Welding: Evidence for Electrochemical Effects on the Weld Pool", Welding Journal (Miami, Fla), 1989, Vol. 68, No. 3, pp. 77-83.

40 C. A. Butler and C. E. Jackson, "Submerged Arc Welding Characteristics of the $CaO-TiO_2-SiO_2$ System", Welding Journal (Miami, Fla), 1967, Vol. 46, No. 10, pp. 448-456.

41 C. E. Jackson, "Submerged Arc Welding, Fluxes and Relations among Process Variables", Metals handbook, ASM, Metals Park, OH, 1982, pp. 73-77.

42 J. F. Lancaster, Metallurgy of Welding, 1980, Alden Press, London, pp. 110-117.

43 G. M. Evans, "Microstructure and Properties of Ferritic Steel Welds Containing Ti and B", Welding Journal (Miami, Fla), 1996, Vol.75, No.8, pp. 251-260.

44 S. S. Tuliani, T. Boniszewski, and N. F. Eaton, "Notch Toughness of Commercial Submerged-Arc Weld Metal", Welding and Metal Fabrication, 1969, Vol. 37, No. 8, pp. 327-339.

45 R. D. Thomas Jr., "Submerged Arc Welding of HSLA Steel for Low-Temperature Services", Metal Progress, 1977, Vol. 111, No. 4, pp. 30-36.

46 H. Ornig, H. Schutz and P. Klug, "Comparison of Methods to Determine the Preheat Temperature for High-Strength Weld Metals", Welding in the World, 1998, Vol. 41, No. 2, pp. 144–148.

47 N. Bailey, "Weldability of Ferritic Steels", Abington Publishing, Cambridge, England, 1994, pp. 32-35.

48 G. M. Evans and N. Bailey, "Metallurgy of Basic Weld Metal", Abington Publishing, Cambridge, England, 1999, p. 108.

49 M. Lord, "Interpass Temperature and the Welding of Strong Steels", Welding in the World, 1998, Vol.41, pp. 452 – 459.

50 N. H. Croft, J. M. Gray and A. J. Deardo, "Submerged Arc Weld Metal Toughness in Microalloyed Linepipe Steels- the Effect of Post Weld Heat Treatment", Metals Park, OH, USA, ASM, 1984, pp. 897-913.

51 http://www.nationalboard.org/nationalboard/commissionedinspectors/topics/cinsp_topicspostweldheat.aspx, accessed on 17th August, 2008.

52 J. R. Still and J. H. Rogerson "The Effect of PWHT on the Properties of Weld Metals Containing Ti, B and Mo", Metal Construction, 1980, Vol. 12, pp. 120-123.

53 J. Bosansky, D. A. Porter, H. Astrom and K. E. Easterling, "The Effect of Stress Annealing Treatments on the Structure of High Heat Input Welds Containing Nb and Mo", Scandinavian Journal of Metallurgy, 1977, Vol. 6, No. 3, pp. 125-131.

54 D. W. Moon, R. W. Fonda and G. Spanos, "Microhardness Variations in HSLA-100 Welds Fabricated with New Ultra-low-carbon Weld Consumables", Welding Journal (Miami, Fla), 2000, Vol. 79, No. 10, pp. 278-285.

55 http://www.esabna.com/EUWeb/SA_handbook/585sa2_9.htm, accessed on 12th August, 2008.

56 R. W. Niles and C. E. Jackson, "Weld Thermal Efficiency of the GTAW Process", Welding Journal (Miami, Fla), 1975, Vol. 54, No. 1, pp. 25-32.

57 R. S. Chandel, "Electrode Melting and Plate Melting Efficiency of Submerged Arc Welding and Gas Metal Arc Welding", Material Science and Technology, 1990, Vol. 6, No. 8, pp. 772-777.

58 "Nondestructive Examination", 2004 ASME Boiler and Pressure Vessel Code, Section V, Article 9, American Society of Mechanical Engineers, NY, USA, pp. 142-144.

59 "Nondestructive Examination", 2004 ASME Boiler and Pressure Vessel Code, Section V, Article 4, American Society of Mechanical Engineers, NY, USA, pp. 46-84.

60 Annual Books of ASTM Standard, Designation E23, Vol. 03.01, 1991, pp. 197-212.

61 "Class 1 Components", 2004 ASME Boiler and Pressure Vessel Code, Section III, Division 1, Subsection NB, American Society of Mechanical Engineers, NY, USA, pp. 198-200.

62 Annual Books of ASTM Standard, Designation A370, Vol. 03.01, 1991, pp. 36-38.

63 “Rules for Construction of Pressure Vessels”, 2004 ASME Boiler and Pressure Vessel Code, Section VIII, Division 1, American Society of Mechanical Engineers, NY, USA, p. 66.

64 “Structural Welding Code - Steels”, AWS D1.1, Miami, USA, American Welding Society, 1990.

65 T. Gladman, “The Physical Metallurgy of Microalloyed Steels”, 1997, The Institute of Materials, London, Great Britain, p. 40.

66 http://www.matter.org.uk/steelmatter/metallurgy/7_1_2.html, accessed on 17th July, 2008

APPENDIX A HARDNESS DATA FOR SA516 GR.70 AND A709 GR.50

The variation of microhardness of first and second passes with distance from the weld center of SA516 weldments for various welding current-travel speed combinations are shown in Figures A1 – A3. Similar results for A709 are shown in Figures A4 – A6.

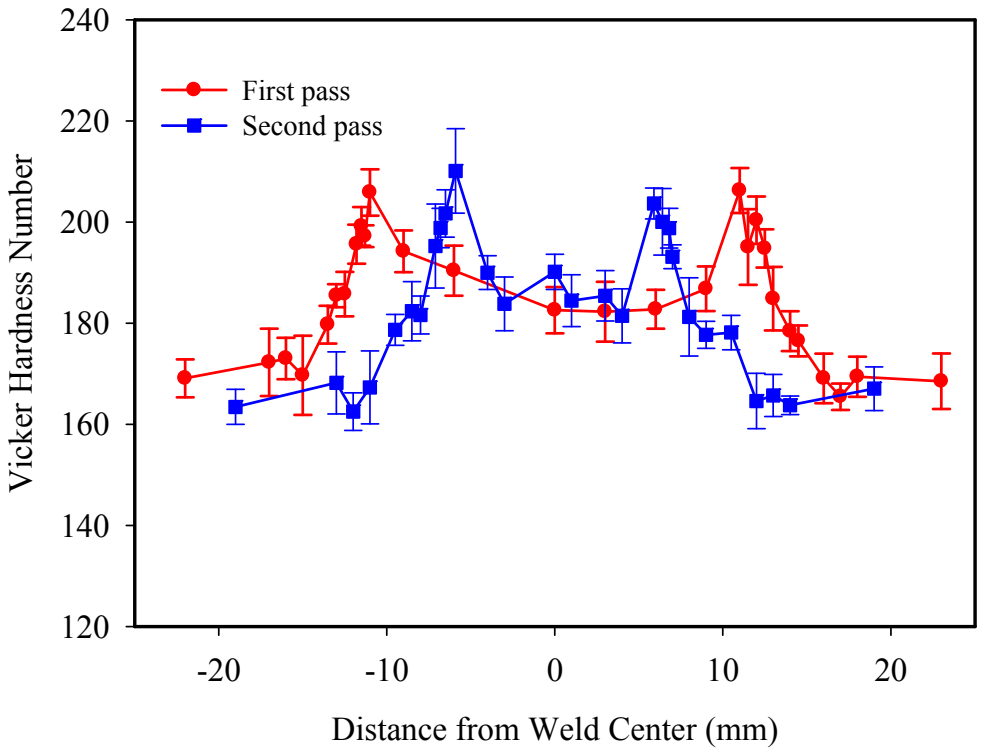

Figure A1.Variation of hardness with distance from the weld center of a SA516 steel weldment produced using 800 A and 5.9 mm/s.

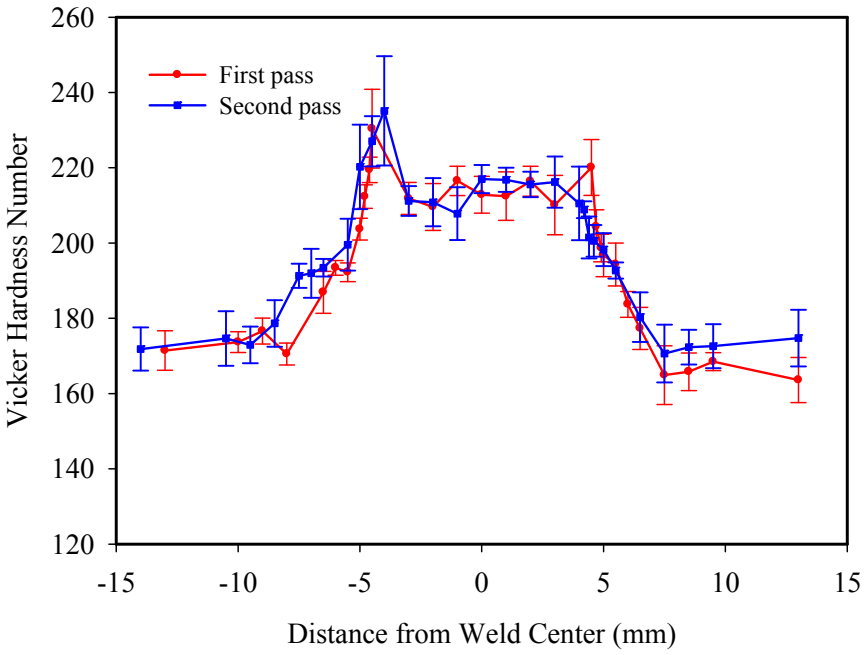

Figure A2.Variation of hardness with distance from the weld center of a SA516 steel weldment produced using 800 A and 12.3 mm/s.

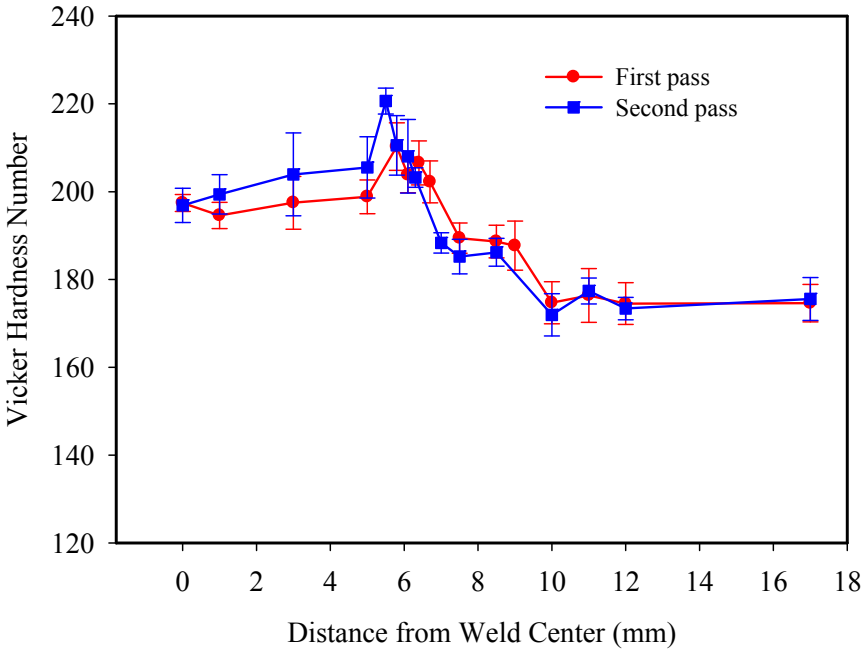

Figure A3.Variation of hardness with distance from the weld center of a SA516 steel weldment produced using 850 A and 9.3 mm/s.

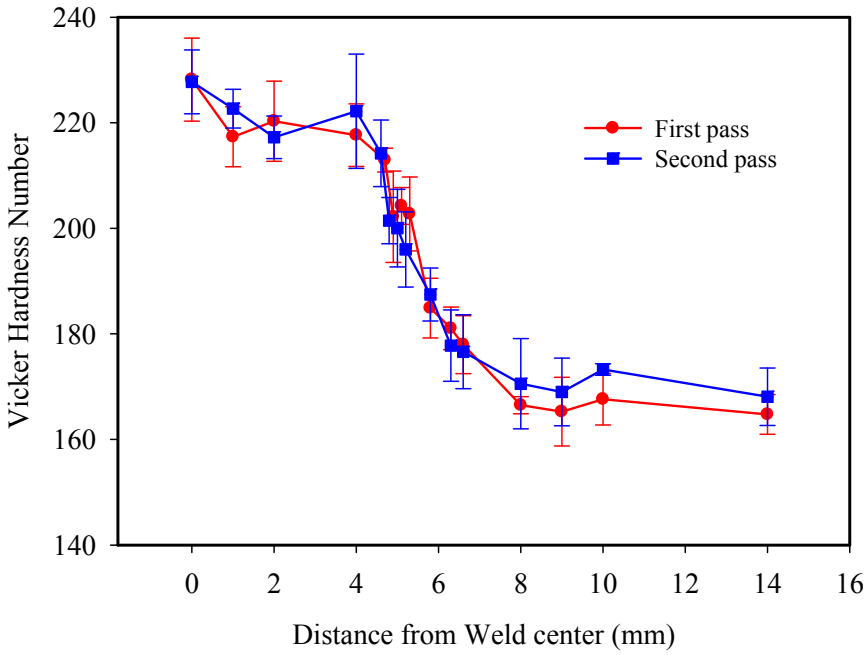

Figure A4.Variation of hardness with distance from the weld center of an A709 steel weldment produced using 700 A and 12.3 mm/s.

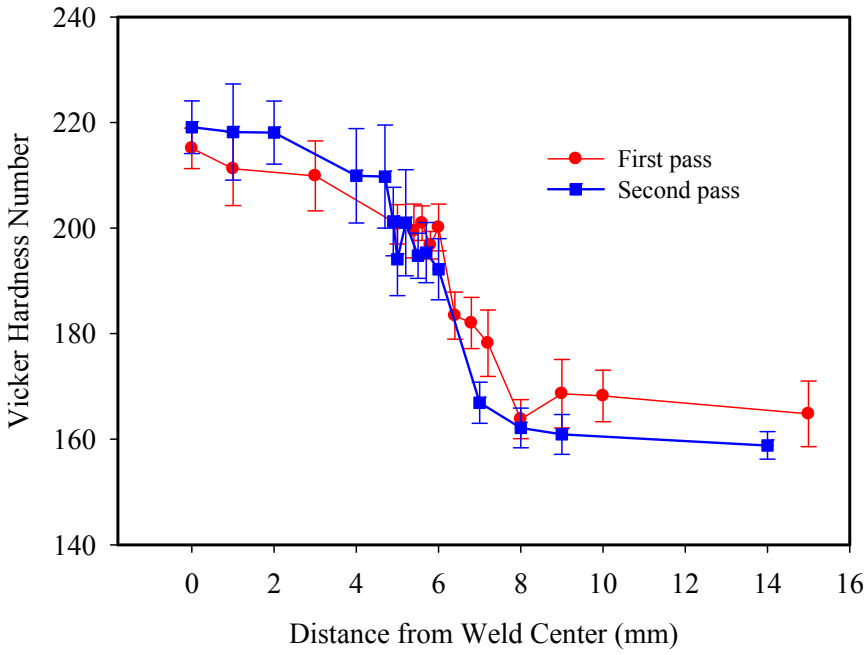

Figure A5.Variation of hardness with distance from the weld center of an A709 steel weldment produced using 800 A and 12.3 mm/s.

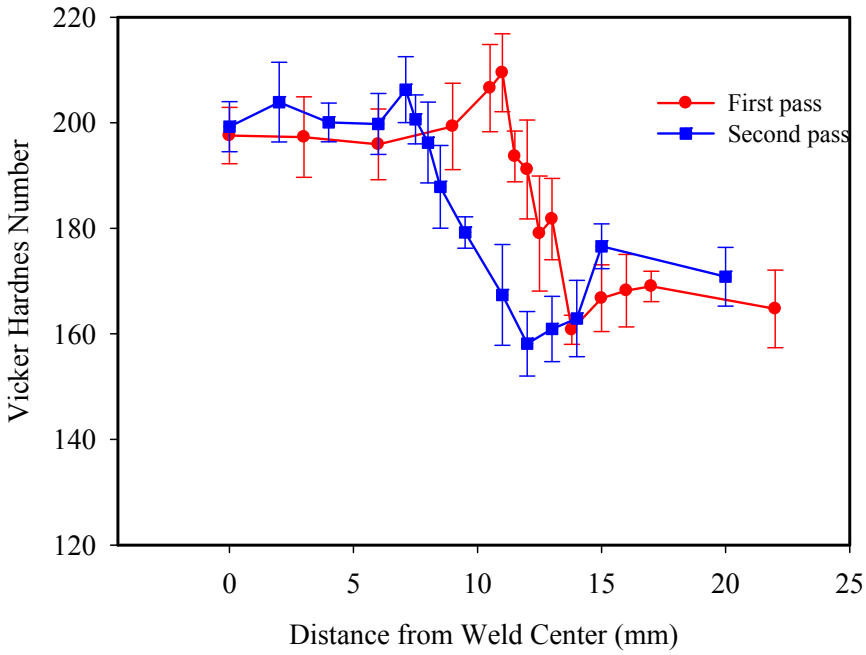

Figure A6.Variation of hardness with distance from the weld center of an A709 steel weldment produced using 850 A and 5.9 mm/s.

APPENDIX B DERIVATION OF EQUATIONS

In this appendix, Equations 2.4 and 4.1 are derived in B1 and B2, respectively.

B1. Derivation of Equation 2.4

Figure B1 shows the sketch of a weldment. Deposition rate (R_d) is defined as the weight of deposited metal per second. Thus

$$R_d = \rho V / t \tag{B.1}$$

where R_d is the deposition rate (g/s), ρ is the density of the welded metal (g/mm^3), V is volume of the deposited metal (mm^3) and t is the time.

From the sketch of a weldment, it is can be seen that $V = A_d l$. Since $l = St$, then,

$$V = A_d St \tag{B.2}$$

where A_d is the deposition area (mm^2), l is the length of a weldment (mm) and S is the travel speed (mm/s).

Therefore $R_d = \rho V / t$

$$= \rho A_d St / t$$

$$= \rho A_d S \tag{B.3}$$

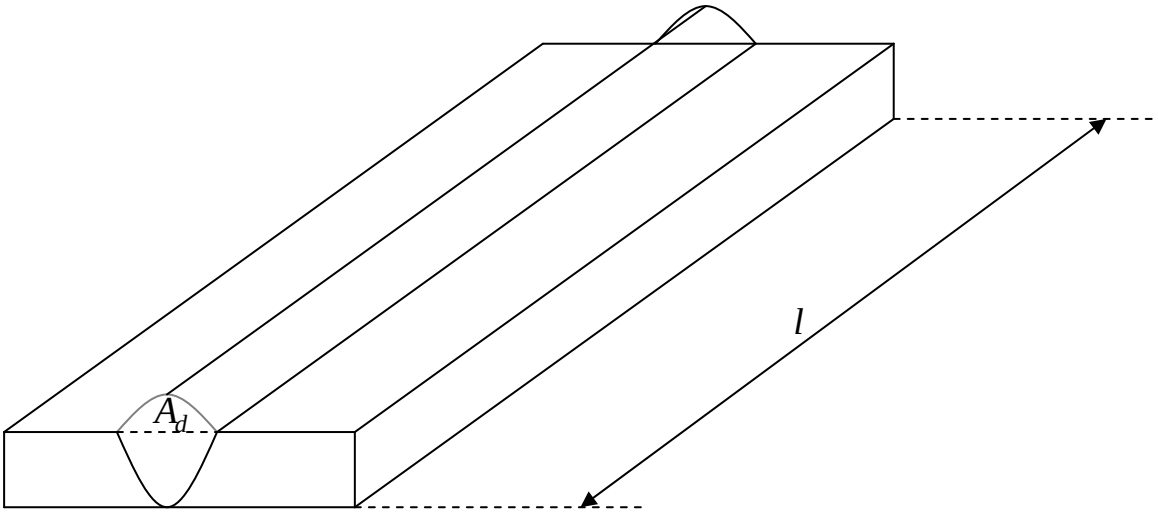

Figure B1. Sketch of a weldment.

B2. Derivation of Equation 4.1

Figure B2 shows the sketch of the cross-section of a weldment. The shape of the deposition area can be approximated to that of an isosceles triangle. So, one can use the triangle formula to calculate the reinforcement height (R) in a weldment.

So, $\tan(180-\theta) = R/(\frac{b}{2})$ and $A_d = \frac{1}{2}Rb$

Therefore: $$R = \frac{b \times \tan(180-\theta)}{2} = \frac{2A_d}{b} \quad \text{(B.4)}$$

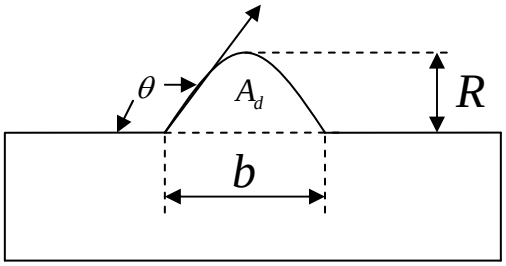

Figure B2. Sketch of the cross-section of a weldment.